ABSTRACT

Title of Thesis: THE EFFECTS OF MODEL SCALING ON SEDIMENT TRANSPORT IN BROWNOUT

Mark Samuel Glucksman-Glaser,
Master of Science, 2013

Thesis directed by: Assistant Professor Anya R. Jones
Department of Aerospace Engineering

The phenomenon of “brownout” is characterized by a large cloud of sediment or dust that is formed around a rotorcraft when it takes off or lands in arid or dusty environments. To further understand the physics of brownout, a laboratory-scale rotor hovering in water was tested over a ground plane covered with a mobile sediment bed. The sensitivity of the dual-phase flow environment to changes in the values of the similarity parameters that potentially govern the fluid dynamics of the rotor flow and the transport of sediment was explored. First, dye flow visualization was performed to study the general evolution of the rotor flow and its interaction with the ground plane. Then, dual-phase flow visualization was used to expose the details of the processes that mobilize and uplift loose particles from the sediment bed. It was shown using the flow visualization that the trailed vortices from the rotor blades were a primary contributor to the mobilization and suspension of sediment. Particle image velocimetry (PIV) was also used to obtain quantitative measurements of the flow velocities found in the rotor wake and near the ground plane. It is then discussed as to why the steady flow assumptions used in the usual definitions of the classical similarity parameters governing sediment transport are not as applicable to the dual-phase flows produced by a rotor operating over a mobile sediment bed. A Buckingham-Π analysis was performed to determine a set of new similarity parameters that potentially better reflect the dual-phase flow characteristics relevant to sediment mobilization and suspension by a rotor wake, including the characteristics of the tip vortices. Sixteen new similarity parameters were initially determined, five of which selected as having particular relevance. Specifically, these new similarity parameters were: 1. The mobile inertia ratio; 2. The stationary inertia ratio, 3. The terminal-swirl velocity ratio; 4. The threshold-swirl velocity ratio; 5. The terminal/threshold-swirl velocity ratio. The values of these similarity parameters were determined using the PIV measurements, and were all found to correlate to the quantity of sediment mobilized and uplifted by the rotor. The terminal/threshold-swirl velocity ratio is proposed as the potentially most important similarity parameter for further characterizing the brownout phenomenon.

THE EFFECTS OF MODEL SCALING ON SEDIMENT TRANSPORT IN BROWNOUT

by

Mark Samuel Glucksman-Glaser

Thesis submitted to the Faculty of the Graduate School of the
University of Maryland, College Park in partial fulfillment
of the requirements for the degree of
Master of Science
2013

Advisory Committee:
Assistant Professor Anya R. Jones, Chair/Advisor
Professor J. Gordon Leishman
Associate Professor James D. Baeder

Acknowledgments

I would like to first express my deepest thanks to Dr. Anya R. Jones, my advisor and mentor. Without her tireless guidance and encouragement this thesis would not have been possible. Dr. Jones' suggestions and comments had me researching and exploring avenues I had never thought to look, greatly improving this work. Furthermore, I would like to thank Dr. J. Gordon Leishman. His extensive knowledge on brownout and experience helped guide my writing. I would also like to thank Dr. James D. Baeder for his contributions as member of my thesis committee.

I want to specially thank everyone on "Team Leishman", past and present: Anish Sydney, Ajay Baharani, Benjamin Hance, Bharath Govindarajan, Monica Syal, Joseph Ramsey, Joseph Milluzzo, Jaime Reel, Juergen Rauleder, Nate Doane, and Natalie Jones. Your assistance with planning my experiments to get me up and running really made the difference in my research experience. Further thanks goes out to the members of the Low Reynolds Number Aerodynamics Laboratory for their help: Andrew Lind, Kristy Schlueter, David Mayo, Siddarth Kolluru, Gino Perrotta, Field Manar, Nate Beals and Peter Mancini. Thank you for giving me sound advice and supporting me throughout my research.

To my friends not mentioned previously, Aaron Thorne, Pratik Bhandari, Matt Collett, Hunter Nelson, and Elena Shrestha, thank you all for making grad school so much fun. I would also like to thank the entire faculty and staff of the Aerospace Department at the University of Maryland. It has been a privilege to complete my undergraduate and graduate research studies in this prestigious program.

My acknowledgements cannot be complete without thanking my family: Mom, Dad, grandparents, aunts, uncles, and cousins. Their love, support, and inspiration have allowed me to accomplish what I have in life and made me who I am today.

I would finally like to acknowledge the support of the Air Force Office of Scientific Research (AFOSR) under the Multidisciplinary University Research Initiative Grant No. W911NF0410176. I would like to thank the contract monitor, Dr. Douglas Smith, for his support of this research.

Contents

List of Tables

List of Figures

Nomenclature

$\dot{m}$	Mass flux through rotor disk, $\mathrm{kg\,s^{-1}}$
A	Blade disk area, $\mathrm{m^2}$
A	Particle cross-sectional area, $\mathrm{m^2}$
A_{vortex}	Vortex core area, $\mathrm{m^2}$
c	Local chord length, m
C_d	Coefficient of drag
C_t	Coefficient of thrust
D	Aerodynamic drag force, N
d	Sediment bed deflation or deposition depth, m
D_p	Sediment particle diameter, m
e	Coefficient of restitution
F^*	Densimetric Froude number
F_b	Sediment buoyancy force, N
g	Gravitational acceleration, $\mathrm{m\,s^{-2}}$
L^*	Monin-Obhukov atmospheric stability length, m
L_i	Topographical horizontal dimension, m
R	Rotor radius, m
r_c	Vortex core radius, m
Re_ν	Vortex Reynolds number
Re_{bl}	Boundary layer Reynolds number
Re_{tip}	Blade tip Reynolds number
T	Thrust force, N
t	Time, s
U_{char}	Characteristic velocity, $\mathrm{m\,s^{-1}}$
U_T, V_T	Tangential velocities along integration contour, $\mathrm{m\,s^{-1}}$
U_t	Sediment friction velocity, $\mathrm{m\,s^{-1}}$
U_t^*	Sediment threshold friction velocity $\mathrm{m\,s^{-1}}$
U_F	Sediment terminal velocity, $\mathrm{m\,s^{-1}}$
v_i	Hover induced velocity of rotor, $\mathrm{m\,s^{-1}}$
V_{tip}	Blade tip speed, $\mathrm{m\,s^{-1}}$
$\lvert V_{\text{total}}\rvert$	Total velocity, $\mathrm{m\,s^{-1}}$
$V_{\theta\text{max}}$	Maximum swirl velocity, $\mathrm{m\,s^{-1}}$
w	Rotor induced velocity, $\mathrm{m\,s^{-1}}$
y/R	Nondimensional radial location
z/R	Nondimensional axial location
z_o	Surface aerodynamic roughness height, m

Greek Symbols

Γ	Γ-Method value, $\mathrm{m\,s^{-1}}$
Γ_ν	Vortex circulation, $\mathrm{m\,s^{-1}}$
Δt	Pulse separation time, s
Δx, Δy	PIV grid spacing, m
ε	Uncertainty, %
ε_m	Uncertainty in magnification factor, %
$\varepsilon_{\Delta t}$	Uncertainty in pulse seperation time, s
$\varepsilon_{\Delta x}$	Uncertainty of particle displacement, m
η	Topographical vertical dimension, m
ν	Coefficient of kinematic viscosity $\mathrm{m^2\,s^{-1}}$
Π_i	Buckingham-Π term
ρ	Fluid density, $\mathrm{kg\,m^{-3}}$
ρ_s	Sediment density, $\mathrm{kg\,m^{-3}}$
τ	Shear stress, $\mathrm{N\,m^{-2}}$
τ_*, Θ	Nondimensional shear stress (Shields parameter)
ψ	Blade azimuth angle, deg

Abbreviations

AWI	AgustaWestland, Inc.
AZTD	Arizona test dust
CMOS	Complementary metal oxide semiconductor (camera)
DARPA	Defense Advanced Research Projects Agency
DSLR	Digital single-lens reflex (camera)
FFT	Fast Fourier Transform
GPS	Global positioning system
Nd:YAG	Neodymium-doped yttrium aluminum garnet; Nd:$Y_3Al_5O_{12}$ (laser)
NTSB	National Transportation Safety Board
PIV	Particle image velocimetry
POD	Proper orthogonal decomposition
ROI	Region of interest
TNO	Dutch Organization for Applied Scientific Research
TPP	Tip-path-plane

Chapter 1

Introduction

1.1 The Problem of Brownout

Brownout can be a consequence of rotorcraft taking-off and landing in arid, dusty environments. The effect occurs when a rotorcraft's wake interacts with and mobilizes loose dust or sand on the ground, uplifting it into a swirling, blinding dust cloud that forms rapidly, often without warning to the pilot. Figure 1.1 shows an example of a helicopter encountering brownout conditions during landing. Many helicopters are affected by brownout, and this phenomenon is a leading cause of accidents during military rotorcraft operations. As many as 60% of human-factor related accidents in military helicopter operations can be related to brownout conditions [1]. Brownout-related accidents also occur in civilian helicopter flight operations, especially those involved in MEDEVAC operations [2].

The most significant consequence of brownout is the loss of visibility to the pilot. This issue is part of a broader class of problems known as a degraded visual environment (DVE). Pilots rely heavily on visual cues during landing and take-off, so losing such a vital source of information near the ground can prove disastrous. To land a helicopter, a pilot requires visual cues ranging from the macro environment, such as the horizon or nearby structures to finer details of the surroundings, such as individual rocks. Even blades of grass give a pilot a sense of motion and orientation.

Figure 1.1: Brownout as experienced by a helicopter landing in a desert environment. (Courtesy of Optical Air Data Systems LLC.)

A dense brownout cloud can obfuscate the pilot's visual cues, and the swirling motion of the dust can give the pilot a sense of erroneous motion. The margin for error in control is very small during take-off and landing operations and minor sensory loss issues can become difficult or impossible to correct.

Brownout can also prove hazardous to ground personnel. The uplifted and suspended dust particles can irritate the eyes and throats of unprotected ground personnel, and fine dust suspended in the air creates degraded visual conditions that can hide rocks that have been thrown from the ground by the rotor wash.

The abrasive dust is also harmful to the operational health of the rotorcraft. The service life of rotor blades, engine components, windscreens, and many other flight-critical parts is greatly reduced by constant exposure to suspended dust. It has been reported that rotor blade service life can be reduced to only tens of hours if frequent or severe brownout conditions are encountered, greatly increasing the cost of maintenance and length of downtime, thus reducing the overall readiness state of a helicopter fleet [3]. Several attempts at mitigating the consequences of brownout through operations [3, 4] or sensors and display technologies [5–10] have been made, but despite these advances, brownout still remains a dangerous problem in rotorcraft operation.

1.2 Physics of Brownout

To work towards mitigating brownout at its source, a better understanding of the underlying physics of the problem must be gained. Brownout is an unsteady, three-dimensional, two-phase fluid dynamics problem caused by the interaction of the rotor flow with the ground [13]. Blade loading, overall rotorcraft performance characteristics, and the specific ground environment can all influence how severe a brownout cloud becomes [14]. Figure 1.2 shows some of the larger scale fluid dynamic mechanisms involved in brownout. Many factors are involved in the evolution of a brownout cloud, but they can be split into two main categories — those associated with the fluid, or carrier phase, and those associated with the sediment, or dispersed phase. The carrier phase consists of the downwash produced by the rotor in ground effect and the embedded blade tip vortices. The dispersed phase contains the sediment, which is mobilized and uplifted from the ground to form the dust cloud. The physics of sediment motion is described by the particle dynamics aspect of sedimentology [15].

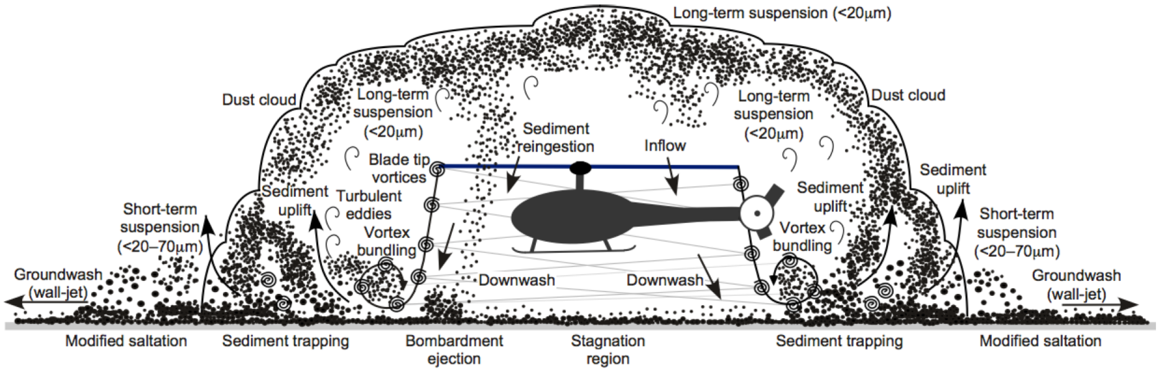

Figure 1.2: A schematic of some of the fluid dynamic mechanisms involved in sediment uplift and transport by a rotor hovering over the ground [16].

1.2.1 Fluid Mechanics

Predicting or measuring the flow of the rotor wake near the ground, even without sediment interactions at the bed, is very difficult. However, understanding the flow beneath the rotor is necessary to understand how and when sediment is uplifted. Most studies of rotors in ground effect have focused on how rotor performance is affected by near-ground operation [17–28]. Some recent studies, however, have provided insight into the detailed flow structures found in the rotor flow near the ground [16, 29–36]. These studies have shown that in ground effect, the rotor wake is characterized by persistent helicoidal tip vortices that produce large velocity excursions.

Previous studies have identified some of the differences in how a rotor wake develops out of ground effect (Fig. 1.3) and in ground effect (Fig. 1.4) [16, 29, 30]. Out of ground effect (Fig. 1.3), the rotor wake flows downwards, contracting slightly as it flows away from the rotor. Tip vortices (the cores of which are visualized as circular regions devoid of smoke) are trailed as vortex filaments from each blade tip, convecting along the slipstream boundary of the wake. Out of ground effect, the tip vortices tend to diffuse at relatively young wake ages (only about two or three rotor revolutions), beyond which the flow is mostly turbulent.

The wake initially contracts for the flow in ground effect (Fig. 1.4), as seen in the out of ground effect case. However, as the wake encounters the ground plane it spreads out and convects radially outward. In ground effect, the tip vortex filaments tend to persist to much older wake ages than out of ground effect because they stretch as they convect outwards along the ground plane, increasing their vorticity. Eventually, the vortices diffuse and form a turbulent wall jet.

Many of the flow features that have been identified in ground effect operation have been suggested as contributors to the brownout phenomenon: the tip vortices shed from the blades, the turbulent wall jet, turbulence generated by wake sheets, and unsteady suction pressures (due to the passage of the tip vortices over points on the ground). Furthermore, secondary wake structures, such as vortex pairing between adjacent turns of the helical vortices, have been noted as possible secondary contributors to sediment mobilization and transport [16] and to the severity of brownout.

1.2.2 Particle Dynamics and Sediment Transport

Sediment mobilization by a rotorcraft is caused by the interaction of the rotor wake with a sediment bed. It is important then, to understand how the shear forces, pressure gradients, and velocity gradients imposed on each particle by the

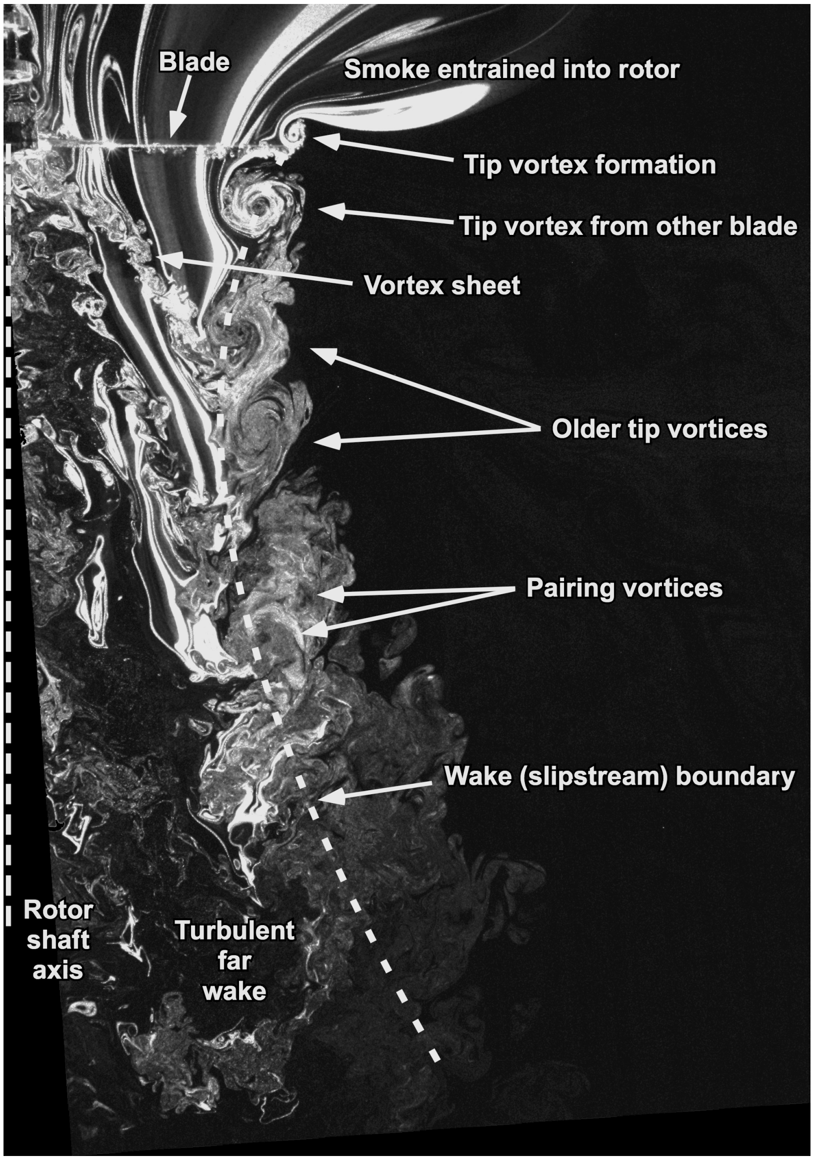

Figure 1.3: Flow visualization of a rotor out of ground effect [29].

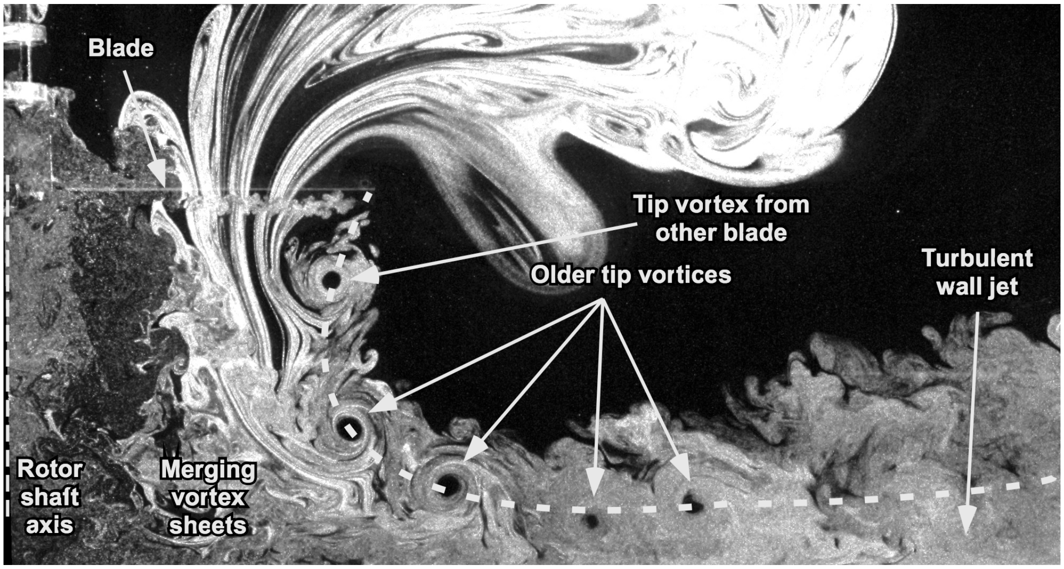

Figure 1.4: Flow visualization of a rotor in ground effect [29].

rotor wake affects its dynamics [16]. For a particle to be mobilized, the gravitational and cohesive forces on a sediment particle must be overcome by the aerodynamic forces caused by the rotor wake. Once a particle has been fully entrained into the flow, the inertial and aerodynamic properties of the sediment particle, as well as the fluid it is suspended in, become important in determining its subsequent motion.

Aeolian and fluvial sciences pertain to the study of a fluid's ability to mobilize, uplift, and suspend sediment. At their most basic level, these processes are driven by a fluid (usually air or water) flowing over a sediment bed [37], causing the mobilization of sediment particles. These particles are then carried downstream by the fluid, and are deposited at a different location. Bagnold [37], as well as Greeley and Iverson [38] studied how sediment in an aeolian environment is mobilized and entrained. Their works in this field aimed to answer, among others, two questions: By what processes does sediment move along a sediment bed? What criteria needs

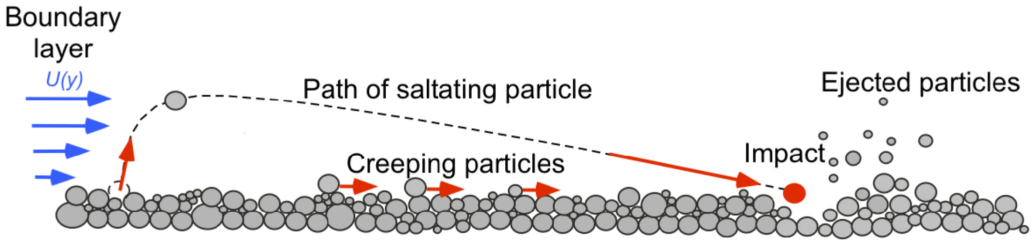

Figure 1.5: Classical aeolian creep and saltation sediment transport mechanisms [16].

to be met to initiate sediment motion and uplift?

Creep, Saltation, and Bombardment

Creep is the process by which particles roll along a sediment bed when the fluid velocity threshold for sediment mobilization has been exceeded (see Fig. 1.5). These rolling particles do not become airborne, but can disturb other particles as they move over the sediment bed, causing more particles to be set in motion and so creep. Creeping particles may also begin to hop and jump as they strike immobile and protruding sediment particles, a process called saltation. As the flow speed increases along a sediment bed, the speed at which the sediment creeps along the ground increases, and the heights to which the particles bounce increase until the particles become fully suspended.

Particles that are uplifted by the flow but do not remain suspended fall back under gravity towards the ground. These particles are said to saltate. As saltating particles collide with the sediment bed, they may dislodge other particles. This results in a cascading effect, where saltating particles cause the ejection of more and more particles, which also saltate and continue the process. A large collection of saltating particles is called a saltation layer, an example of which is the thin layer of wind-blown sand that moves just above a sand dune in high winds.

Bombardment is the process by which saltating particles collide back into a sediment bed at the end of their trajectory. This collision can loosen relatively large quantities of particles, which are then much more susceptible to mobilization and may begin to creep or saltate. Particles bombarding the surface with significant energies can also cause the ejection of particles to heights well into the saltation layer, directly increasing the quantity and concentration of saltating particles [38].

Threshold Criteria

Determining the conditions required to mobilize sediment is an important aspect of sediment transport, and many studies have done this by determining the magnitude of the threshold friction velocity, $U_t^* = \sqrt{\tau_\omega/\rho}$. This equation describes the minimum shear stress, τ_ω (given as an equivalent velocity), that is required to just overcome the gravitational and cohesive forces that resist particle motion in ideal conditions [39]. When the friction velocity on the sediment bed, U_*, (caused by the boundary layer of the passing fluid) is greater than the threshold friction velocity, sediment particles on the bed will begin to become mobilized.

Particles that are exposed to this shear stress but wedged against other particles may still not begin to move (see the discussion of incipient sediment mobilization in Appendix A). Near the threshold friction velocity, mobilized particles will generally only undergo creep. Greater increases in velocity along the ground are required to uplift the particles and so generate a saltation layer [38].

Shields Parameter

Shields parameter (τ_* or θ as given by Eq. 1.1) is another method used in the aeolian sciences to establish when sediment might begin to move.

$$\tau_* = \theta = \frac{\tau}{(\rho_s - \rho) g D_p} \tag{1.1}$$

This parameter describes the relationship between the fluid forces and gravitational forces on a sediment particle, and can be viewed as another form of the non-dimensional shear stress on the sediment bed. Finding the values of Shields parameter is difficult [40] and there is subjective error in identifying at what velocity initial mobilization occurs [41, 42]. The present work, therefore, uses the threshold friction velocity rather than the Shields parameter to determine particle threshold velocities.

1.3 Prior Work

A variety of research has been performed to study how the physics of brownout relate to rotorcraft. Computational approaches, such as the computational fluid dynamics (CFD) work performed by Kalra [31] and Thomas [43], attempt to model the brownout problem numerically. Several other CFD studies searched for ways to reduce the problem [44–46]. CFD can be useful as it allows for the investigation of many different aspects of brownout physics that can be hard to model in the laboratory, but experiments also necessary. Physical testing in addition to CFD expands knowledge of the brownout phenomenon by examining how actual brownout clouds behave, and the data acquired helps to validate numerical models and simulations.

1.3.1 Full-Scale Research

There is little data on the brownout cloud produced by a full-scale rotorcraft. One full-scale study, performed by Wong and Tanner [36], used photogrammetry as a means for quantifying the size and shape of a brownout cloud. This work provided observations of how a brownout cloud forms and evolves, but measurements of internal velocities, shear stresses, or other fluid properties in the brownout cloud were not attempted. Another study performed by the U.S. Air Force [5,6] measured the quantity of sediment uplifted by several different helicopters in an attempt to quantify brownout intensity. This information was used to identify general trends of sediment uplift across different helicopter platforms.

Using this and other data on helicopter brownout, Milluzzo and Leishman [47] attempted to understand why some rotorcraft experience more severe brownout conditions than others. It was theorized that certain factors, such as average downwash velocities, blade tip vortex strengths, and vortex frequency in the rotor wake, are related to the severity of the brownout clouds produced.

In most cases, performing full-scale experimentation is a difficult and expensive proposition. In addition to the manpower and material cost of operating a helicopter, the inherent risks of operating a rotorcraft in brownout conditions must be taken into account. Measuring flow velocities in a brownout cloud is also very difficult. The DVE conditions caused by a brownout cloud makes it extremely difficult to use optical flow measurement techniques. It is also nearly impossible to account for naturally occurring events such as wind or rain, which can affect how a dust cloud develops and evolves.

1.3.2 Laboratory-Scale Research

The difficulty in obtaining accurate and comprehensive flow field measurements of the brownout phenomenon at the full-scale drives the need for laboratory experiments. For example, a camera with extremely high resolution would be needed to resolve individual sediment particles in a full-scale brownout cloud. By reducing the problem to a laboratory-scale, the composition and motion of the dust cloud can be measured.

To date, laboratory-scale research has focused on identifying the fundamental aerodynamic and sediment transport processes that contribute to the brownout phenomenon [16, 29, 30]. Nathan and Green [33] studied the flows produced by a small-scale rotor in ground effect at low advance ratios. They used particle image velocimetry (PIV) to measure velocity profiles of the rotor wake in ground effect. Research performed by Sydney et al. [16] identified the underlying physics that govern how brownout clouds may develop. In addition to creep, saltation and bombardment, Sydney identified several additional mechanisms of sediment transport in rotor flows. Vortex-induced trapping, secondary suspension of particles, and unsteady pressure effects were identified as further mechanisms by which brownout clouds may develop.

1.4 Scaling Issues of Brownout

With most studies of the brownout phenomenon being performed in the laboratory-scale, there is a need to understand how these results correlate to the brownout dust clouds produced by full-scale helicopters. To relate a laboratory-scale brownout environment to full-scale, the physics of both the aerodynamics and sediment transport must be scaled simultaneously. Prior work has not fully accounted for the effects of scaling. However, without understanding how changing scale affects the sediment entrainment characteristics produced by a rotor, the results from these experiments are difficult to apply to the full-scale brownout problem.

To relate results from laboratory-scale testing to full-scale environments, each flow is characterized by similarity parameters. According to Greeley and Iverson [38], there are at least fifteen similarity parameters that must be matched to achieve dynamic similarity in aeolian flows (Table 1.1). The complexities of matching just a few of the scaling parameters between full-scale and laboratory-scale rotor flows means that no previous research has achieved true dynamic similarity of the two-phase flow.

The sensitivity of sediment transport under a rotor to five of Greeley and Iverson's [38] fifteen scaling parameters (parameters 2, 3, 5, 12, and 14 in Table 1.1), was studied by Baharani [29]. Table 1.2 lists the calculated laboratory-scale values from that study. The selected parameters included, in order of importance to sediment uplift, the particle-to-fluid density ratio, ρ_s/ρ; the threshold friction speed ratio, U_{char}/U_t^*; the particle diameter-to-rotor radius ratio, D_p/R; the densimetric

Table 1.1: Classical nondimensional scaling parameters used in aeolian transport [38].

Parameter	Expression	Description
(1)	d/R	Deposition depth ratio
(2)	D_p/R	Particle diameter-to-rotor radius ratio
(3)	U_{char}^2/gR	Froude number
(4)*	e	Coefficient of restitution
(5)	U_{char}/U_F	Ratio of characteristic velocity to particle terminal speed
(6, 7, and 8)	$L_i/R, (z/R)/R, \eta/R$	Topographical geometric similarity
(9)	z_0/R	Roughness similarity
(10)	L^*/R	Boundary layer stability similarity
(11)	$U_{\text{char}}R/\nu$	Reynolds number
(12 and 13)	$U_{\text{char}}/U_t, U_{\text{char}}/U_t^*$	Friction speed ratios
(14)	ρ_s/ρ	Density ratio
(15)	$U_{\text{char}}t/R$	Time scale

* – Coefficient of restitution is not a similarity parameter, but a nondimensional parameter governing particle elasticity and energy transfer between colliding particles.

Froude number, $U_{char}/\sqrt{((\rho_s/\rho)-1)gD_p}$; and the ratio of characteristic flow speed to particle terminal speed, U_{char}/U_F. A discussion of each of these parameters is given in Appendix A.

Table 1.2 shows that for full-scale vehicle operation, tip chord Reynolds numbers are of the order 10^7, but at the laboratory-scale, Reynolds numbers are typically of the order 10^4. The terminal velocity ratio is also several orders of magnitude different, largely because of differences in the characteristic velocity, U_{char}. The downwash velocities produced by a full-scale rotorcraft are much higher than those produced by a laboratory-scale rotor. The higher characteristic velocities found at full-scale (a direct result of the higher downwash velocities) result in terminal velocity ratios that are two orders of magnitude higher than at laboratory-scale.

Greely and Iverson's similarity parameters are widely accepted in the aeolian sciences, but these classical similarity parameters were developed using steady flow assumptions that may not hold for a rotor flow. Rotor flows are highly unsteady and include significant turbulence, vorticity, and a host of other characteristics that can affect sediment mobilization. It is, therefore, unclear how well the classical parameters describe the scaling of the problem of brownout.

One of the biggest differences between a large-scale fluvial/aeolian flow and a rotor flow is the periodic passage of a tip vortex over the sediment bed. The passage of a tip vortex element produces vertical velocity components that can mobilize and uplift sediment particles, and so cause them to be transported much further and in different directions than would occur in uniform flow. In addition, vortex passage causes large transients in the horizontal velocity over the ground plane, which affects

Table 1.2: Selected scaling parameters.

Scaling Parameters		Full-Scale	Lab-Scale in air, Ref. [29]	Lab-Scale in water (estimated)
Reynolds number	$\frac{U_{\text{char}}R}{\nu}$	1×10^7	3×10^4	3×10^4
Time scale	$\frac{U_{\text{char}}t}{R}$	1×10^{-3}	5	0.2
Particle-to-fluid density ratio	$\frac{\rho_s}{\rho}$	2.25×10^3	2.19×10^3	2.5
Densimetric Froude number	$\frac{U_{\text{char}}}{\sqrt{(\frac{\rho}{\rho_s}-1)gD_p}}$	49	4	3
Particle size-to-rotor radius ratio	$\frac{D_p}{R}$	6.22×10^{-7}	6.42×10^{-4}	6.42×10^{-4}
Terminal velocity ratio	$\frac{U_{\text{char}}}{U_F}$	5.31×10^3	20	9
Threshold friction speed ratio	$\frac{U_{\text{char}}}{U_t^*}$	28	40.7	24

the instantaneous values of many of the similarity parameters, e.g., the threshold friction velocity [49]. While the average velocity along the sediment bed may be below the threshold velocity, the velocity fluctuations in an unsteady flow may exceed the threshold value, mobilizing the particles [50]. A proper characterization of the unsteady flow velocites near the sediment bed is, therefore, important in understanding the brownout environment.

Several of the similarity parameters given in Tables 1.1 and 1.2 are functions of U_{char}, the characteristic velocity of the flow. In the field of aeolian sciences, characteristic velocity is calculated from the averaged wind speed of the flow. In classical sediment transport problems, the flow is steady, and an average wind speed is representative of flow conditions. This is not the case in rotor flows. Inspired by the methods of the aeolian sciences, previous two-phase rotor flow testing has calculated the characteristic velocity using the time-averaged downwash velocity of the rotor [16, 29]. Baharani [29], for example, calculated the characteristic velocity from the average velocity of the flow field in the region where sediment was noted to become mobilized. However, this averaged velocity is not fully representative of the unsteady and three-dimensional nature of a flow under a rotor at any instant in time. The choice of a characteristic velocity is important as it affects the values of many of the similarity parameters.

1.5 Objectives of the Present Research

The main objectives of this research are:

1. To determine which of the classical scaling parameters best characterize the aerodynamics and sediment transport below a rotor, to improve the understanding of how full-scale brownout problem might be better reproduced in the laboratory.

2. To compare results over a range of scaling parameters (especially Reynolds number and density ratio) different to that of previous experiments.

3. To identify new scaling parameters that could be used to better predict the onset and severity of brownout.

In the current research, a rotor operating in ground effect over a flat plate was tested in water. Because water has a viscosity and density much higher than air, a different range of scaling parameters was possible. These scaling parameters, when also combined with results from previous work [29], provide for a wider range of similarity parameter values. Dye flow visualization, particle image velocimetry, and dual-phase flow visualization were used to explore the effects of the similarity parameters on the mobilization and uplift of sediment particles. Furthermore, this work explored different methods of calculating the selected scaling parameters to account for flow unsteadiness. A dimensional analysis accounting for the characteristics of both the sediment particles and the most dominant structures in a rotor flow, i.e., blade tip vortex filaments, helped identify new parameters for future study.

Chapter 2

Description of the Experiments

2.1 Overview

The present research involves experiments performed in single-phase and dual-phase flow environments below a hovering rotor operating in ground effect. The goal of these experiments was to determine the effects of changing some relevant scaling parameters by performing experiments in water rather than air. The increased density and viscosity of water allows for the ranges of the scaling parameters to be increased or decreased relative to what would be obtained in air. This chapter describes the experiment, the setup, instrumentation, and the techniques used to collect and analyze the data. The difficulties encountered with the experiments and challenges with measurements are also discussed.

2.1.1 Water Tank

All experiments were conducted in a $1.2 \times 1.2 \times 1.2\,\mathrm{m}$ water tank, shown in Fig. 2.1, located at the Low Reynolds Number Aerodynamics Laboratory (LRAL) at the University of Maryland, College Park. The water tank was constructed with 3.81 cm (1.5 in) thick acrylic walls. The tank was placed into a steel support framework and supported 1 m the ground to allow optical access on all sides. Testing equipment (such as cameras and the laser system) was positioned orthogonally to

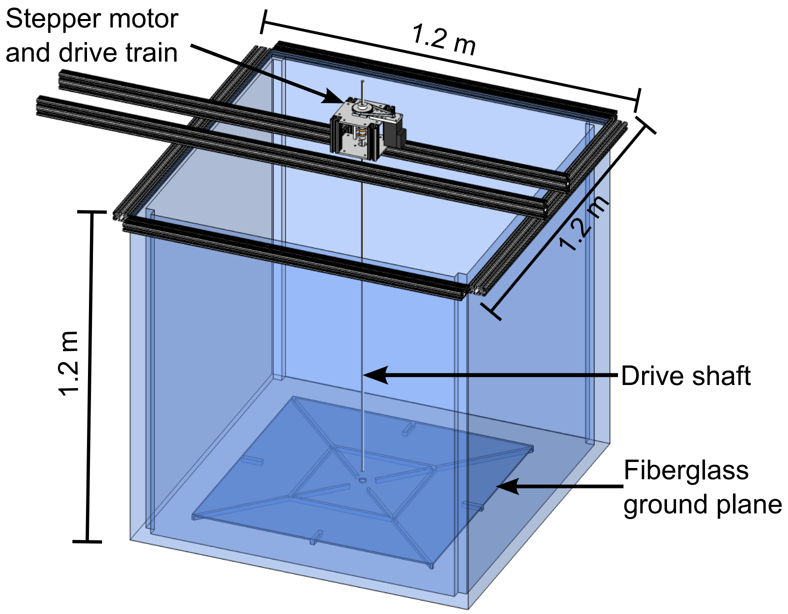

Figure 2.1: Water tank setup with motor and drive-train.

the walls of the tank to prevent image distortion caused by the differing indices of refraction in air, acrylic, and water.

2.1.2 Rotor System

Two different rotors were used in these experiments. For initial dye flow visualization and proof of concept work, a two-bladed rotor with a radius of 85 mm (3.34 in) was used to create the rotor wake. The design of the rotor was based on previous research [29]. The rotor had untwisted rectangular blades (constant chord) using cambered flat plate airfoils with rounded leading edges. These airfoils were selected because a cambered flat plate has increased aerodynamic efficiency relative to traditional airfoils at low Reynolds numbers [28]. Figure 2.2(a) shows a sketch of the rotor. (A technical drawing of the rotor is given in Appendix B.) The rotor had

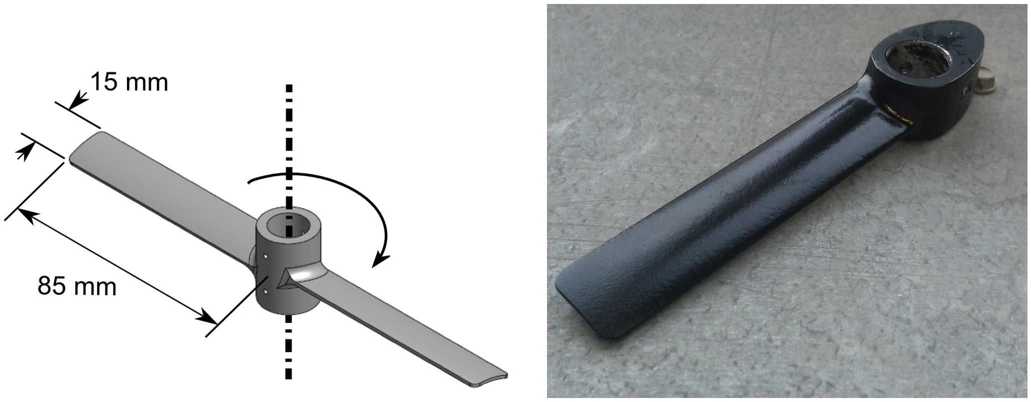

(a) Sketch of the two-bladed rotor.

(b) Single-bladed rotor.

Figure 2.2: Rotors used for experimentation.

fixed pitch and was set at 12° collective relative to the chord line. It was fabricated using three-dimensional rapid prototyping using Nylon-12 doped with carbon fiber composite. The forces generated by operating in water were so high that the rotor deformed unacceptably at higher rotational speeds, limiting the use of this rotor to low-speed flow visualization.

The dual-phase flow visualization and particle image velocimetry experiments utilized a one-bladed rotor (Fig. 2.2(b)) to generate the rotor wake. This one-bladed rotor was milled from a solid billet of aluminum. The overall blade design of this rotor was the same as for the two-bladed rotor, however one blade was replaced by a tungsten carbide counterweight. Solid aluminum construction allowed much higher rotational rates to be achieved, without any of the flexing or coning seen with the Nylon rotor. The one-bladed rotor incorporated two set screws used to position the rotor at the desired height above the ground plane. All of the present experiments were performed with the rotor a height of one rotor radius (85 mm) above the ground

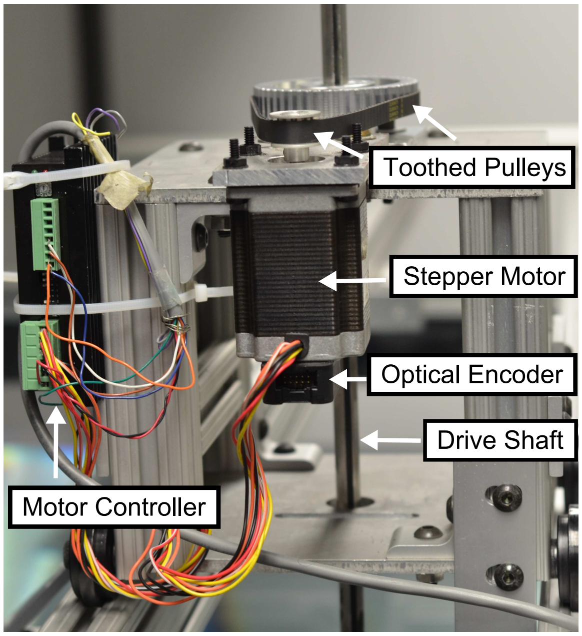

Figure 2.3: Photograph of drive assembly.

plane or sediment bed.

The rotor was fitted to a 12.7 mm (0.5 in) drive shaft that was 1.5 m long. One end of the drive shaft was passed through a hole in the ground plane and was located in a bearing secured to the bottom of the tank. This bearing provided support for the drive shaft. The other end of the drive shaft passed through a set of tapered bearings above the waterline and entered the drive assembly. In the drive assembly (Fig. 2.3), the rotor shaft was driven by a stepper motor through a set of toothed pulleys with a gear ratio of 1:2. An optical encoder provided tracking of the rotational position of the rotor blades.

The stepper motor was programmed to gradually increase the speed of the rotor to the required operational condition, and then slow it down after data collection was completed. An optical encoder was used to synchronize the rotor position

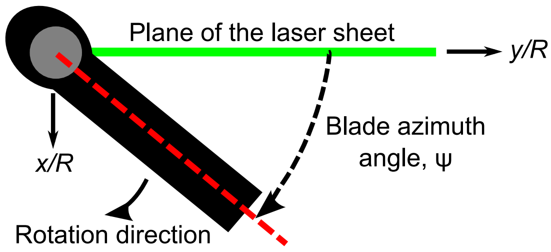

Figure 2.4: Diagram of blade azimuth angle, ψ; top down view of rotor.

with the camera and laser equipment. The blade azimuth angle, ψ, is defined to be $\psi = 0°$ when the mid-chord of the rotor blade passes through the plane of the laser light sheet (see Section 2.6.1). The angle of the axis of the rotor blade relative to the plane of the laser sheet viewed from above defines the blade azimuthal angle, as shown in Fig. 2.4.

2.1.3 Ground Plane

A fiberglass ground plane, shown in Fig. 2.1, was placed above the bottom of the tank to clear the bearing affixed to the tank bottom. It extended to the edges of the tank, with a hole in the center to accommodate the drive shaft that supported the rotor. The ground plane also provided protection to the acrylic of the tank when sediment particles were used; without a separate ground plane, the sediment particles would abrade the acrylic. For experiments utilizing lasers, the ground plane was painted a matte-black to reduce laser reflections.

For all measurements, the origin of the coordinate system was positioned at the intersection of the axis of rotation and the ground plane, as shown in Fig. 2.5. Moving away from the ground plane towards the top of the tank was defined as

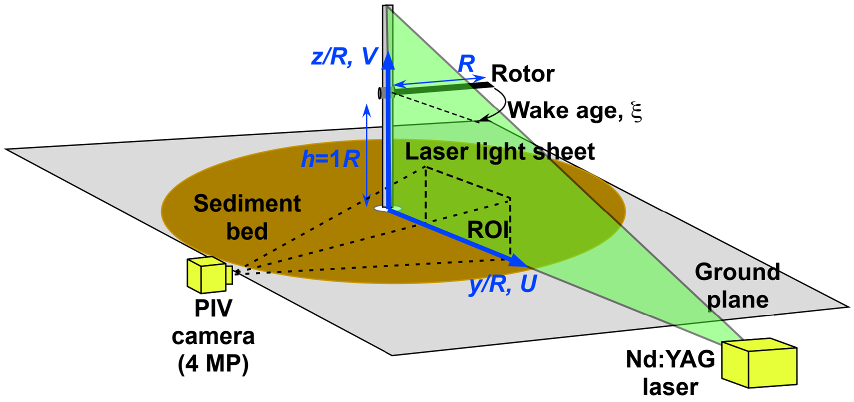

Figure 2.5: Experimental setup.

positive z/R, the nondimensional vertical height. Moving out away from the axis of rotation was defined as positive y/R, the nondimensional radial location. In order to capture images for this work, a camera was arranged as shown in Fig. 2.5, with the optical axis of the camera orthogonal to the axis of the laser sheet

2.2 Seeding and Sediment Particles

Soda-glass microspheres of diameter 45–63 μm (average diameter of 54 μm) were placed on the ground plane to form a bed of sediment about one centimeter thick. The soda-glass particles were chosen because they were of the same type used in previous experiments in air [16, 29]. Because the glass spheres were denser than the water (specific gravity = 2.478), they remained stationary on the ground plane until mobilized by the rotor flow. By using the same glass particles as in previous research in air, the effect of changing just the operating fluid was evaluated.

Denser stainless steel particles were also used for this experiment to determine how changing the properties of the sediment particles affected their mobilization and transport. The steel particles were between 44–125 μm in diameter, with an average size of 90 μm. They had a specific gravity of 7.495, approximately three times higher than the soda-glass microspheres.

The particle image velocimetry (PIV) and dual-phase flow visualization required the use of tracer particles suspended within the water to track the fluid motion. A Nylon powder (Vestosint 2070) was selected because of its near-neutral buoyancy in water, as well as its small and consistent size ($\sim$2 μm in diameter). This powder, once mixed into the water, remained in suspension for several days.

2.3 Regions of Interest

Two primary regions of interest (ROI) were studied in these experiments. They are shown in Fig. 2.6, laid over a schematic of the rotor setup and ground plane, along with some key flow features found during experimentation. ROI 1 consisted of a region from $y/R = 0.75$ to $y/R = 2.6$. This large field of view allowed for quantitative measurements to be taken across a large portion of the flow field, and provided an overall understanding of the features present in the flow. This view also provides insight into which areas in the flow require further study, i.e., areas that might contain interesting flow features, or where sediment would likely be mobilized and entrained.

ROI 2, consisting of the region from $y/R = 1.50 - 2.5$, covers a smaller area that contains the highest velocities across the ground plane. Therefore, this region was most likely to contain mobilized sediment. Phase-resolved PIV was performed

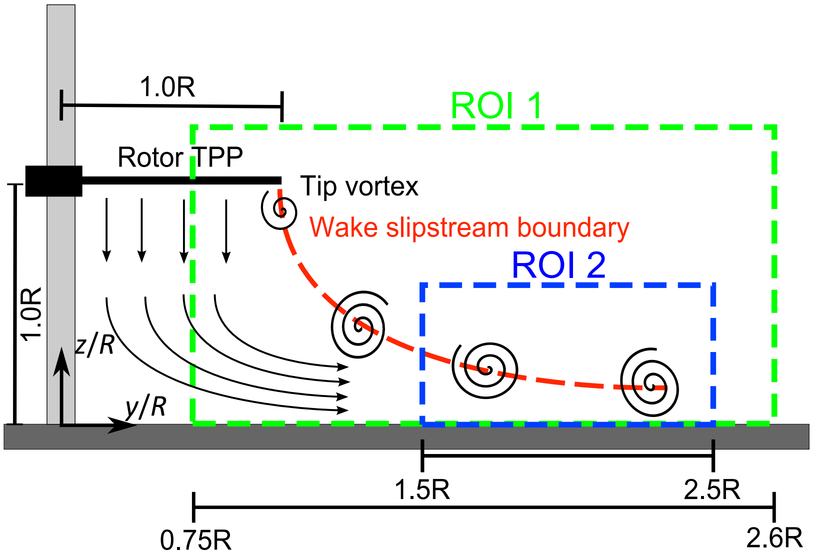

Figure 2.6: Schematic of regions of interest.

in this region of interest, as was dual-phase flow visualization.

2.4 Operating Conditions

The experiments in this research were performed in water. The main purpose of using water as the working fluid was to allow for larger changes in the values of the similarity parameters as compared to previous tests done in air. The tip Reynolds number, Re_{tip}, is defined as

$$Re_{\text{tip}} = \frac{V_{\text{tip}} c}{\nu} \tag{2.1}$$

where V_{tip} is the tip speed of the rotor, c is the blade chord, and ν is the kinematic viscosity of the fluid, in this case water. Water, with its lower kinematic viscosity (1.004×10^{-6} m^{2}s^{-1}) compared to air (1.568×10^{-5} m^{2}s^{-1}), requires lower tip speeds to achieve the same tip Reynolds numbers as for tests done in air.

To quantify the relative importance of the different scaling parameters, several rotor operating conditions were used. Because the rotor used for this work was set to a fixed pitch of 12°, increasing rotor rpm increased the thrust produced by the rotor. This increase in thrust also increased the rotor disk loading, induced velocity, and slipstream velocity of the rotor wash. Five operating conditions, each at a different blade rotational frequency, were used. For this work, measurements of sediment uplift are compared at different rotor operating conditions, represented by tip Reynolds number, Re_{tip}, and rotor speed, rpm. It is important to note that while tip Reynolds number is used to characterize the rotor operating condition, the effects seen are not necessarily caused by increased Reynolds number, per se, but by the increase in thrust (i.e., causing an increase in downwash velocity). Thrust was not measured in this research because of the difficulty in incorporating a force balance into the experimental setup.

Table 2.1 gives the different rotor operating conditions used for the present research. To prevent recirculation in the tank from becoming a significant contributor to the measured flow, the running time of the rotor was limited to two minutes or less. After running the rotor, the water was allowed to settle for a period of not less than 30 minutes (a time chosen based on observation of tank settling). During the dual-phase testing (as explained in following sections), this settling time was also used to re-level the sediment bed to ensure a smooth surface.

Table 2.1: Rotor operating conditions.

Rotor Speed (rpm)	Blade Passing Frequency (Hz)	Tip Speed (ms^{-1})	Tip Reynolds Number (Re_{tip})
80	1.333	0.712	1.06×10^4
100	1.667	0.890	1.33×10^4
120	2.000	1.068	1.60×10^4
152	2.533	1.353	2.02×10^4
450	7.500	4.006	5.98×10^4

2.5 Flow Visualization

The flows induced by the single-blade and dual-blade rotors were first qualitatively studied using flow visualization and high-speed photography. As shown in the region of interest schematic (Fig. 2.6), the flow consists of a mean outflow and vortices trailed from the blade tips. Several methods of flow visualization were used in this research. Flow visualization utilizing concentrated dye helped to show the regions that were needed further study, as well as revealing some of the overall complexities in the flow beneath a rotor operating near the ground. Single-phase flow visualization in a seeded flow provided experience in seeding methods, and allowed for photographic techniques to be developed. Dual-phase flow visualization helped show the degree of sediment uplift, as well as the effect of scaling parameters and the effect of rotor operating conditions on sediment mobilization.

2.5.1 Dye Flow Visualization

While visualizing the movement of the sediment under the action of the rotor was an important part of studying the particle uplift mechanisms found beneath the rotor, studying the movement of the water itself was also required. For dye flow visualization, concentrated dye was used to identify the flow structures. A long needle was fed through the ground plane and the dye was injected immediately under the tip-path-plane (TPP) of the rotor (see Fig. 2.6) to identify the vortices present in the rotor wake. The downwash of the rotor carried the dye with the rotor flow, making elements of the tip vortex filaments visible as they convected along the slipstream boundary. A 16 MP DSLR camera was used to capture images of the dye as it convected away from the rotor.

The dye flow visualization is the only part of this study that utilized the two-bladed rotor. Because of the limitations on the strength of the Nylon material used for the blades, this rotor could only be operated at relatively low rotational frequencies (up to 100 rpm).

2.5.2 Single-Phase Flow Visualization

Although mostly used as a stepping stone to doing PIV, single-phase flow visualization in a seeded flow provided good insight into the overall rotor flow. This technique also used the 16 MP camera, but instead of using dye as a tracer medium, fine polyamide 12 Nylon seed particles (Vestosint 2070) were uniformly distributed in the tank. The particles were illuminated using a laser light sheet in continuous wave mode. This unsynchronized system of camera and laser makes exact timing impossible, but long exposure imagery was possible. By keeping the shutter of the camera open for relatively long periods of time (∼3 − 4 seconds), the illuminated particles traced out long streaks, showing the time-history of the flow. This time-history allowed the evolution of the general characteristics of the wake generated by the rotor to be better understood.

2.5.3 Dual-Phase Flow Visualization

Dual-phase flow visualization was undertaken by dispersing the Nylon particles in the water, with the glass or steel microspheres being used for the sediment. Before starting the rotor, a level bed of sediment particles approximately one centimeter thick was formed on the ground plane. The rotor was started, and images were taken as the rotor began to mobilize the sediment. After a run was completed, the sediment layer was re-graded.

The dual-phase flow visualization taken for this research was used to study both the process of sediment uplift and the amounts of sediment entrained. By measuring the intensity of each pixel in a flow visualization image (see Fig. 2.7(a)) and applying a thresholding filter, sediment particles could be identified (see Fig. 2.7(b)). The total area of the image that was covered by sediment provided a quantitative assessment of the quantity of suspended sediment. Some of the Nylon tracer particles were in each measurement, but the total contribution to the threshold area was relatively small. This contribution (or error) was measured by thresholding an area

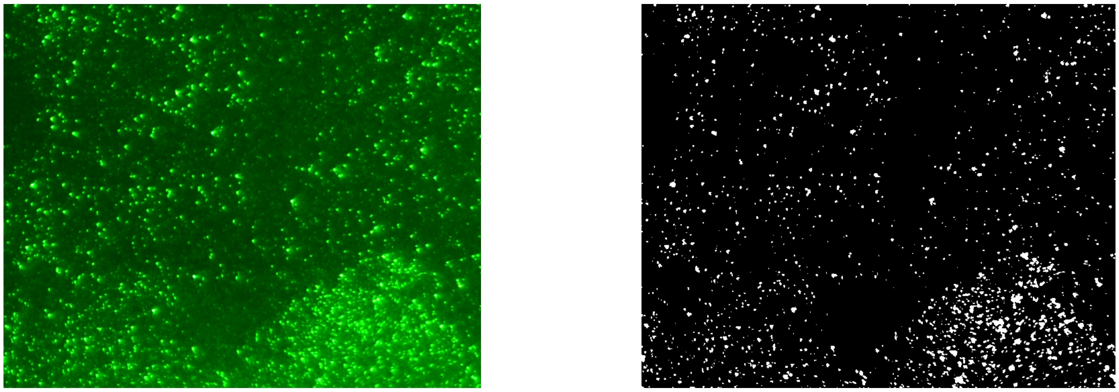

(a) Raw dual-phase flow visualization image.

(b) Threhsolded particle image.

Figure 2.7: Dual-phase flow visualization analysis.

of the image without suspended sediment, and was found to be 0.035%. The results of this analysis were then reported as a fraction of the total image obstruction, which is defined as the area in a region covered by sediment particles to the total area of that region.

2.6 Particle Image Velocimetry (PIV)

Particle image velocimetry (PIV) is a non-invasive flow diagnostic method that can measure the velocity field of a fluid in a given region [51,52]. The present study used several methods of PIV to determine the flow characteristics. As discussed in Section 2.3, two regions of interest (ROI) were used. The present section describes time-averaged, phase-averaged, and instantaneous PIV techniques used to measure the flow conditions beneath the rotor.

2.6.1 Methodology

PIV requires that the fluid be seeded so that the motion of the fluid can be rendered visible. In this research, the flow was seeded with small Nylon tracer particles, as previously discussed. The particles chosen were selected because of their small size and neutral buoyancy in water, which meant that they could follow the flow and still be large enough to scatter light when illuminated by the laser.

A Nd:YAG dual cavity laser with a maximum output of 100 mJ per pulse was used to generate the laser sheets. The invisible 1064 nm light emitted from the laser was frequency doubled to a length of 532 nm (visible in the green spectrum). The beams emanating from the lasers were passed through a series of cylindrical lenses that generated a light sheet, that was measured to have a thickness of less than 2 millimeters at its waist. Images were recorded using a 4 MP CMOS camera with a viewing axis that was orthogonal to the laser sheet and focused on the selected ROI (Fig. 2.5). The operation of the laser and camera were synchronized using a timing hub and a 500/rev encoder to obtain precisely timed images.

Successful PIV requires the capture of two precisely timed images taken in quick succession. The two captured images (frames A and B) are separated by a known pulse separation time, Δt. To calculate the velocity fields, each image frame is first sub-divided into many smaller interrogation windows of a given size. The window size utilized in processing the present images was 24×24 pixels. The interrogation window from the same location in both frames A and B were then compared. To calculate the velocities of the tracer particles in the window, a cross-correlation algorithm was used to measure how the unique pattern of particles in frame A changed relative to frame B. This correlation sequence is repeated for each set of interrogation windows for each set of images. Once the displacement of each particle within the flow is measured, the distance traveled is divided by the pulse separation time, and the velocity field is determined.

The calculation process was conducted using a FFT correlator, and a Rohaly-Hart analysis was used to refine cross-correlation and improve results [53]. The cross-correlation methods used in this research used a deformation grid algorithm, as discussed in depth by Scarano [54]. The velocity vectors were further validated using a universal median test, and only images that contained fewer than 5% spurious vectors were used in subsequent analysis. The good accuracy of the measurements resulted in spatial resolution of 81 vectors per square centimeter, or 14 vectors per blade chord length.

2.6.2 Time-Averaged PIV

In time-averaged PIV, 500 image pairs were taken at several different blade azimuthal angles (ψ). Image acquisition was not synchronized to the blade position. Images were collected by allowing the PIV system to capture image pairs at its maximum repetition rate of 14.5 Hz, with a pulse separation time (Δt) of 575 μs. This repetition rate is several times faster than the rotational rate of the rotor (for rotational rates, see Table 2.1). For the time-averaged flow analysis, only ROI 1 was imaged. A lens with a focal length of 85 mm was trained on the region of interest, and a $20 \times 20\,\mathrm{cm}$ field of view was captured. By performing an ensemble average over the entire set, an average velocity field was determined. The time-averaged velocity field allowed for the calculation of certain parameters needed for the similarity parameters, most notably the characteristic velocity, U_{char} (see Section 1.4).

2.6.3 Phase-Averaged PIV

In this experiment, the laser and camera were synchronized to the rotational rate of the rotor, and images were only captured when the blades were at a pre-defined azimuthal position, ψ. This method required the use of an optical shaft encoder, which identified the blade position and sent the value to a control and synchronization program. The same Nd:YAG laser used for the time-averaged PIV experiments was also used with the 4 MP CMOS camera. When the optical encoder determined that the blade was at the desired blade azimuthal angle, the first laser pulse was triggered, and the two images were recorded.

The phase-averaging method of data collection gave a large set of images with the blade at the same azimuthal angle ψ. A phase-averaged set of data was created by ensemble averaging 150 velocity fields. By capturing PIV images at the same blade azimuthal angle, the location of the tip vortices was similar in each image. Averaging PIV images taken in this manner allows the periodic flow structures to be highlighted. To demonstrate how the flow evolved as the rotor position changed, three blade azimuth angles were studied, $\psi = 10^\circ$, 60°, and 320°.

2.6.4 Instantaneous PIV

Single image-pairs were taken from the phase-resolved data set and the instantaneous velocity fields computed to examine some of the aperiodic flow features that form in the rotor wake.

2.6.5 PIV Challenges

PIV measurements of a rotor flow pose several technical challenges. Laser reflections off of the ground plane were one of the greatest challenges to overcome. Light that reflected or refracted from the rotor, ground plane, or tank walls could scatter throughout the tank, causing overexposed regions in the image. Overexposure in an image can mask individual seed particles, preventing successful cross-correlations.

The reflection most difficult to mitigate was off of the ground plane, but this is the very region where sediment mobilization and transport occurs. Judicious alignment of the laser sheet was, therefore, necessary to reduce reflections as much as possible. Figure 2.8(a) shows the second region of interest (ROI 2) just above the ground plane when laser reflections are strong. Figure 2.8(b) shows the result of good laser alignment; surface reflections in this case are significantly reduced, and will allow better measurements.

Seeding of the water can also be a challenge when performing PIV. If too few seed particles were added to the tank, poor cross-correlations would be obtained. However, over-seeding can also be a problem. Too many particles creates a situation

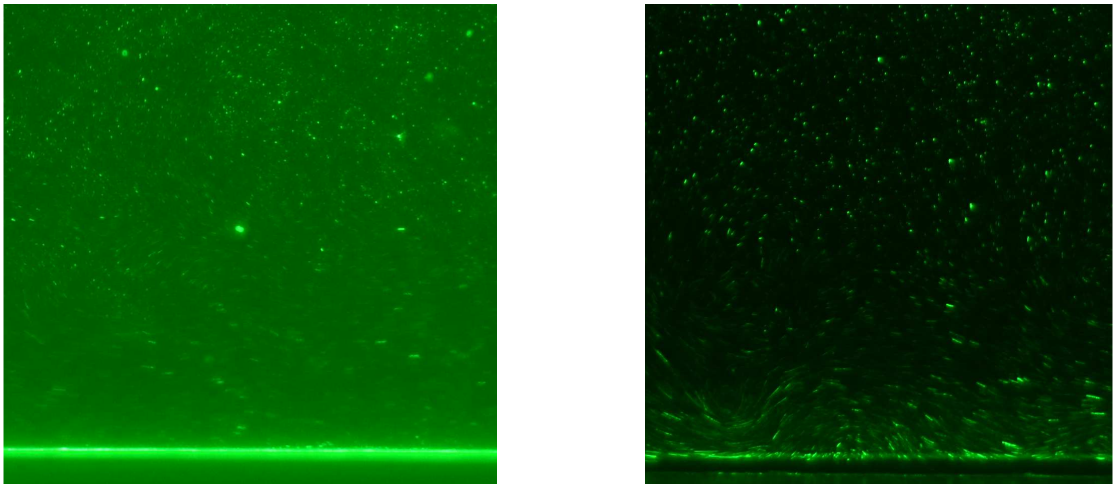

(a) Laser light sheet reflection at the ground due to poor laser alignment.

(b) Reduction of reflections after laser alignment.

Figure 2.8: Reduction of laser light reflections near the ground through careful alignment of the laser light sheet.

where individual seed particles can no longer be discerned from others. Furthermore, if too many particles are added to the water, they are impossible to remove. Instead, some or all of the tank must be drained and refilled with clear water to dilute the concentration of seed particles. Also problematic is the natural occurrence of minerals, dissolved gases, and other contaminants in the water used in the tank. These contaminants can make the water semi-opaque, an effect that can sometimes be mitigated by allowing the water tank to settle for several hours.

Determining the proper settings for the camera, laser, and rotor can be another challenge. A careful selection of the laser pulse separation time, for instance, is important; this is because too short a separation time results in sub-pixel displacements of the seed particles, which makes it difficult for the cross-correlation algorithms to detect particle movement. Too large a Δt, however, results in seed particles traveling too far, or even out of the laser sheet entirely, which can cause errors in the measurements of the flow velocities.

2.6.6 Uncertainties in PIV

There are many potential sources of uncertainty in the flow measurements using PIV. Sources can include particle tracking errors, background image noise, interrogation window size, as well as several other factors [51, 59]. Tracking errors are the result of seed particles that are not able to perfectly respond to changes in flow speed or direction. Usually, the larger the inertia of the seed particle, the less able it will be to follow the flow. Images taken by digital cameras will have some amount of sensor noise. The noise detected by the camera's CCD array can cause false peaks in the algorithms that detect and correlate particle motion. This is especially true where the signal-to-noise ratio is low (sometimes caused by images taken with too much ambient light or otherwise overexposed). Another source of error in the PIV measurements is the uncertainty in the magnification factor, M, caused by lens aberrations or uneven magnification. This effect can be mitigated by calibration plates, which allow the software to account for aberrations. Errors in the calibration of the pixel size to physical dimensions can cause some errors in calculated velocities. Finally, there is some uncertainty (usually very small) in the pulse separation time.

For this work, the uncertainty from measured velocity fields, values of pulse separation time Δt, and magnification factor, resulted in a total propagated uncertainty of the flow velocity measurement of about 5%. This uncertainty was calculated using

$$\Delta U = \sqrt{\left(\Delta\varepsilon_{\Delta x}\frac{\partial U}{\partial \Delta x}\right)^2 + \left(\varepsilon_{\Delta t}\frac{\partial U}{\partial \Delta t}\right)^2 + \left(\varepsilon_M\frac{\partial U}{\partial M}\right)^2}$$

where $\varepsilon_{\Delta x}$, $\varepsilon_{\Delta t}$, and ε_M are the uncertainties in the pixel displacement, pulse separation time, and magnification factor, respectively [60].

2.7 Identification of the Locations of the Vortices

Determining the location of the trailed vortices was vital for measuring the vortex characteristics. While qualitative observation of the PIV velocity fields is sufficient to determine approximate locations of the vortices, a quantitative methodology was required to accurately measure the vortex core position. Given the PIV-measured velocity fields, several methods of vortex identification were used to locate the vortex cores.

2.7.1 Vorticity

One way of calculating the locations of the vortices in a flow is through the calculation of the vorticity within the flow field. Vorticity is a measure of the circulation in the fluid. Vorticity is defined mathematically as the curl of a velocity field, i.e., $\vec{\omega} = \vec{\nabla} \times \vec{v}$. After calculating the vorticity in the velocity field, vortices are defined as areas of concentrated vorticity, the center of the vortex is at the location of highest vorticity.

2.7.2 Q-Criterion

While the use of vorticity is one way of determining the location of a vortex, some inaccuracies in measuring vortex location may arise because the calculated vorticity field can also be affected by the velocity gradients or shear layers in the flow. Several methods for vortex identification exist that account for regions with shear layers or altered velocity gradients. One such method is the Q-criterion algorithm. Developed by Hunt et al. [61], the Q-criterion defines a vortex as a region where the norm of the vorticity tensor dominates the rate of strain. The Q-value is calculated by finding the discriminant of the velocity gradient tensor, as given by

$$Q = \frac{1}{4}S^2 - q \tag{2.2}$$

where S is the trace of the velocity gradient tensor

$$S = \frac{\partial u}{\partial x} + \frac{\partial v}{\partial x} \tag{2.3}$$

and q is the determinate of the velocity gradient tensor, given by

$$q = \frac{\partial u}{\partial x}\frac{\partial v}{\partial y} - \frac{\partial u}{\partial y}\frac{\partial v}{\partial x} \tag{2.4}$$

The velocity gradients were calculated using the Richardson extrapolation where

$$\left(\frac{\partial f}{\partial x_i}\right) \approx \frac{f_{i-2} - 8f_{i-1} + 8f_{i+1} + f_{i+2}}{12\Delta X} \tag{2.5}$$

The Richardson extrapolation method provides an accuracy $\sim O(\Delta X^3)$, and an uncertainty $\approx 0.95\varepsilon/\Delta X$. Vortex centers are located at the maximum positive peak of Q for each vortex.

2.7.3 Γ-Method

Another method for vortex identification is the Γ-method [62]. This method utilizes a proper orthogonal decomposition (POD) to separate the turbulent fluctuations from unsteady swirling motion. This decomposition is then used in either of two vortex identification functions. These functions can be used to either identify the location of a vortex center or to compute the size of the vortex core. In the present research, the second function was used to visualize the vortices present in the flow. By this method, a vortex is defined as a region where $\Gamma \geq 0.6$, where Γ is defined as

$$\Gamma(x,y) = \frac{1}{N}\sum_{S} \frac{\left[\mathbf{PM} \times (\mathbf{U}_M - \tilde{\mathbf{U}}_P)\right] \cdot z}{\|\mathbf{PM}\| \cdot \left\|\mathbf{U}_M - \tilde{\mathbf{U}}_P\right\|} \tag{2.6}$$

In Eq. 2.6, N is the number of points inside S, the two-dimensional area surrounding P, a fixed point in the measurement domain. M is a point that lies in S, and $\mathbf{PM}$ represents the radius vector linking M to P. $\mathbf{U}_M$ is the velocity vector found at the measurement location and $\tilde{\mathbf{U}}_P$ is the local convection velocity around P. $\tilde{\mathbf{U}}_P$ can be calculated from

$$\tilde{\mathbf{U}}_P = \frac{1}{S}\int_S \mathbf{U}\,\mathrm{d}S \tag{2.7}$$

Finally, z is the unit vector normal to the measurement plane. Further information about the POD vortex core identification method can be found in [62].

2.8 Summary

This chapter has described the experimental setup and methods used in the course of the current work. The water tank, rotor setup, ground plane, seeding, and sediment particles were described. The flow visualization techniques, as well as particle image velocimetery principles were discussed, and the equipment used in each case has been described. The methods of collecting time-averaged, phase-averaged, and instantaneous velocity field measurements were explained, and some vortex identification methods were also discussed.

Chapter 3

Results

3.1 Overview

The present chapter presents the findings from the flow visualization and particle image velocimetry in the single-phase and dual-phase flow environments. Flow visualization was used to examine the rotor wake flow near the ground, and to qualitatively study the effects of changing the scaling parameters on the resulting two-phase flow environment. Flow visualization was vital for determining regions of interest for further study using particle image velocimetry (PIV) techniques. Time-averaged and phase-averaged PIV measurements were then made, and the data was used to calculate different values of the fluid scaling parameters that were used.

3.2 Single-Phase Flow Visualization

3.2.1 Dye Flow Visualization

Dye flow visualization was used to examine the flow structures beneath a two-bladed rotor operating in ground effect. Flow visualization was performed by introducing concentrated dye near the tip-path-plane (TPP) of the rotor such that the dye became entrained into the blade tip vortices. These dye flow experiments were performed at significantly lower rotational rates (80 rpm) than the later tests

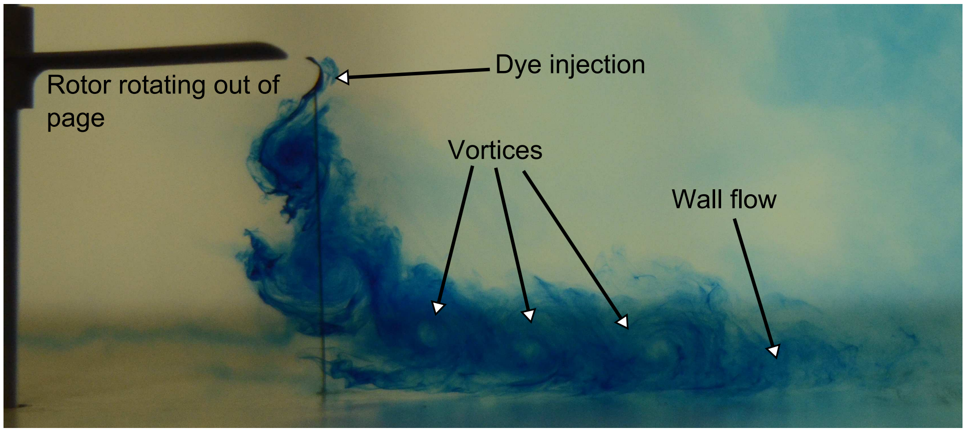

Figure 3.1: Dye flow visualization (side view).

because the two-bladed rotor was structurally less stiff than the single-bladed rotor.

In addition to locating areas of interest for later study, the initial flow visualizations with the two-bladed rotor provided examples of the flow structures expected from the rotor in ground effect operation. Figure 3.1 shows a representative flow visualization image from a side view. In this case, the rotor plane was at a height of one rotor radius above the ground plane, and the dye was injected from a thin (24 gauge) needle protruding from the ground plane to a point very close to the TTP of the rotor.

The most dominant features in the flow are clearly the blade tip vortices. As each rotor blade moves through the water, it trails a helical tip vortex. Figure 3.2 shows a perspective view of the rotor flow. Each element of the vortex can be identified by the roughly spiral or helicoidal pattern it produces. Initially, the wake contracts below the rotor, but as it nears the ground plane, the wake and the vortices quickly expand and convect outwards. As the vortex filaments convect along the ground, they are also stretched, which intensifies their vorticity and increases

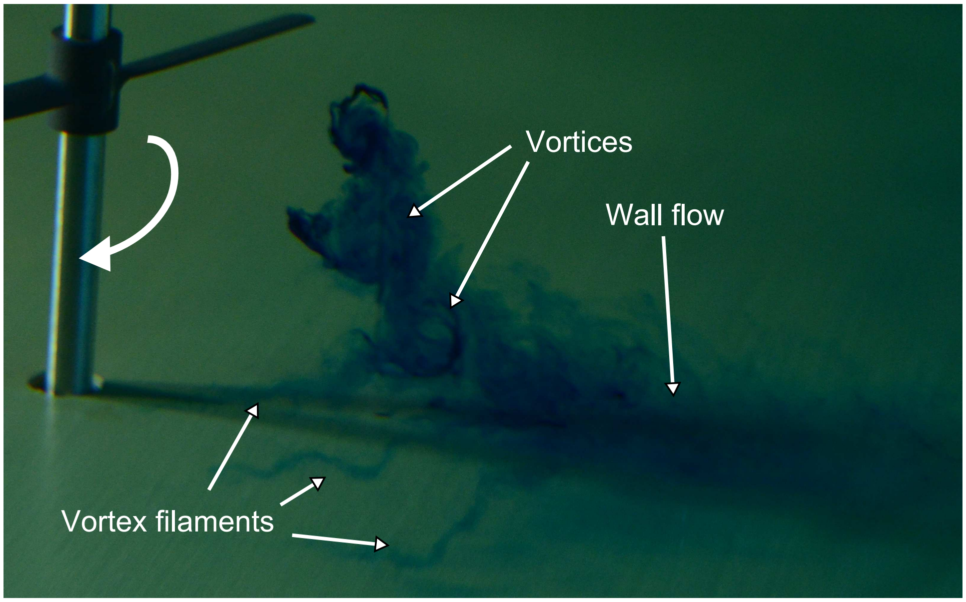

Figure 3.2: Dye flow visualization (isometric view).

the local swirl velocities. Stretching allows the vortex filaments to persist longer than they would out of ground effect (for more information on this effect, see Section 1.2.1). Eventually, the vortices diffuse and merge with other features of the downwash field formed by the rotor to form a wall jet over the ground plane.

Of particular interest in this study was the unsteady nature of the vortex filaments as they approached the ground plane. In Fig. 3.2, aperiodic disturbances in the vortex filaments are visible. When two adjacent turns of the helicoidal tip vortex move closer to each other, they may pair and merge, combining their strength and causing significant velocity fluctuations in the local flow. It was found using the flow visualization (and later by means of particle image velocimetry) that higher rotational rates of the rotor can increase the tendency for pairing to occur. This effect has also been noted in prior work by Sydney and Leishman [16]. Increased vortex pairing at higher rotational rates occurs because adjacent turns of the helical vortex filaments become spatially closer together, which leads to increased flow interactions. The frequency of vortex pairing is directly related to the blade passing frequency; a rotor with more blades is more likely to produce a wake with a greater susceptibility to vortex pairing. In later testing of a one-bladed rotor, pairing and merging events were found to occur less often.

3.2.2 Seeded Flow Visualization

Flow visualization on a single-bladed rotor was conducted by seeding the water in the tank with Nylon particles (Vestosint 2070) and illuminating a plane in the flow using a laser sheet generated by a 1 W continuous wave laser. This method of flow visualization allowed for a more complete view of the flow field because the tracer particles were more evenly distributed throughout the fluid, rather than injected at a single point as was used in the dye flow visualization.

Figure 3.3 shows an example of the flow visualization images captured during testing. In this example, the rotor is rotating at 100 rpm ($Re_{\text{tip}} = 1.33 \times 10^4$). Sections of the tip vortex are visible in the image as particle streaklines. The vortices form at the tip of the rotor blade (out of frame in this image) and follow along the slipstream boundary of the rotor wake. As they convect downwards, the wake below the rotor contracts slightly before encountering the ground plane and expanding outward, as was seen previously in the dye flow visualization (see Fig. 3.1).

Photography using a long exposure was utilized to gain a better understanding of the time-averaged flow. In a long exposure image of the flow, longer streaks in

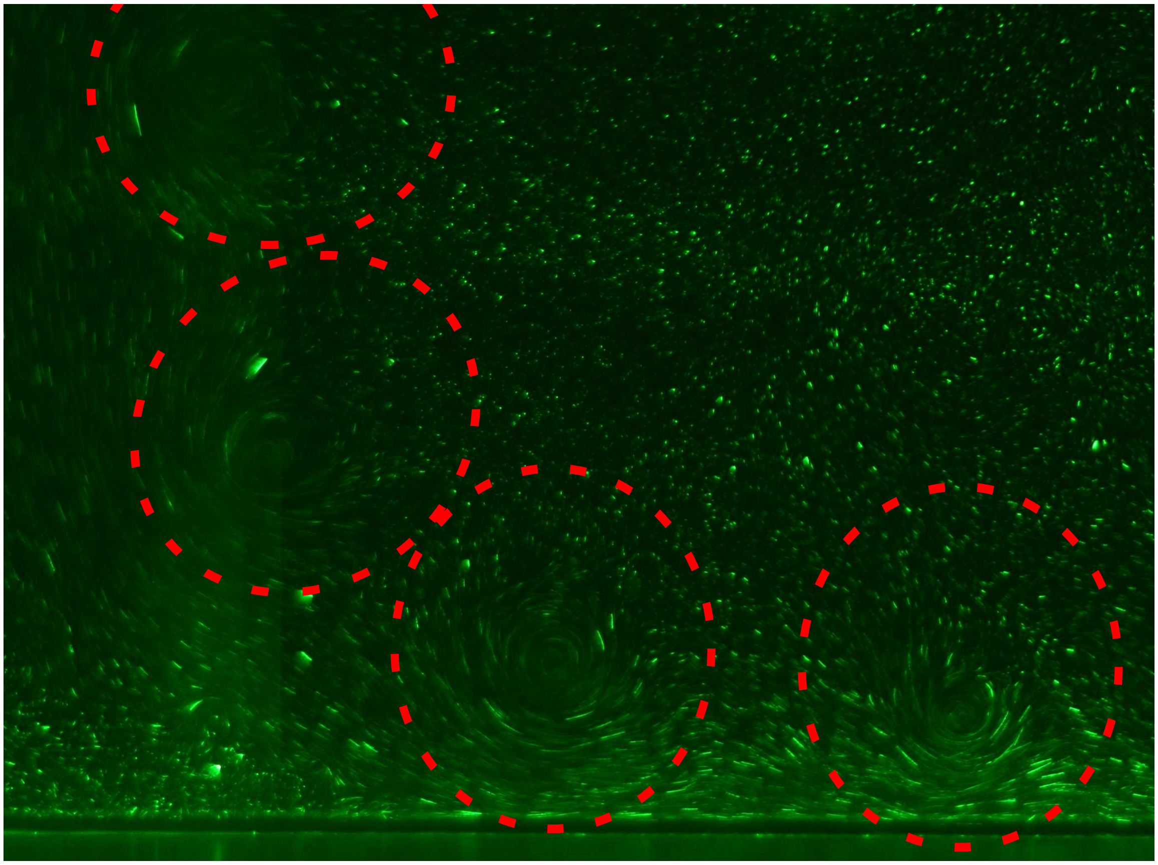

Figure 3.3: Seeded flow visualization (zoomed in and vortices circled for clarity).

the particle tracks usually represent larger flow velocities. Because the laser sheet was relatively thin (approximately 2 mm), longer streaks also indicate a more two-dimensional flow in which the particles stay in the plane of the laser sheet for longer. Short particle tracks represent either very low flow velocities or a flow that had a larger out-of-plane component.

Figure 3.4 shows a partitioning of the different flow regions around the rotor in ground effect. Region 1 is the region of the flow that will pass through the TPP of the rotor. In actual operational brownout conditions, this region of the flow is important because any sediment or dust entrained here will be re-ingested by the rotor. The flow in Region 2 is mostly downwards, but also radially inwards towards the rotor, and sediment suspended in this region would be carried towards the rotor. In practice, any sediment suspended in this region would tend to remain close to the rotorcraft, probably contributing to reducing the pilot's visibility. Region 3 contains mostly downwash produced by the rotor. This downwash flow is turbulent and three-dimensional, as is evident from the short particle streaks. From the flow visualization (e.g., Fig. 3.3), the cores of the trailed vortices are known to flow out along the ground plane on the boundary between Regions 4 and 5. As the vortices pass over the ground plane, the negative (to the left) tangential velocities at the top edge of the vortices combine with the translational velocities of the vortices (to the right), and results in a turbulent mixing zone, marked as Region 4. Near the ground plane (Region 5), the positive (to the right) tangential velocity at the bottom of the vortex adds to the net translational velocity of the vortex flow, causing relatively larger flow velocities to occur at the ground plane.

3.3 Time-Averaged PIV

PIV was used to measure the velocity field produced by the rotor above the ground plane, as well as to obtain a first-order approximation of the values needed for the scaling factors. Baharani [29] and others [16, 30] used a time-averaged characteristic velocity to evaluate several of the two-phase flow similarity parameters thought to be relevant to rotorcraft brownout (e.g., the densimetric Froude number, friction threshold velocity, and terminal velocity). To compare the results from the

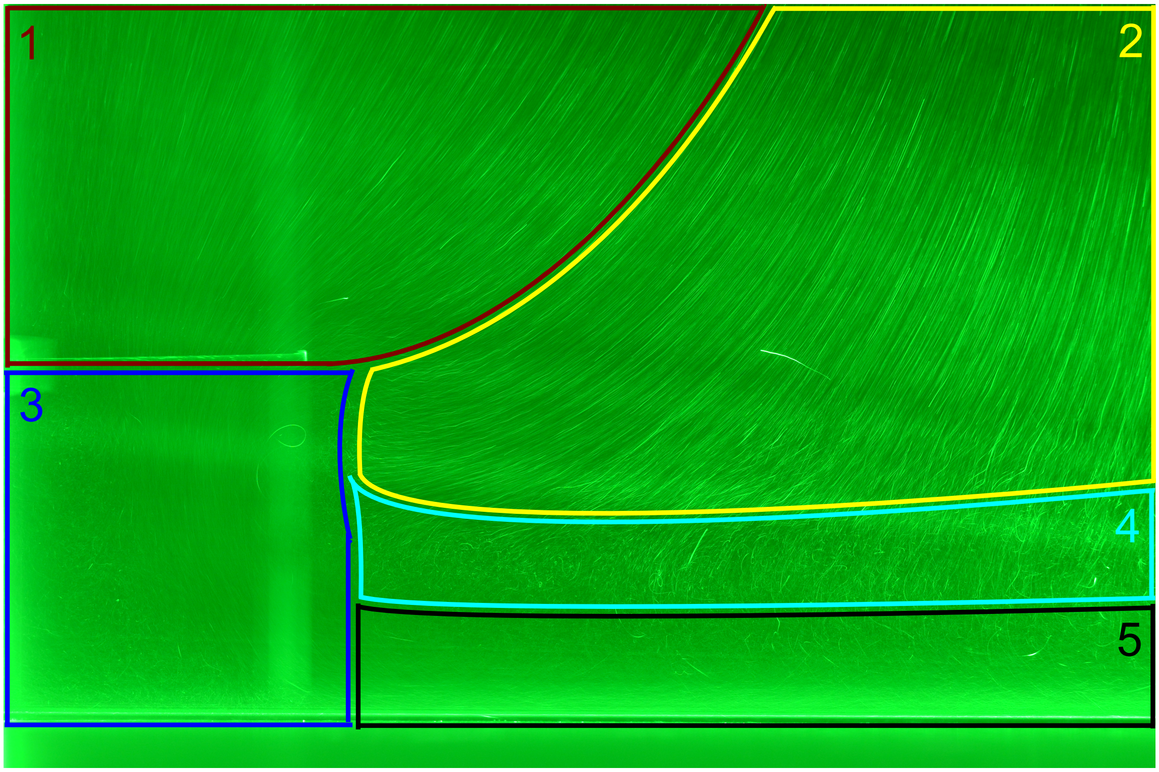

Figure 3.4: Long exposure photograph of the flow with the rotor at 100 rpm ($Re_{\text{tip}} = 1.33 \times 10^4$).

present work with the previous work, time-averaged velocity field measurements of the flow were acquired.

Figure 3.5 shows the normalized time-averaged total velocity (i.e., $|V_{\text{total}}| = \sqrt{u^2 + v^2}/\Omega R$) field in ROI 1 for the rotor operating at 120 rpm ($Re_{\text{tip}} = 1.60 \times 10^4$). The streamlines in this image have been created by drawing lines tangential to the calculated velocity vectors. The rotor is located at a nondimensional height of $z/R = 1$, with the tip of the rotor blades at $y/R = 1$. Higher flow velocities are shown in red and lower velocities in blue. As shown previously in the long exposure flow visualization, the flow curved towards the edge of the TPP before being convected downwards.

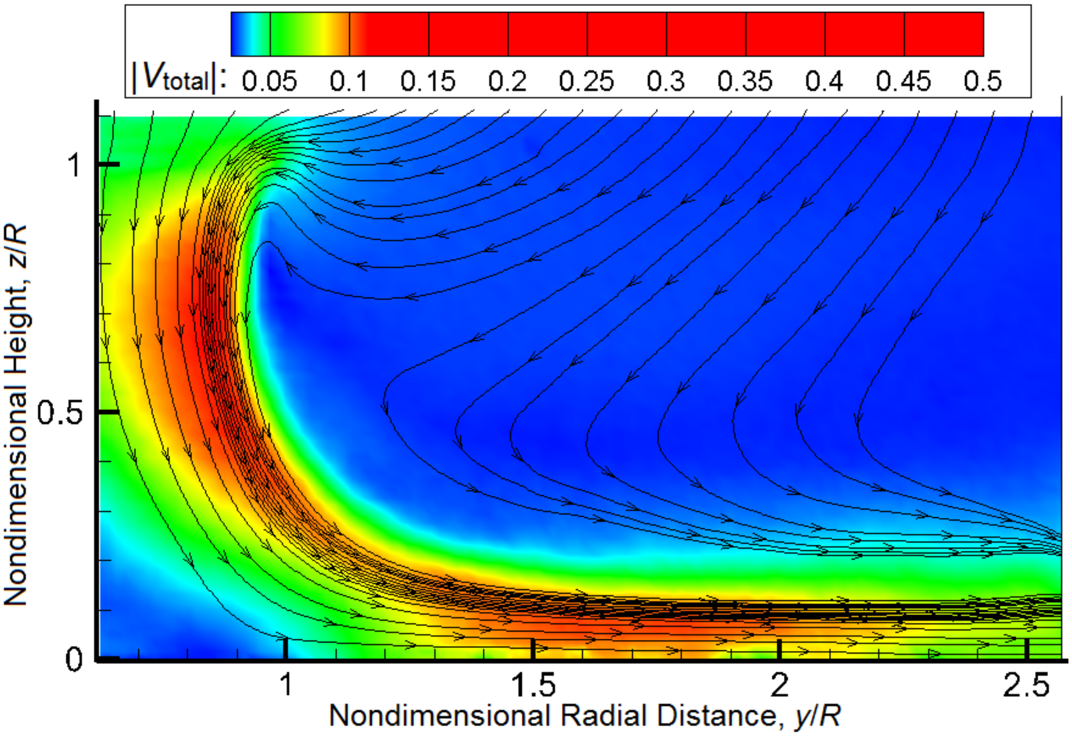

Figure 3.5: Time-averaged total velocities in ROI 1 with the rotor at 120 rpm ($Re_{\text{tip}} = 1.60 \times 10^4$). (Total velocity: $|V_{\text{total}}| = \sqrt{u^2 + v^2}/\Omega R$)

The two-phase flow visualization (presented later in Section 3.6) revealed that the region of maximum sediment uplift was between $y/R = 1.25$ and $y/R = 2.60$, i.e, in ROI 2. Figure 3.6 shows the normalized total velocity in ROI 2 for the single-bladed rotor operating at 100 rpm ($Re_{\text{tip}} = 1.33 \times 10^4$). The time-averaged velocity field near the ground is shown, and for clarity only every 10th vector along the abscissa and every other vector along the ordinate is plotted. Figure 3.7 shows radial velocity profiles for the flow under the rotor at the same operating conditions (100 rpm, $Re_{\text{tip}} = 1.33 \times 10^4$) at non-dimensional radial distances of $y/R = 1.7$, 2.0, 2.3, and 2.57. The radial velocity slows near the ground, reaches a maximum velocity at approximately 1/10th of a rotor radius above the ground, and is nearly zero at

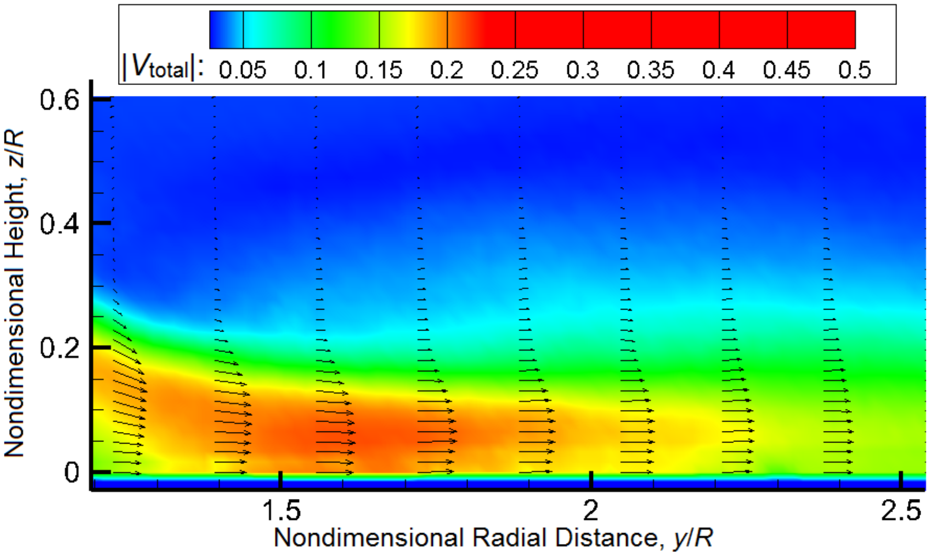

Figure 3.6: Time-averaged total velocities in ROI 2 with the rotor at 100 rpm ($Re_{\text{tip}} = 1.33 \times 10^4$). (Total velocity: $|V_{\text{total}}| = \sqrt{u^2 + v^2}/\Omega R$.)

rotor heights greater than 1/2 of a rotor radius. The shape of the time-averaged velocity profiles was found to be similar for all of the radial distances shown here, although the maximum velocity measured in the wall jet decreased as y/R increased.

3.4 Phase-Averaged PIV

When compared to the dye flow visualization, it became evident that the velocity field measurements obtained by the time-averaging method were a poor representation of the actual flow conditions in the rotor wake (see Fig. 3.1). As a rotor blade passes through the imaging plane, it leaves behind an element of a tip vortex, which is visible in the dye flow visualization (see Fig. 3.1) but not in the time-averaged velocity field (see Fig. 3.5).

To quantitatively resolve these flow features, phase-averaged measurements

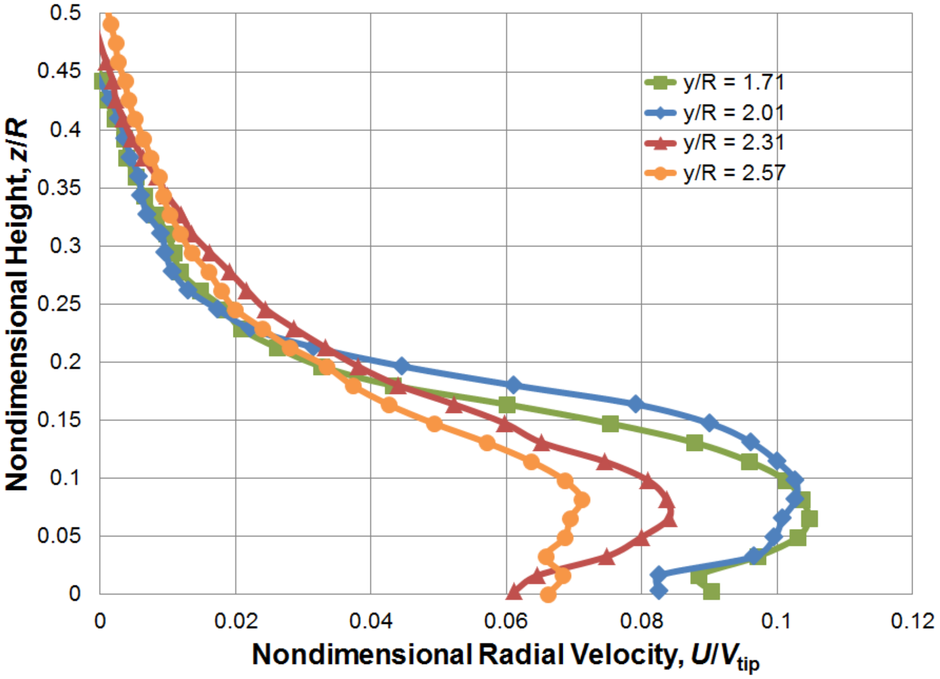

Figure 3.7: Radial velocity profiles at $y/R = 1.7$, 2.0, 2.3, and 2.57 in the velocity field shown in Fig. 3.6.

were acquired with the rotor at selected rotor azimuthal positions, ψ. By capturing a series of images at the same blade azimuthal position, elements of the tip vortex filament appeared to be in (nearly) the same spatial locations. Once a set of data large enough to provide statistical significance (at least 150 image pairs) was acquired, the velocity fields were computed and then ensemble averaged. This flow measurement technique gives a measure of the periodic flow velocity fluctuations in the rotor wake.

Three rotor phase angles (or degrees from the beginning of a revolution) were used for the phase-averaged PIV, and in this case were at $\psi = 10^\circ$, 60°, and 320° (see Fig. 2.4). These angles allow for the flow to be observed before the blade passes through the field of view ($\psi = 320°$), just after it begins a new revolution ($\psi = 10°$), and further into its rotation ($\psi = 60°$). While each turn of the tip vortex filament follows the same general path, turbulence introduces some uncertainty in the spatial position of any given vortex element. This behavior affects the phase-averaged profiles to some degree. In general, the velocities phase-averaged over all PIV realizations will be somewhat lower than what is expected in an instantaneous velocity field [16, 29, 30].

Figure 3.8(a) shows the phase-averaged radial velocity fields in ROI 1 for a single-bladed rotor at $\psi = 320°$ operating at 100 rpm ($Re_{\mathrm{tip}} = 1.33 \times 10^4$). Note that the rotor's axis of rotation is at $y/R = 0$. The colors represent the radial velocity at each location in the flow, with red representing flow moving away from the rotor shaft (to the right), and blue showing flow moving towards the rotor shaft (to the left). Vortices appear as red/blue pairs in the flow field. Five vortices are visible in Fig. 3.8(a). Their spatial locations were determined by finding the maximum Q of each vortex utilizing the Q-criterion, and then verified using the Γ-method (see Section 2.7). To visualize the size and locations of each element, contours of $\Gamma = 0.6$ are overlaid in black.

Figure 3.8(b) shows the phase-averaged and time-averaged radial (outward) velocities at $y/R = 1.7$, which is marked with a vertical gray line in Fig. 3.8(a). The velocity profiles are shown from the ground plane to a non-dimensional axial height of $z/R = 0.5$. At this blade azimuthal angle there is a portion of the tip vortex present near $y/R = 1.6$, but the core is still to the left of the velocity profile cut at $y/R = 1.7$. The phase-averaged velocity profile is similar to the time-averaged

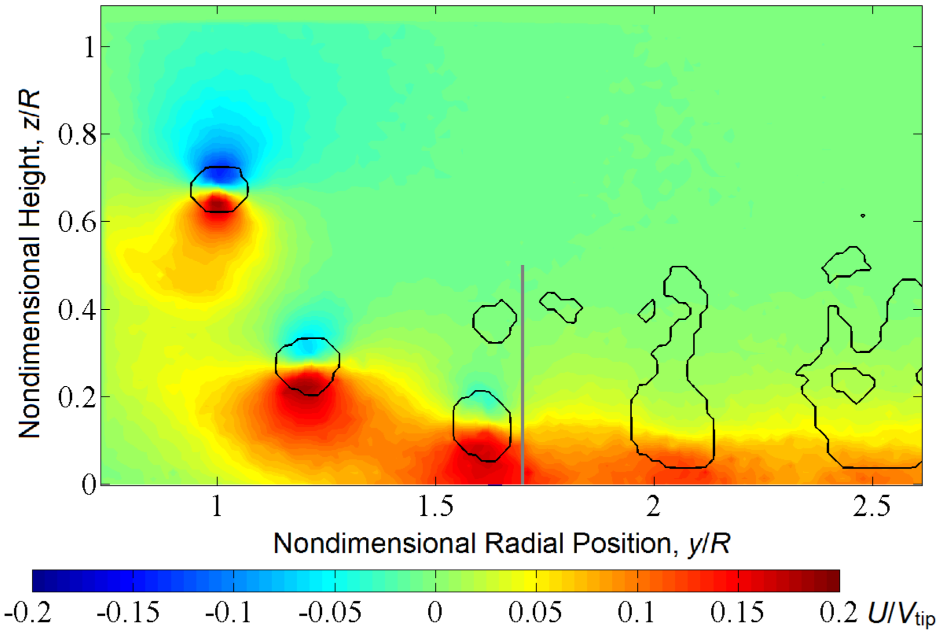

(a) Radial velocity field

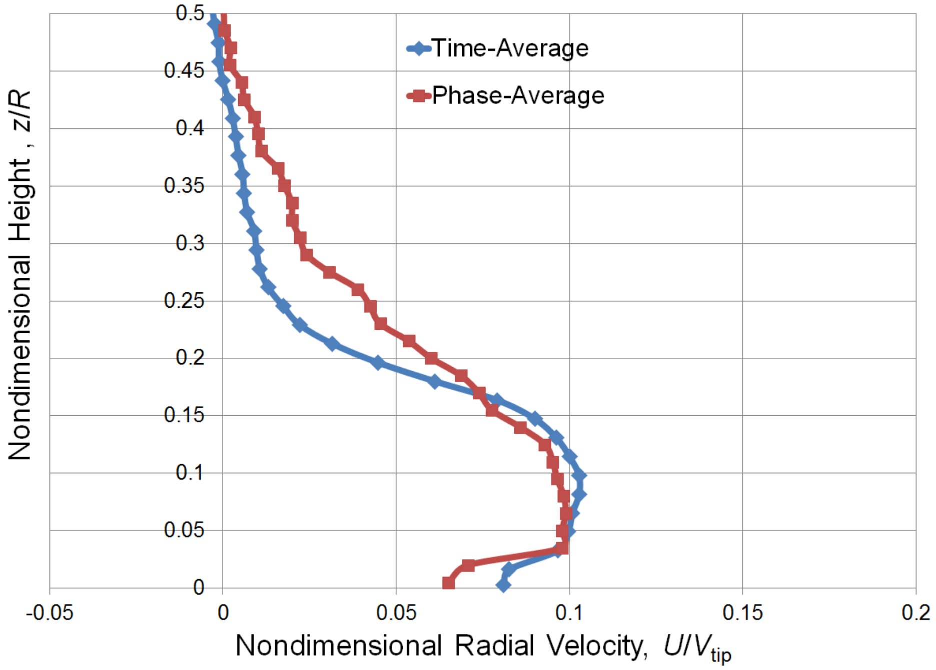

(b) Radial velocity profile for $\psi = 320°$ at $y/R = 1.7$

Figure 3.8: Phase-averaged radial flow velocities with the rotor operating at 100 rpm ($Re_{\text{tip}} = 1.33 \times 10^4$) and $\psi = 320°$.

profile, with a few differences. Very close to the ground plane, the velocities are lower in the phase-averaged case compared to the time-averaged case. The velocity then increases further from the ground plane to a maximum near the maximum seen in the time-averaged case. This results in steeper velocity gradients near the wall (and is commensurate with increased shear stresses) and so the flow there is more likely to uplift and entrain sediment particles. As previously discussed, sediment particles will resist movement until a certain threshold velocity has been reached; the higher velocities produced near a tip vortex are more likely to mobilize and entrain sediment.

Figure 3.9(a) shows the phase-averaged flow field at a blade azimuthal angle of $\psi = 10^\circ$. Here 50° of blade rotation has elapsed compared to that shown in Fig. 3.8(a) and a vortex is positioned directly over the ground at $y/R = 1.7$. The passage of this vortex has produced a velocity excursion from the average flow and a region of reverse flow at axial heights above $z/R = 0.25$. Figure 3.9(b) shows that the passing vortex produced velocities that were more than 50% higher than the time-averaged values. This higher velocity along the ground is one reason that loose sediment on the ground is more likely to be mobilized during a vortex transit.

After the vortex has passed (see Fig. 3.10, $\psi = 60^\circ$), the phase-averaged velocity profile returns to a shape similar to those of the $\psi = 320^\circ$ case (see Fig. 3.8(b)) and the time-averaged case (see Fig. 3.7). While this trend is observed whenever a vortex is not directly over a measurement location, time-averaging is not generally representative of the flow field found under a rotor in ground effect because the excursions are large when the vortex is present. The phase-averaging results highlight

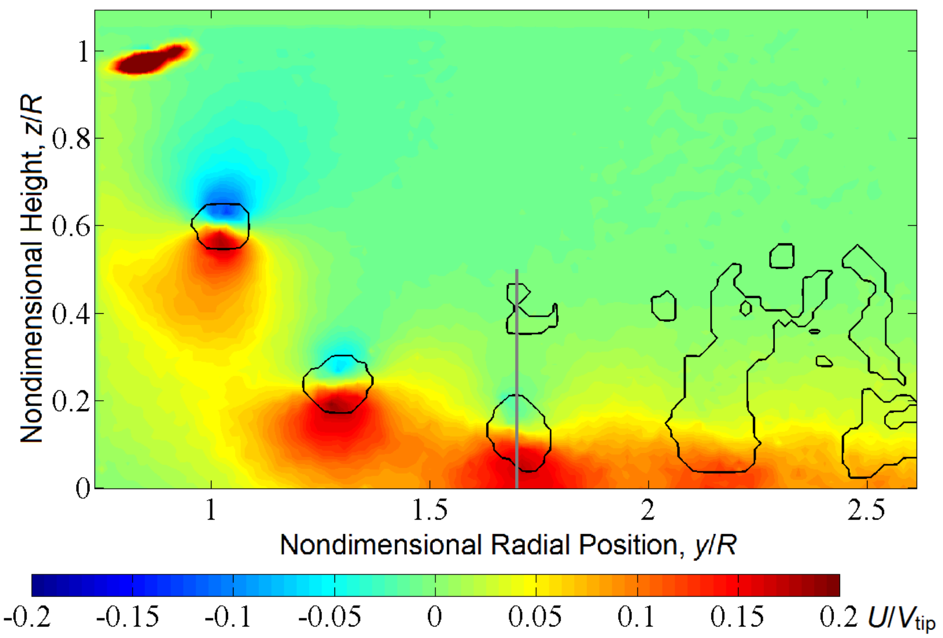

(a) Radial velocity field

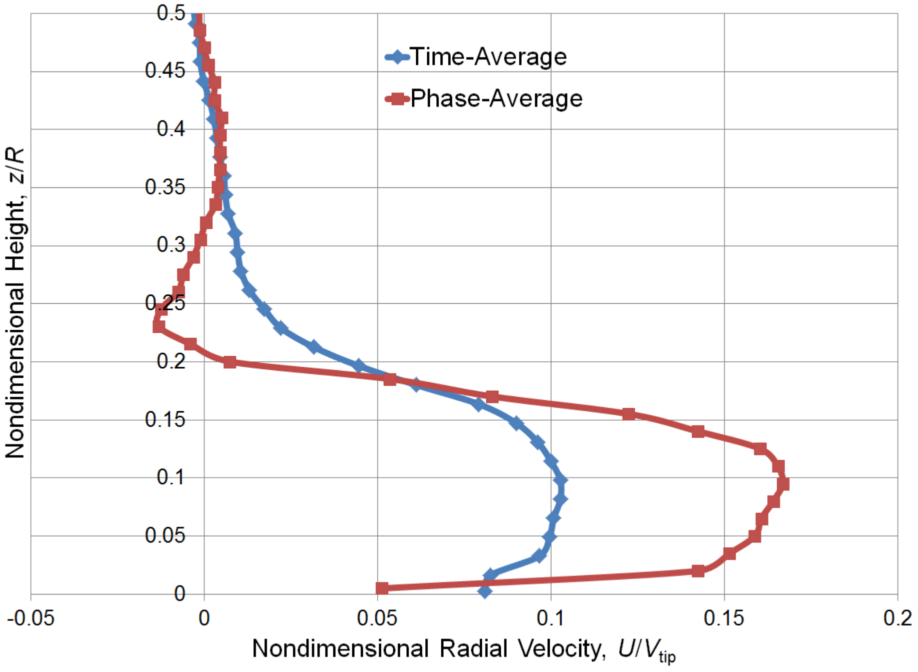

(b) Radial velocity profile for $\psi = 10°$ at $y/R = 1.7$

Figure 3.9: Phase-averaged radial flow velocities with the rotor operating at 100 rpm ($Re_{\text{tip}} = 1.33 \times 10^4$) and $\psi = 10°$.

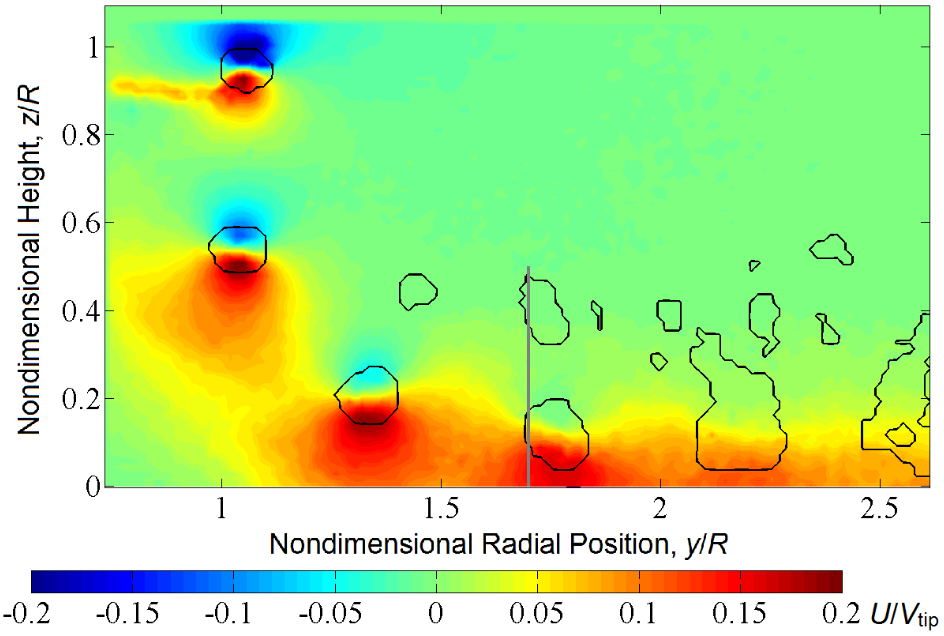

(a) Radial velocity field

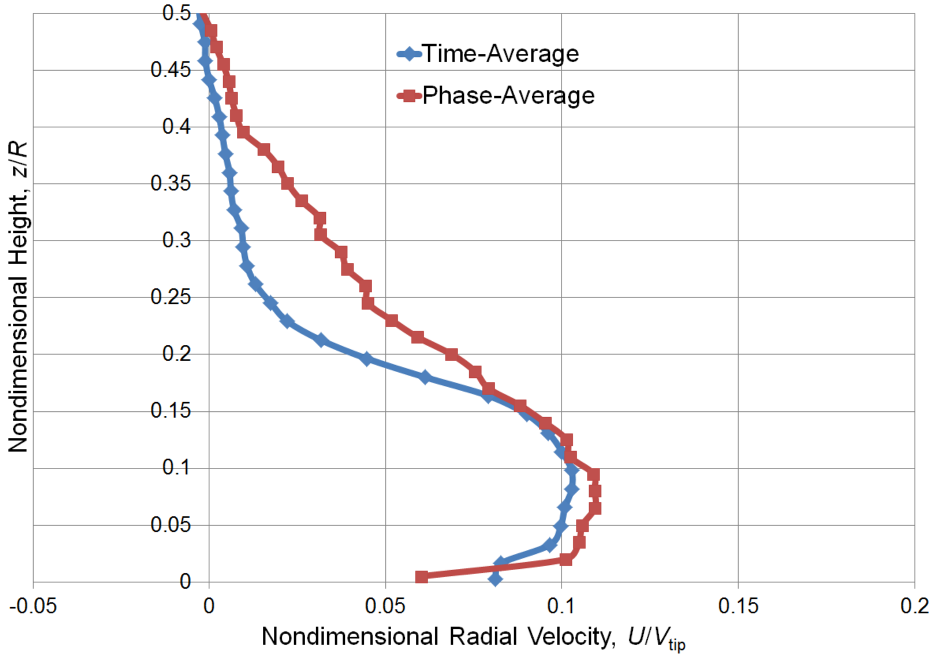

(b) Radial velocity profile for $\psi = 60°$ at $y/R = 1.7$

Figure 3.10: Phase-averaged radial flow velocities with the rotor operating at 100 rpm ($Re_{\text{tip}} = 1.33 \times 10^4$) and $\psi = 60°$.

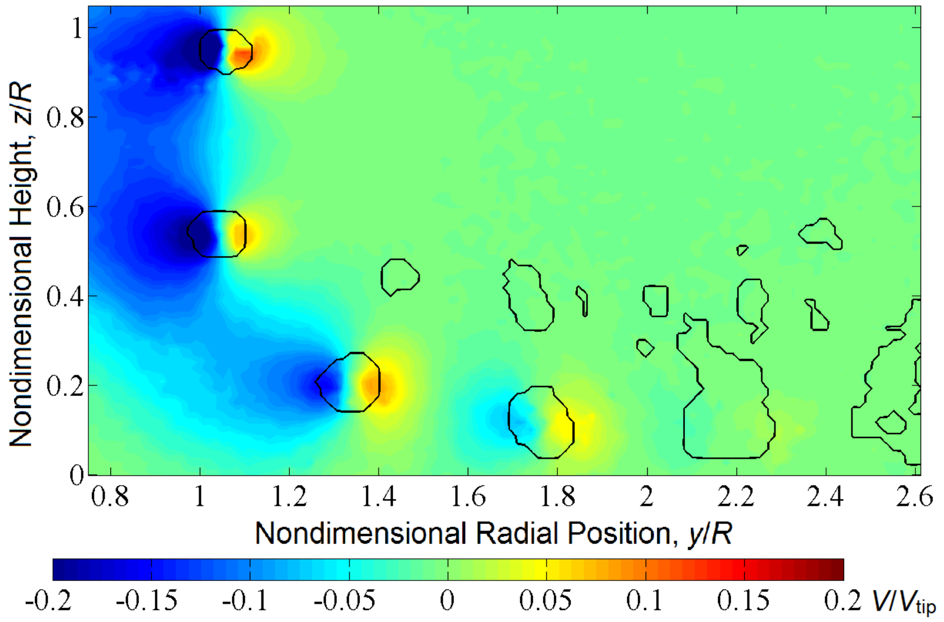

(a) Axial velocity field

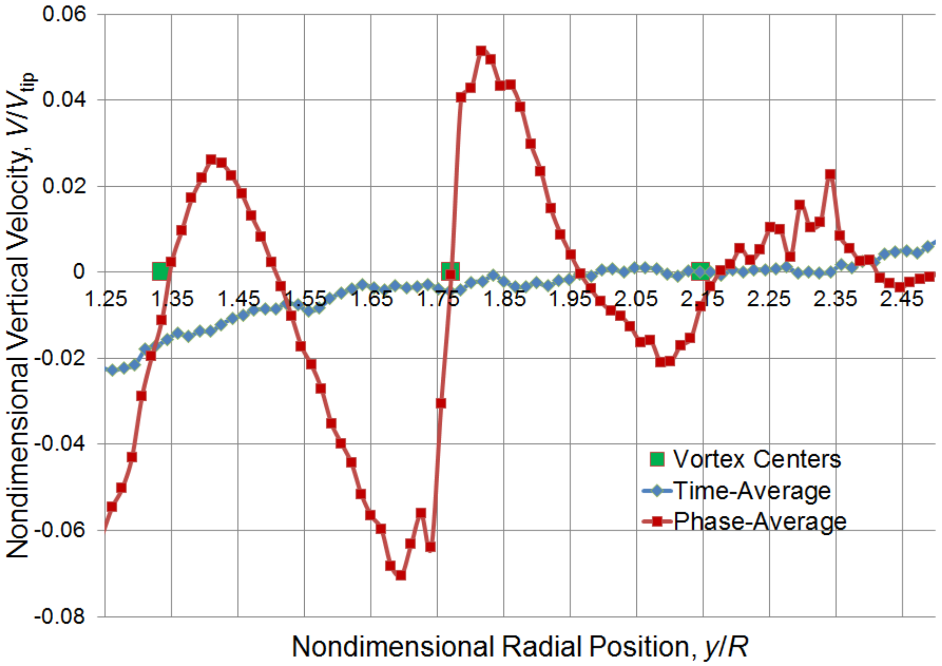

(b) Axial velocity profile for $\psi = 60°$ at $z/R = 0.1$

Figure 3.11: Phase-averaged axial flow velocites with the rotor operating at 100 rpm ($Re_{\text{tip}} = 1.33 \times 10^4$) and $\psi = 60°$.

the elements of the tip vortices — a key feature in rotor flow — and shows how the velocity at a fixed location on the ground plane varies with time.

Figure 3.11(a) shows the slipstream axial (vertical) velocity field when $\psi = 60°$. In this figure, blue denotes downward velocities and orange/red denotes upward velocities. Because the vortices are generally convecting downward, the blue side of the vortex appears more intense than the orange (upward moving) side. Figure 3.11(b) shows the axial (vertical) velocities near the ground plane from $y/R = 1.25 - 2.5$ at a non-dimensional axial height of $z/R = 0.1$. As before, the vortex centers were located using the Q-criterion and Γ-method, and both results are overlaid on the plot.

Notice that to the right of each vortex, a region of positive axial velocity is present. On a sediment bed, this upward velocity would act to lift any mobilized particles away from the ground. To the left of each vortex core, a region of negative axial velocity is present. If there are particles in the fluid on this side of the vortex then they would be accelerated downwards toward the sediment bed, and may bombard the bed.

3.5 Instantaneous PIV

While phase-averaging of the PIV measurements gives one measure of the tip vortex strengths, the instantaneous flow field measurements capture the unsteady flow conditions found in the rotor wake. Figure 3.12(a) shows the instantaneous radial velocities in the flow field with the rotor at 100 rpm ($Re_{\text{tip}} = 1.33 \times 10^4$) and at a blade azimuthal position of $\psi = 10°$. While the vortices are rendered here as red/blue pairs, they were not as sharp as was found in the phase-averaged data shown in Fig. 3.8(a). Contours of $\Gamma = 0.6$ are shown in white to highlight the vortex locations.

Figure 3.12(b) shows four of the 150 instantaneous velocity profiles used to compute the phase-averaged results (also shown here for comparison) at $y/R = 1.7$. While all of the profiles are qualitatively similar to the phase-averaged results, there are large fluctuations in the instantaneous flow measurements. Note that some flow velocities near the wall are greater than the phase-averaged values, some are smaller, and some are even negative (i.e., reverse flow). In all of the observed velocity profiles, the instantaneous measurements showed higher velocity maximums than the phase-averaged cases.

3.6 Dual-Phase Flow Visualization

To better understand how the specific flow structures below a hovering rotor may influence the problem of rotorcraft brownout, dual-phase flow visualization was conducted. This approach showed how (and when) sediment mobilization and uplift occurred by the action of the rotor wake. The objective of these experiments was to determine if sediment mobilization and entrainment into the flow correlates to the transit of a vortex element over the ground, an event that was previously shown to cause higher velocity excursions.

Two different types of sediment particles were used in the current research.

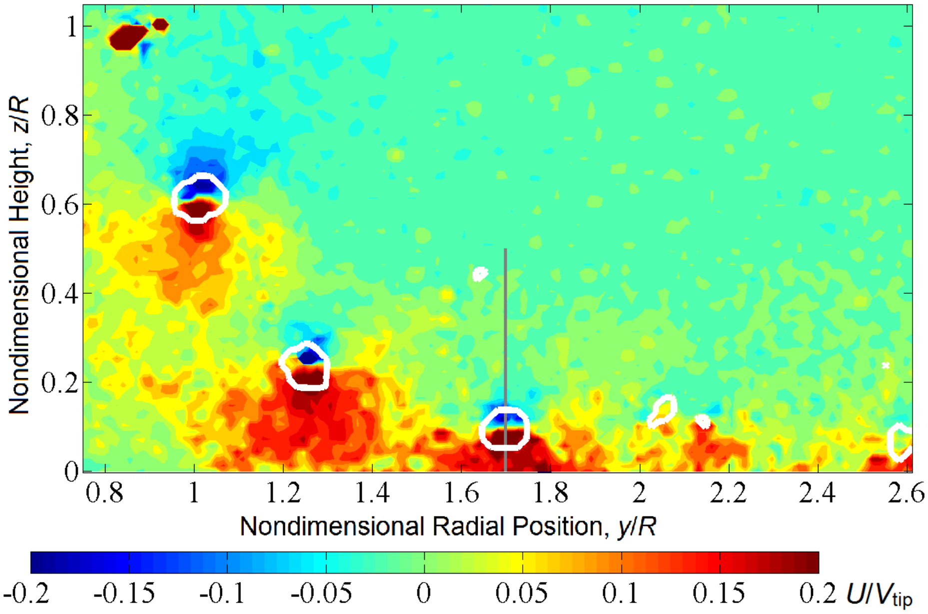

(a) An example radial velocity field

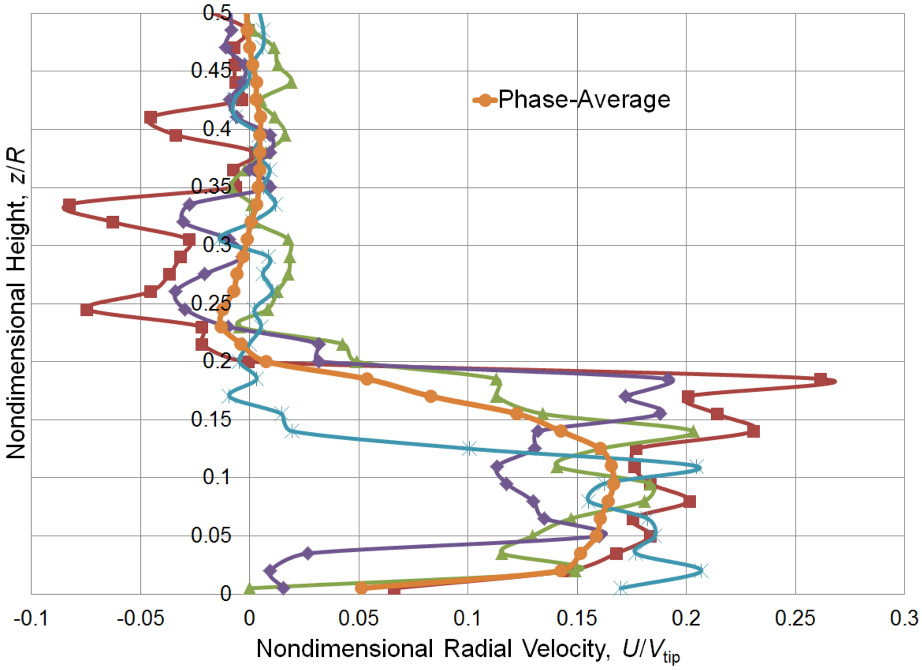

(b) Radial velocity profiles for $\psi = 10^\circ$ at $y/R = 1.7$

Figure 3.12: Instantaneous radial flow velocities with the rotor operating at 100 rpm ($Re_{\text{tip}} = 1.33 \times 10^4$) and $\psi = 10^\circ$.

Soda-glass microspheres of diameters between 45–63 μm and of a density 2,575 kg m^{-3} were used to match the particles used in previous research [29]. In addition, stainless steel particles of diameter 44–125 μm and a density of 7,473 kg m^{-3} were also used.

3.6.1 Soda-Glass Particles

Figure 3.13 shows an image of the two-phase flow in ROI 2, with the rotor operating at 100 rpm ($Re_{\text{tip}} = 1.33 \times 10^4$) one rotor radius above a sediment bed comprised of the 45–63 μm soda-glass microspheres. The flow is from left-to-right, and the approximate locations of the tip vortices have been marked with spirals. In Fig. 3.13, a dense concentration of uplifted particles can be seen in front of and below passing vortices (see Fig. 3.13, Region (a)). Notice that particles are not uniformly uplifted by the rotor wake, but appear to respond to the local excursions in flow velocity (and resulting shear stress). This condition corresponds to the phase-averaged PIV measurements (presented in Section 3.4) in which there was a region of larger-than-average positive radial (see Fig. 3.8) and axial velocities (see Fig. 3.12) in front of the tip vortices. Between the vortices there is a region of relatively quiescent flow (see Fig. 3.13 (b)) with relatively few suspended particles. The flow shown here did not uplift sediment into Region (c) of Fig. 3.13, only achieving a maximum height of approximately $z/R = 0.5$.

The rotor speed (and thus the tip speed of the rotor) was then increased to 120 rpm ($Re_{\text{tip}} = 1.60 \times 10^4$), increasing the swirl velocities in the tip vortex, and the velocity of the rotor downwash (through the effects of increasing thrust, see

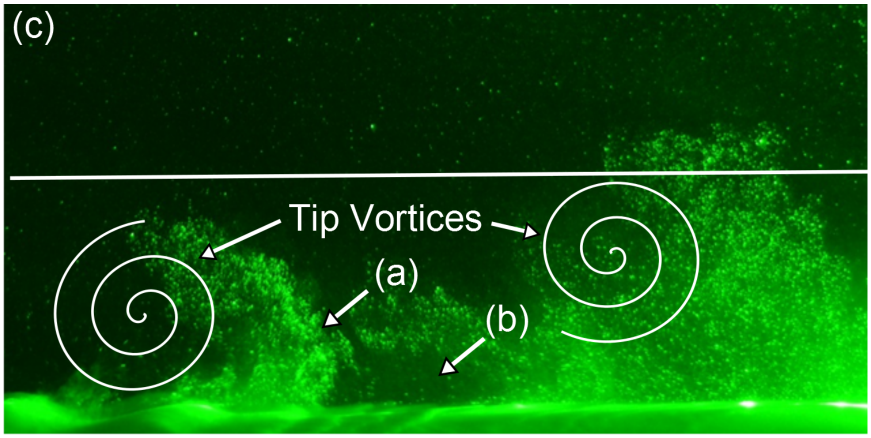

Figure 3.13: Dual-phase flow visualization in ROI 2 with the rotor operating at 100 rpm ($Re_{\text{tip}} = 1.33 \times 10^4$) showing sediment mobilization. (a) Quiescent area between vortices (b) Wave of mobilized particles caused by vortex passage (c) Region above vortices

Section 2.4). Figure 3.14 shows a greater quantity of suspended sediment was uplifted to greater heights, and a significantly larger concentration of sediment was produced.

The relative quantity of suspended sediment was compared at the different rotor operating conditions by measuring the percentage of each image covered by sediment particles (see Section 2.5.3). In Fig. 3.13 (at 100 rpm, $Re_{\text{tip}} = 1.33 \times 10^4$), 2.70% of the image was obscured by suspended sediment particles, while in Fig. 3.14 at (120 rpm, $Re_{\text{tip}} = 1.60 \times 10^4$), 8.12% of the image was obscured by sediment. In addition to more particles being mobilized and entrained in the flow, the sediment was also more evenly distributed at the higher rotor rpm, and more particles appeared in the flow above and behind the vortices. Approximately fifty times more particles were measured in Region (c) of Fig. 3.14 than in Region (c) of Fig. 3.13.

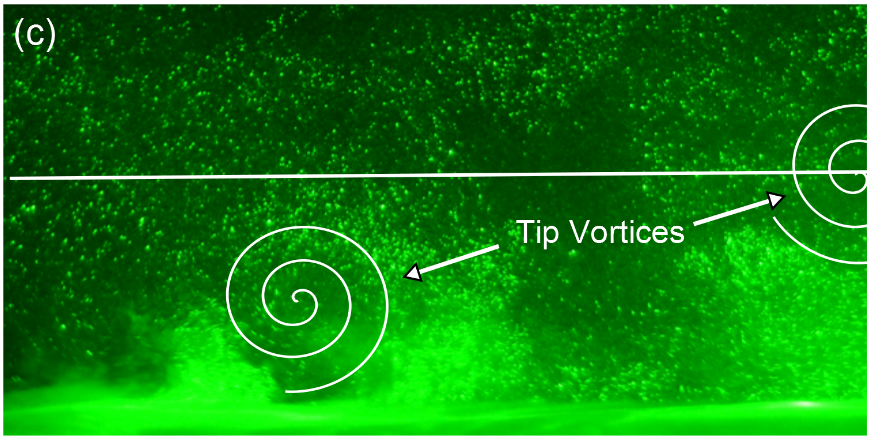

Figure 3.14: Dual-phase flow visualization in ROI 2 with the rotor operating at 120 rpm ($Re_{\text{tip}} = 1.60 \times 10^4$) showing large quantities of sediment mobilization in Region (c) above the vortices.

The increase in the groundwash velocity between the 100 and 120 rpm cases also altered the mechanisms of sediment mobilization. At 100 rpm, corresponding to a tip Reynolds number of 1.33×10^4, sediment particles were not entrained or uplifted between vortex passages. However, particle mobilization did occur between vortex passages at higher rotor rotational speeds (120 rpm). It appears that between 100 rpm and 120 rpm, a threshold condition was exceeded that caused a significant increase in particle mobilization and dispersal throughout the flow. Figure 3.15 shows that at even higher rotor rpm and flow velocities, even more sediment is uplifted, in this case creating a relatively dense sediment cloud.

Reducing the rotor tip speed to 80 rpm ($Re_{\text{tip}} = 1.06 \times 10^4$) greatly decreased the quantity of sediment that was uplifted. Figure 3.16 shows results for ROI 2 when the rotor was operating at 80 rpm. At this operating condition, the only sediment that was mobilized was just ahead of the vortex flow at the ground, where

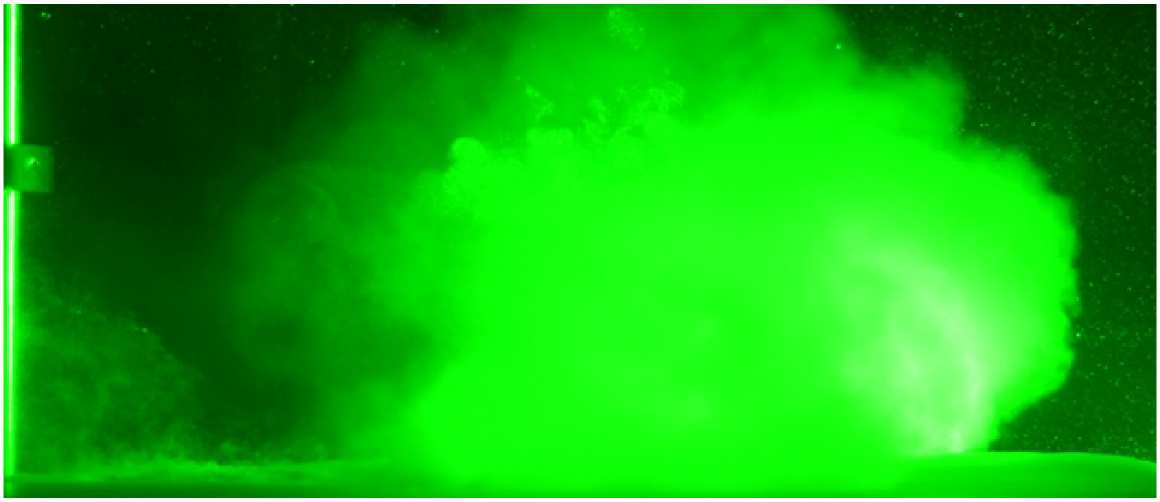

Figure 3.15: Dual-phase flow visualization with the rotor operating at 450 rpm ($Re_{\text{tip}} = 5.98 \times 10^4$).

there was an axial (upward) velocity (see Fig. 3.12) and an increased streamwise velocity along the sediment bed (see Fig. 3.8). It appears that the threshold for sediment mobilization was only met in the regions of the flow with the highest (and most unsteady) flow velocities. Furthermore, sediment was uplifted primarily by younger vortices (the ones to the left of the image); these younger vortices were to be more coherent, and so contained the higher flow velocities that were necessary for sediment mobilization.

3.6.2 Stainless Steel Particles

Further dual-phase flow visualization was performed with the rotor operating at 450 rpm, corresponding to a tip Reynolds number of 5.98×10^4, and using steel sediment particles instead of soda-glass microspheres. A significantly higher rotational speed (450 rpm) was required in this case because the other operating

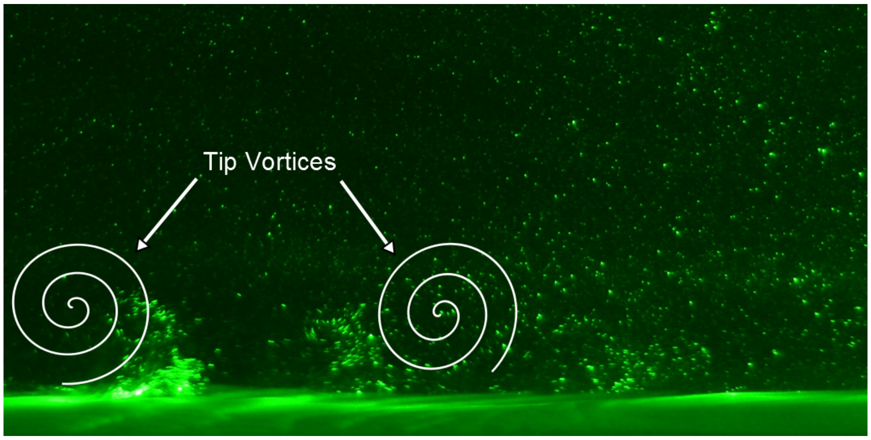

Figure 3.16: Dual-phase flow visualization in ROI 2 with the rotor operating at 80 rpm ($Re_{\text{tip}} = 1.06 \times 10^4$).

conditions (defined in Section 3.6.1) failed to mobilize the stainless steel particles. The higher specific gravity of the steel particles (leading to a higher particle terminal velocity) is the likely reason higher rotor speeds are necessary to entrain the particles. Figure 3.17 shows a flow visualization image of the stainless steel particles that were uplifted at 450 rpm. This case looks similar to the glass sediment case when the rotor operated at 120 rpm ($Re_{\text{tip}} = 1.33 \times 10^4$; see Fig. 3.13) despite the different particle densities and rotor operating conditions.

3.7 Summary

This chapter has discussed the flow structures produced by a small rotor operating in ground effect as observed using flow visualization and PIV. Flow visualization showed the behavior of the tip vortices near the ground plane, as well as turbulent zones found within the rotor flow. Time-averaged PIV allowed for the measurements of the time-history of the flow. Phase-averaged and instantaneous

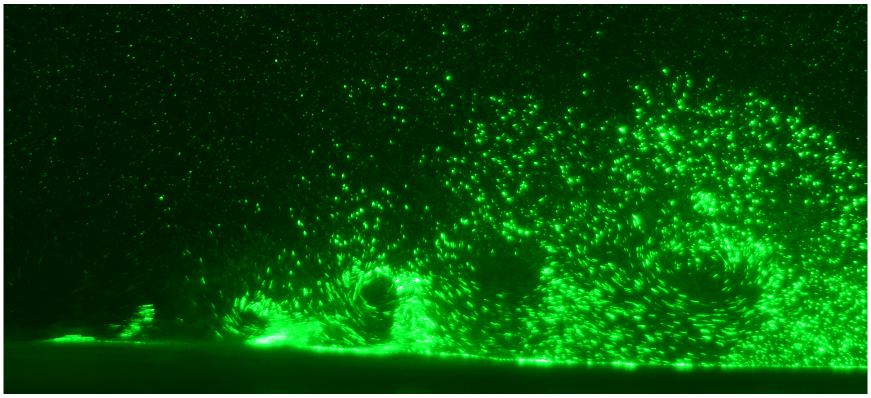

Figure 3.17: Dual-phase flow visualization of the stainless steel particles in ROI 2 with the rotor operating at 450 rpm ($Re_{\mathrm{tip}} = 5.98 \times 10^4$).

PIV was used to characterize the features of the tip vortices. The dual-phase flow visualization was used to show the effects of vortex passage on sediment mobilization and transport.

Chapter 4

Discussion

4.1 Overview

The previous chapter described the phase-averaged and time-averaged particle image velocimetry (PIV) experiments performed to study the flow beneath a rotor hovering over a ground plane. To relate the results obtained from the present work with those of other experiments performed in air [29], it was necessary to calculate the similarity parameters that relate the single-phase and dual-phase flow environments. The present chapter discuses the results that were obtained and explores a method for determining new similarity parameters and calculating their values from the measurements.

4.2 Classical Similarity Parameters

The "classical" similarity parameters (see Greeley and Iverson [38] and Appendix A) used to describe the two-phase flow in the present research were:

1. Particle diameter-to-rotor radius ratio, D_p/R
2. Particle-to-fluid density ratio, ρ_s/ρ
3. Ratio of characteristic flow velocity to particle terminal velocity, U_{char}/U_F

4. Densimetric Froude number, $U_{\text{char}}/\sqrt{((\rho_s/\rho)-1)gD_p}$
5. Threshold friction velocity ratio, U_{char}/U_t^*

As mentioned in Section 1.4, these parameters were chosen to correspond with those studied in previous experiments in air [29] which are a subset of the parameters given by Greeley and Iverson [38].

4.2.1 Time-Averaged Characteristic Velocity

Three of the classical scaling parameters listed above depend on the evaluation of a characteristic velocity, U_{char}, within the flow. In previous rotor studies, this value has been calculated from a time-average of the PIV measurements of the flow velocities at all (measured) radial positions along the sediment bed [16,29]. A similar method was used in the current work by using the time-averaged PIV results.

The time-averaged velocity field near the ground plane in the region from $y/R = 1.25$ to $y/R = 2.60$ was calculated from 500 PIV realizations taken at numerous blade azimuthal positions. The ensemble average was calculated using

$$U_{\text{avg}}(i,j) = \frac{1}{N}\sum_{n=1}^{N} U_m(i,j) \tag{4.1}$$

where N is the total number of measurements ($N = 500$ in this case), n is an individual image realization, and (i,j) represents the spatial location of a velocity measurement in a PIV realization. The characteristic velocity was then calculated by selecting the peak velocity, U, at each radial station, y/R, and then ensemble averaging the peak velocities to give an average peak flow velocity, U_{char}. This value can be written as

$$U_{\text{char}} = \frac{1}{N} \sum_{i=1}^{k} \max(U(i)) \tag{4.2}$$

where k is equal to the number of measured radial positions and $\max(U(i))$ is the peak velocity at a given radial position, y/R. Table 4.1 shows the results of this analysis for the different cases tested in the present research.

Table 4.1: Calculated (time-averaged) characteristic velocities.

Rotor Operating Condition (rpm)	Tip Reynolds Number (Re_{tip})	U_{char} (ms^{-1})
80	1.06×10^4	0.076
100	1.33×10^4	0.095
120	1.60×10^4	0.120
152	2.02×10^4	0.186
450	5.98×10^4	0.445

The rotor rig used in the present work was thrust-matched at 152 rpm to the rotor used in Baharani's research. Direct thrust measurements could not be obtained with the present experimental set-up. However, a comparison of the rotor thrust between the two rotor rigs can be made by using momentum theory as a basis, beginning with the thrust equation, i.e.

$$T = \dot{m}w = \dot{m}(2v_i) = 2(\rho A v_i)v_i = 2\rho A v_i^2 \tag{4.3}$$

where T is the thrust of the rotor, $\dot{m}$ the mass flow through the rotor disk, w is the rotor-induced velocity in the far wake, ρ is the density of the working fluid, A

is the disk area of the rotor, and v_i is the hover-induced velocity of the rotor at the rotor plane. By setting the thrust of the two rotor systems to be equal for the two different fluid mediums, the difference in the induced velocity can be found using Eq. 4.3, resulting in

$$2\rho_{\text{air}} A v_{i\ \text{air}}^2 = 2\rho_{\text{water}} A v_{i\ \text{water}}^2 \tag{4.4}$$

Because the disk (and blade) areas of the two rotor systems are equal, this result simplifies to

$$\rho_{\text{air}} v_{i\ \text{air}}^2 = \rho_{\text{water}} v_{i\ \text{water}}^2 \tag{4.5}$$

Rearranging yields

$$\frac{\rho_{\text{air}}}{\rho_{\text{water}}} = \left(\frac{v_{i\ \text{water}}}{v_{i\ \text{air}}}\right)^2 \tag{4.6}$$

and solving for the induced velocity in water results in

$$v_{i\ \text{water}} = v_{i\ \text{air}} \sqrt{\frac{\rho_{\text{air}}}{\rho_{\text{water}}}} \tag{4.7}$$

In Baharani's experiments [29], a characteristic velocity of 4.10 ms^{-1} was measured. With the density of air equal to 1.20 kg m^{-3}, and the density of water equal to 998 kg m^{-3}, Eq. 4.7 (momentum theory) suggests an expected thrust-matched characteristic velocity in water of approximately 0.142 ms^{-1} with the rotor operating at 152 rpm. Table 4.1 shows that at 152 rpm, the actual measured characteristic velocity in the present experiments was 0.186 ms^{-1}.

Table 4.2: Calculated time-averaged similarity parameters.

	Geometric Parameters			Operational Parameters		
Sediment type, particle size, and rotor rpm	Size ratio	Density ratio	Characteristic flow velocity (Table 4.1)	Terminal velocity ratio	Densimetric Froude number	Threshold friction velocity ratio
	$\frac{D_p}{R}$	$\frac{\rho_s}{\rho}$	U_{char} (ms^{-1})	$\frac{U_{\text{char}}}{U_F}$	$\frac{U_{\text{char}}}{\sqrt{((\rho_s/\rho)-1)gD_p}}$	$\frac{U_{\text{char}}}{U_t^*}$
Glass microspheres, 45–63 μm, 80 rpm	6.42×10^{-4}	2.578	0.0758	33	2.69	8.28
Glass microspheres, 45–63 μm, 100 rpm	6.42×10^{-4}	2.578	0.0946	41.2	3.36	10.33
Glass microspheres, 45–63 μm, 120 rpm	6.42×10^{-4}	2.578	0.1195	52.1	4.25	13.05
Steel microspheres, 44–125 μm, 450 rpm	9.94×10^{-4}	7.474	0.4445	20.98	6.07	40.6

4.2.2 Time-Averaged Similarity Parameters

Using the time-averaged characteristic velocities given in Table 4.1, and further sediment and rotor operating characteristics, the similarity parameter values shown in Table 4.2 were computed. These parameters have been classified as either "geometric" (i.e., parameters that depend only on the geometry of the problem), or "operational" (i.e., parameters that depend on the rotor operating conditions).

The dual-phase flow visualization presented in Chapter 3 (see Figs. 3.13–3.16) showed how the rotor operating conditions (e.g., the characteristic flow velocity) affected the quantity of sediment uplift — higher rpm produced higher flow velocities, which mobilized more sediment. The geometric parameters (particle diameter-to-rotor radius ratio, D_p/R, and particle-to-fluid density ratio, ρ_s/ρ) remained constant for the tests with the glass microspheres, despite changes in rotor operating conditions. The rotor operational parameters, however, are affected by the characteristic velocity, which depends on the rotor rpm. The quantity of sediment mobilization was found to increase with increases in characteristic velocity (as shown in Section. 3.6.1).

In addition to the glass particles, stainless steel microspheres were also used as sediment. It was found that higher rotor rotational speeds (and thus higher flow velocities) were required to mobilize these particles. Even at higher operating speeds (450 rpm), the mobilization and entrainment of the stainless steel particles was less severe than for the 120 rpm case with the glass microspheres.

Table 4.2 shows that the densimetric Froude number and the threshold friction velocity ratio were higher when the rotor was operating at 450 rpm with steel particles than when the rotor was operating at 120 rpm with the glass particles. At the same time, the terminal velocity ratio decreased significantly between the two cases, reaching values lower than those measured with the glass particles with the rotor operating at 80 rpm.

Of the three operational similarity parameters listed in Table 4.2, the terminal velocity ratio best reflected the trends (increasing glass particle uplift with an increase in rotor rpm) seen in the dual-phase flow visualization. However, the trends seen in the terminal velocity ratio did not completely mirror the results seen in the flow visualization. There was more sediment uplift with the steel particles and the rotor operating at 450 rpm than with the glass particles and the rotor operating at 80 rpm, even though the steel particles have a lower terminal velocity ratio. This difference may be because the classical similarity parameters use the steady flow velocities obtained from time-averaging and do not account for the unsteady velocity fluctuations inherent in the rotor flow.

4.2.3 Phase-Averaged Similarity Parameters

Previous observations of the dual-phase flow (see Section 3.6) showed a link between the passage of tip vortices near the ground plane and bursts of increased sediment mobilization and uplift. The velocity excursions caused by vortex passages are often large enough to exceed the particle threshold friction velocity and so mobilize the particles on the bed. However, values of the classical similarity parameters presented in the previous section were computed using a time-averaged characteristic velocity, which does not account for such velocity fluctuations.

In Section 3.4, phase-averaged results were obtained by ensemble averaging the PIV images with the blade at a fixed azimuthal position, ψ. Three different PIV realizations, with the blade at $\psi = 320^\circ, 10^\circ$, and 60° were captured. Figure 4.1 shows the positions of the nearest vortex relative to the measurement location at $y/R = 1.7$ for the three PIV realizations. The maximum radial velocities measured at $y/R = 1.7$ for each of the three different phase-averaged data sets were then used as three different characteristic velocities. These velocities were used to show how the similarity parameter values changed at $y/R = 1.7$ because of the presence of a nearby vortex.

Table 4.3 shows how the time-averaged similarity parameter values measured with the rotor at 100 rpm compare to those computed using the characteristic velocities measured in the three phase-averaged PIV realizations. The geometric pa-

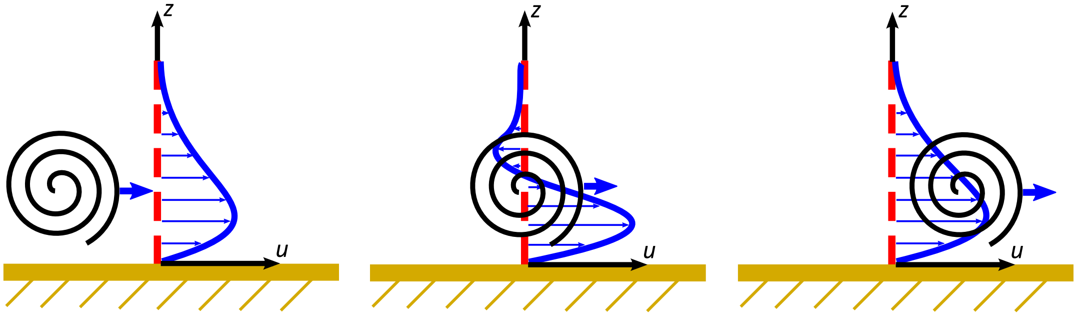

(a) $\psi = 320°$ (b) $\psi = 10°$ (c) $\psi = 60°$

Figure 4.1: Vortex location relative to a vertical cut at $y/R = 1.7$.

rameter values are constant but the operational parameters vary. Before and after the vortex passage (i.e., the $\psi = 320°$ and $\psi = 60°$ cases, respectively), the values of the phase-averaged operational similarity parameters are similar to those of the time-averaged values. However, the values of these parameters are very different at $\psi = 10°$, when the vortex core is centered over the measurement point at $y/R = 1.7$. At $\psi = 10°$, the parameter values increase more than 60% because of the increase in local flow velocity caused by the tip vortex. This effect correlates with the dual-phase flow visualization (see Figs. 3.13 – 3.16), where particle mobilization and uplift was found to occur primarily in the region below or directly ahead of a vortex. This observation shows the need for appropriate similarity parameters that account for the influence of the tip vortices in the two-phase flow.

4.2.4 Discussion of the Classical Similarity Parameters

The design of an experiment generally requires a compromise when selecting the similarity parameters that will be matched. With at least fifteen “classical”

Table 4.3: Calculated phase-averaged similarity parameters at $y/R = 1.7$.

	Geometric Parameters			Operational Parameters		
Test Case Particle size and rpm	Size ratio $\frac{D_p}{R}$	Density ratio $\frac{\rho_s}{\rho}$	Characteristic velocity U_{char} (ms^{-1})	Terminal velocity ratio $\frac{U_{\text{char}}}{U_F}$	Densimetric Froude number $\frac{U_{\text{char}}}{\sqrt{(\rho_s/\rho - 1)gD_p}}$	Threshold friction velocity ratio $\frac{U_{\text{char}}}{U_t^*}$
Time-averaged 100 rpm 45–63 μm Glass microspheres	6.42×10^{-4}	2.578	0.0946	41.2	3.36	10.33
Phase-averaged, $\boldsymbol{\psi = 320^\circ}$ 100 rpm 45–63 μm Glass microspheres	6.42×10^{-4}	2.578	0.0989	43.1	3.51	10.79
Phase-averaged, $\boldsymbol{\psi = 10^\circ}$ 100 rpm 45–63 μm Glass microspheres	6.42×10^{-4}	2.578	0.1669	72.7	5.93	18.22
Phase-averaged, $\boldsymbol{\psi = 60^\circ}$ 100 rpm 45–63 μm Glass microspheres	6.42×10^{-4}	2.578	0.1094	47.7	3.89	11.94

similarity parameters in the coupled aerodynamics/sediment transport problem [38], there are likely to be significant challenges in scaling laboratory-scale experiments. Some interdependencies between the scaling parameters also makes it difficult to simultaneously scale all of the parameters that might be relevant to the problem. Therefore, it is important to understand which scaling parameters are likely to have the greatest effect on sediment mobilization and transport.

Dual-phase flow visualization (see Section 3.6) suggested that an important factor in the operational parameters is the characteristic velocity of the fluid, U_{char}. It was found that as the characteristic velocity increased, the quantity of mobilized particles also increased. At lower flow velocities, the sediment particles only experienced saltation (or creep) along the ground plane. However, once a certain threshold velocity was exceeded, sediment particles were transported away from the ground and many particles remained suspended in the flow for a longer time.

The classical operational parameters, which assume steady flow velocities, represent sediment mobilization and entrainment for aeolian environments. However, the flow visualization results suggest that an important characteristic of the flow field induced by a rotor is the unsteady local velocities induced by the tip vortices as they convect along the sediment bed. The classical similarity parameters are based on steady flows, which do not capture these unsteady effects. This deficiency can be resolved to some extent by using the phase-averaged values of the characteristic velocities. However, new parameters that characterize the most important unsteady flow features, the effects of the blade tip vortices, better describe the brownout environment.

4.3 New Scaling Parameters

Using the Buckingham-Π Theorem, new scaling parameters were derived for use in unsteady and aperiodic rotor flows. Because of the observed importance of the tip vortices in mobilizing and entraining sediment (see Section 3.6), it was important to include the measured characteristics of the tip vortices in addition to the properties of the sediment in the formulation of the new parameters.

4.3.1 Vortex Characteristics

The first step in deriving new similarity parameters was to quantify the characteristics of the vortices produced by the rotor blades. Of greatest interest were quantities such as circulation, vortex Reynolds number, peak swirl velocity, vortex core size, and overall area of the flow that was affected by the vortices.

Circulation:

The circulation of a vortex is defined by the closed loop line integral

$$\Gamma_v = \oint_C \mathbf{V} \cdot \mathbf{ds} \tag{4.8}$$

where **V** is the local fluid velocity and **ds** is the directed line segment along the closed contour of integration, C. In the current work, the circulation was calculated by using the circulation box method. The center (i.e., the core region) of a vortex was found using methods discussed previously (see Section 2.7) and a small rectangular box oriented along the abscissa and ordinate axes enclosing the vortex was defined, as shown in Fig. 4.2. The total circulation was calculated from discrete velocity measurements using

$$\Gamma_v = \oint_C \mathbf{V} \cdot \mathbf{ds} = \sum U_T \Delta x + V_T \Delta y \tag{4.9}$$

where U_T and V_T are the horizontal and vertical velocity components of the flow tangential to the edges of the circulation box, and Δx and Δy are the respective spatial discretizations of the velocity field measurements. The area of the circulation box was increased incrementally, recalculating the total circulation at each increment. Eventually, the circulation approaches an asymptote (see Fig. 4.3). Care was taken to exclude other sources of circulation, such as near a rotor blade, at the ground plane, or near other vortices.

Using this method, the value of the tip vortex circulation for each operating

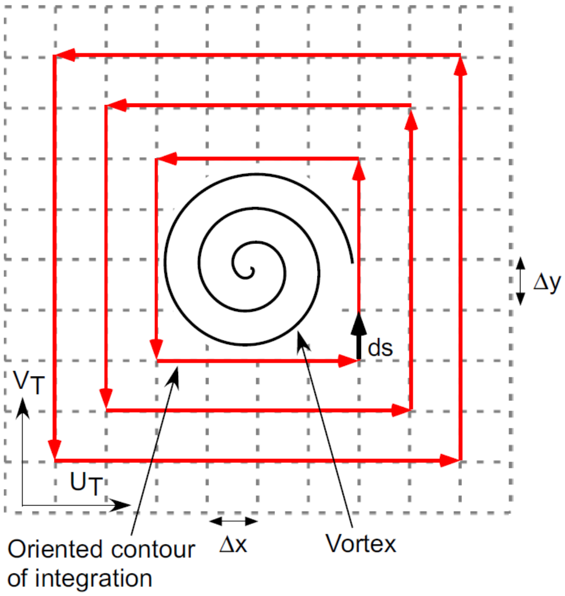

Figure 4.2: Vortex circulation calculation using the circulation box method [29].

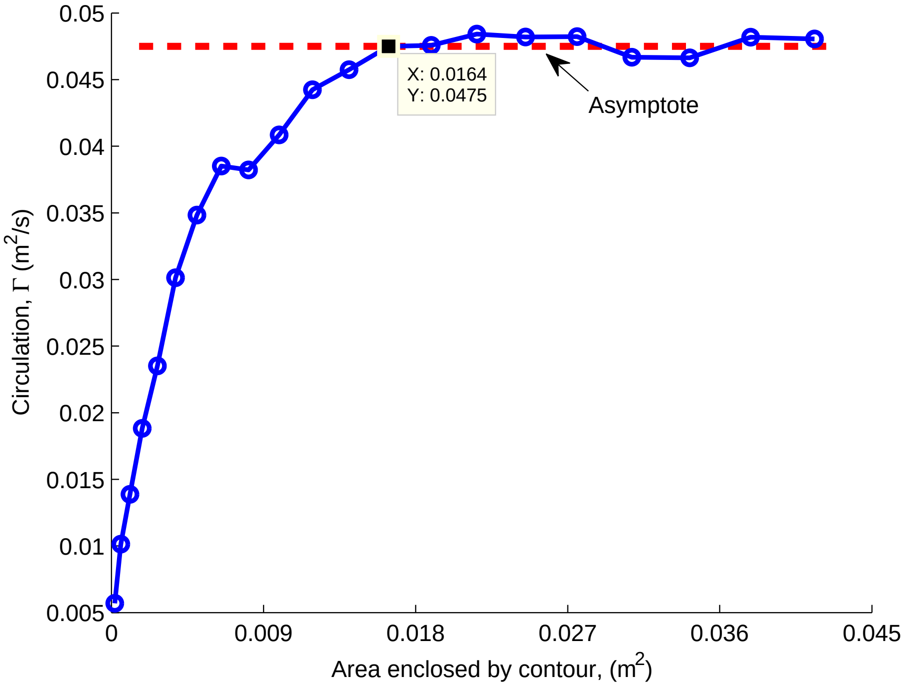

Figure 4.3: Circulation box method circulation result for 120 rpm.

condition was found from the phase-averaged PIV measurements, and is given in Table 4.4. The circulation box method requires many measurements on all sides of a vortex flow, therefore the values of circulation were calculated by using the younger vortices closer to the rotor to avoid ground interference. The values given in Table 4.4 for a full-scale helicopter are an estimate, obtained from the equation

$$\Gamma_v = 2.3 \left(\frac{C_T}{\sigma} \right) \Omega R c \tag{4.10}$$

where C_T is coefficient of thrust, σ is the solidity of the rotor, and ΩR is the tip speed of the rotor [63].

Comparing the strength of the vortices measured in this research to those obtained by Baharani [29], the vortex strength in water was less than that in air, except when the rotor was operating at 450 rpm. Notice that for all of the laboratory-scale tests, the vortices were considerably weaker than for those of a full-scale helicopter.

Vortex Reynolds number:

The vortex Reynolds number is a dimensionless number that gives a measure of the ratio of inertial forces to viscous forces in a vortex flow. The vortex Reynolds number is defined as

$$Re_v = \frac{\Gamma_v}{\nu} \tag{4.11}$$

where Γ_v is the vortex strength and ν is the coefficient of kinematic viscosity. The lower kinematic viscosity of water ($\nu_{\text{water}} = 1.00 \times 10^{-6}$) as compared to air ($\nu_{\text{air}} = 1.57 \times 10^{-5}$) and larger vortex sizes as compared to air results in higher vortex Reynolds numbers in the current work than in that of Baharani [29], but the values were still much lower than at full-scale.

Swirl velocity, core radius, and core area:

The swirl velocity is another characteristic of a vortex flow. For this research, the vortices were assumed to be axisymmetric, similar to the Rankine vortex model [64]. A vertical "cut" was taken through the vortex center, and the maximum velocity normal to this cut was taken to be the maximum swirl velocity. By selecting vortices near the rotor blade that were traveling axially (downward) through the flow and not radially (outward), the vortex convection velocity was not included in the swirl velocity estimate. All of the measured swirl velocities in the water-based experi-

Table 4.4: Calculated tip vortex characteristics.

Operating condition	Vortex radius r_c (m)	Vortex core area A_{vortex} (m^2)	Peak swirl velocity $V_{\theta\,\max}$ (ms^{-1})	Vortex strength Γ_v (m^{2}s^{-1})	Vortex Reynolds number Re_v
rpm, Re_{tip}	Laboratory-scale tests in water (calculated)				
80 rpm, 1.06×10^4	0.0225	1.59×10^{-3}	0.1618	0.0270	2.69×10^4
100 rpm, 1.33×10^4	0.0225	1.59×10^{-3}	0.1858	0.0395	3.94×10^4
120 rpm, 1.60×10^4	0.0225	1.59×10^{-3}	0.2243	0.0475	4.73×10^4
450 rpm, 5.98×10^4	0.0225	1.59×10^{-3}	0.4656	0.6067	5.98×10^5
Re_{tip}	Laboratory-scale tests in air (from [29])				
4.34×10^4	0.002	1.26×10^{-5}	10	0.241	1.54×10^4
Re_{tip}	Full-scale utility helicopter (estimated)				
7.47×10^6	0.21336	0.1430	37	37.53	2.39×10^6

ments were larger than the tests done in air, and were many times lower than those produced by a full-scale rotor.

The analysis used to find the swirl velocities also yields an estimate of the vortex core radius and vortex core area. The core radius, r_c, can be defined as the distance from the center of the vortex to the location of the maximum swirl velocity. The vortex core area was assumed to be circular and was calculated directly from the measured core radius, i.e., $A_{\text{vortex}} = \pi r_c^2$. Notice that the core radius and area of the vortices in the current work are significantly larger than for laboratory-scale vortices in air; this is a consequence of the higher dynamic viscosity of water.

To compare the results of this and previous laboratory-scale reasarch to full-scale rotor flows, the vortex characteristics for a full-scale helicopter were also needed. Leese and Knight's research on helicopter downwash [63] provided the necessary values for a common medium-lift utility helicopter, but it should be noted that these values are only approximate.

4.3.2 Buckingham-Π Theorem

The Buckingham-Π dimensional analysis is one formal method to systematically determine the dimensionless parameters governing a given problem. This approach provides a large pool of possible similarity parameters, but the final selection of the most useful parameters requires experience and judgment. To use the Buckingham-Π Theorem, a list of dependant variables was first created (given in Table 4.5). These variables were selected to represent the particle characteristics, flow velocities, and vortex characteristics known to affect sediment mobilization and entrainment. The corresponding basic units of these variables (length, mass, and time) were isolated. For example, the characteristic velocity, U_{char}, is a variable that is dependent on the flow and has units of length L and time T (LT^{-1}). Letting r be the number of basic dimensions in the problem ($r = 3$ for this case), and k be the number of dependent variables ($k = 17$), there exist $k - r$ non-dimensional Π-products (i.e., 14 potential similarity parameters).

Next, r linearly independent variables were selected from the list (Table 4.5). These initial variables appear in each new similarity parameter. Each selected variable must have a different make-up of basic units than the others selected. For example, two variables both involving velocities (LT^{-1}) cannot be selected. Additionally, across all r variables, each basic unit must be included at least once. To find new similarity parameters for the brownout problem, the Buckingham-Π analysis was performed several times with different choices of initial variables, resulting in several potential similarity parameters.

Buckingham-Π example

The initial variables were chosen to be $V_{\theta\ \max}$, ρ_s, and D_p. One more "repeating" variable was selected, i.e., U_{char}. This approach gives the first Π-product (similarity parameter) as

$$\Pi_i = U_{\text{char}} (V_{\theta\max})^b (\rho_s)^c (D_p)^d \tag{4.12}$$

Because the similarity parameter must be dimensionless, the equation can be decomposed into its basic units M, L, and T

Table 4.5: Dependent variables selected for the Buckingham-Π analysis.

Variable	Symbol	Units	Basic units
Rotor radius	R	m	L
Blade chord	c	m	L
Particle diameter	D_p	m	L
Characteristic flow velocity	U_{char}	ms^{-1}	LT^{-1}
Gravitational constant	g	ms^{-2}	LT^{-2}
Particle terminal velocity	U_F	ms^{-1}	LT^{-1}
Boundary layer thickness	L^*	m	L
Kinematic viscosity	ν	m^2s	L^2T
Threshold friction velocity	U_t^*	ms^{-1}	LT^{-1}
Sediment density	ρ_s	kg m^{-3}	ML^{-3}
Fluid density	ρ	kg m^{-3}	ML^{-3}
Blade passing frequency	t^{-1}	s^{-1}	T^{-1}
Vortex strength	Γ_v	m^2s	L^2T
Vortex core size	r_c	m	L
Maximum swirl velocity	$V_{\theta\ \text{peak}}$	ms^{-1}	LT^{-1}
Vortex area	A_{vortex}	m^2	L^2
Rotor tip speed	V_{tip}	ms^{-1}	LT^{-1}

$$M^0L^0T^0 = L^1T^{-1}(L^1T^{-1})^b(M^1L^{-3})^c(L^1)^d \tag{4.13}$$

The following r equations were then written as

$$M = 0 : 0 = 0 + 0 + c + 0$$

$$L = 0 : 0 = 1 + b - 3c + d$$

$$T = 0 : 0 = -1 - b + 0 + 0$$

Solving the r equations for b, c, and d, and substituting back into Eq. 4.12 yielded the first Π-product, i.e.,

$$\Pi_1 = \frac{U_{\text{char}}}{V_{\theta\text{max}}} \tag{4.14}$$

This type of analysis was performed again by replacing the repeating variable (U_{char} in this example) with another repeating variable. For the selected parameters in Table 4.5, this process yielded thirteen more Π-products.

Buckingham-Π Results

More Π-products were found by selecting different initial variables. Table 4.6 shows all (20) of the Π-products generated by the Buckingham-Π analyses. The first four similarity parameters in the first row of Table 4.6 belong to the list of classical parameters given by Greeley and Iverson [38]. The remaining parameters are new, and in this case account for various characteristics of the vortices, including their circulation and peak swirl velocity. Note that similarity parameters that include vortex characteristics have not been previously used to characterize aspects of the brownout problem.

Table 4.6: Similarity parameters obtained from the Buckingham-Π analyses.

$\frac{U_{\text{char}}}{U_F}$	$\frac{\rho_s}{\rho}$	$\frac{R}{D_p}$	$\frac{U_{\text{char}}}{U_t^*}$	$\frac{U_t^*}{U_F}$
$\frac{\Gamma_v}{RV_{\text{tip}}}$	$\frac{r_c}{D_p}$	$\frac{V_{\theta \ \max}^2}{U_F U_t^*}$	$\frac{\Gamma_v}{A_{\text{vortex}} t}$	$\frac{V_{\theta \ \max}}{V_{\text{tip}}}$
$\frac{V_{\theta \ \max}}{U_F}$	$\frac{\Gamma_v}{r_c U_F}$	$\frac{\Gamma_v}{R U_F}$	$\frac{\Gamma_v}{D_p U_F}$	$\frac{V_{\text{tip}}}{U_F}$
$\frac{V_{\theta \ \max}}{U_t^*}$	$\frac{\Gamma_v}{r_c U_t^*}$	$\frac{\Gamma_v}{R U_t^*}$	$\frac{\Gamma_v}{D_p U_t^*}$	$\frac{V_{\text{tip}}}{U_t^*}$

4.3.3 New Similarity Parameters

Tables 4.7 – 4.10 show representative values of these similarity parameters for different operating conditions, and at both laboratory-scale and full-scale. An initial investigation of these similarity parameters as potential indicators of brownout allowed several of them to be immediately discarded. It was clear from dual-phase flow visualization (see Section 3.6) that an increase in rotor speed resulted in the uplift of more sediment. Therefore, the similarity parameters that do not change with rotor speed or do not take vortex characteristics into account, i.e., U_{char}/U_F, Γ_v/RV_{tip}, and r_c/D_p, do not show much promise in having important consequences on the problem of brownout. These parameters were, therefore, excluded from further consideration. Furthermore, several of the parameters such as Γ_v/RU_F and

Γ_v/D_pU_F, are similar in value except for a geometric constant (i.e., R and D_p), and thus only one of each set was retained. It is important to note that these parameters are not identical (the flow could be dependent on R but not D_p) and the discarded similarity parameters may have other uses despite their exclusion in the current research. The field of prospective similarity parameters was thus narrowed to five:

1. $\Gamma_v/D_pU_t^*$, which is called the stationary inertia ratio
2. Γ_v/D_pU_F, which is called the mobile inertia ratio
3. $V_{\theta\ \max}/U_F$, which is called the terminal-swirl velocity ratio
4. $V_{\theta\ \max}/U_t^*$, which is called the threshold-swirl velocity ratio
5. $V_{\theta\ \max}^2/U_FU_t^*$, which is called the terminal/threshold-swirl velocity ratio

Stationary inertia ratio, $\Gamma_v/D_pU_t^*$

The stationary inertia ratio has a form similar to the densimetric Froude number (i.e., $U_{\text{char}}/D_p\sqrt{((\rho_s/\rho)-1)g}$). The Froude number can be thought of as a ratio of a particle's inertia to the momentum of the fluid. Similarly, the stationary inertia ratio compares a measure of the threshold velocity (related to the sediment's inertia) to the momentum of the passing fluid. Intuitively, this parameter relates how difficult it is to mobilize sediment to how much energy the flow has to initiate particle motion. The classical similarity parameter that is usually used to define the onset of particle motion is the threshold velocity ratio, U_{char}/U_t^*. As previously discussed, using the characteristic velocity alone may give a poor representation of real (unsteady)

Table 4.7: Calculated values of the new similarity parameters (1 of 4).

Operating condition	$\frac{U_t^*}{U_F}$	$\frac{\Gamma_v}{RV_{\text{tip}}}$	$\frac{r_c}{D_p}$	$\frac{V_{\theta\ \max}}{U_F}$
rpm, Re_{tip}, and sediment	Laboratory-scale tests in water (calculated)			
80 rpm, 1.06×10^4 Glass Particles	4.00	2.242	412	70.7
100 rpm, 1.33×10^4 Glass Particles	4.00	1.915	412	81.1
120 rpm, 1.60×10^4 Glass Particles	4.00	1.911	412	97.9
450 rpm, 5.98×10^4 Steel Particles	0.514	0.567	266	22.1
Re_{tip} and sediment	Laboratory-scale tests in air (from [29])			
4.34×10^4 Glass Particles	0.561	16.01	36.7	52.9
4.34×10^4 Kaolinite	117	16.01	1340	72700
4.34×10^4 Ottawa Test Dust	0.0829	16.01	5.56	3.00
Re_{tip} and sediment	Full-scale utility helicopter (estimated)			
7.47×10^6 AZTD (0-10 μm)	28.9	48.14	60100	38900

Table 4.8: Calculated values of the new similarity parameters (2 of 4).

Operating condition	$\frac{\Gamma_v}{r_c U_F}$	$\frac{\Gamma_v}{R U_F}$	$\frac{\Gamma_v}{D_p U_F}$	$\frac{V_{\text{tip}}}{U_F}$
rpm, Re_{tip}, and sediment	Laboratory-scale tests in water (calculated)			
80 rpm, 1.06×10^4 Glass Particles	524	139	$2.16{\times}10^5$	311
100 rpm, 1.33×10^4 Glass Particles	767	203	$3.16{\times}10^5$	389
120 rpm, 1.60×10^4 Glass Particles	922	244	$3.80{\times}10^5$	466
450 rpm, 5.98×10^4 Steel Particles	1260	333	$3.35{\times}10^5$	189
Re_{tip} and sediment	Laboratory-scale tests in air (from [29])			
4.34×10^4 Glass Particles	638	15.0	$2.34{\times}10^4$	240
4.34×10^4 Kaolinite	876000	20600	$1.18{\times}10^9$	$3.29{\times}10^5$
4.34×10^4 Ottawa Test Dust	36.1	0.85	201	13.6
Re_{tip} and sediment	Full-scale utility helicopter (estimated)			
7.47×10^6 AZTD (0-10 μm)	185000	4820	$1.11{\times}10^{10}$	$2.32{\times}10^5$

Table 4.9: Calculated values of the new similarity parameters (3 of 4).

Operating condition	$\frac{V^2_{\theta\ \max}}{U_F U_t^*}$	$\frac{\Gamma_v}{A_{\text{vortex}} t}$	$\frac{V_{\text{tip}}}{V_{\theta\ \max}}$	$\frac{V_{\theta\ \max}}{U_t^*}$
rpm, Re_{tip}, and sediment	Laboratory-scale tests in water (calculated)			
80 rpm, 1.06×10^4 Glass Particles	1250	12.73	4.401	17.7
100 rpm, 1.33×10^4 Glass Particles	1650	14.91	4.791	20.3
120 rpm, 1.60×10^4 Glass Particles	2400	14.94	4.762	24.5
450 rpm, 5.98×10^4 Steel Particles	935	50.30	8.603	8.60
Re_{tip} and sediment	Laboratory-scale tests in air (from [29])			
4.34×10^4 Glass Particles	4980	225.6	4.540	94.1
4.34×10^4 Kaolinite	4.51×10^7	225.6	4.540	621
4.34×10^4 Ottawa Test Dust	108	225.6	4.540	36.1
Re_{tip} and sediment	Full-scale utility helicopter (estimated)			
7.47×10^6 AZTD (0-10 μm)	5.23×10^7	61.07	5.969	1350

Table 4.10: Calculated values of the new similarity parameters (4 of 4).

Operating condition	$\frac{\Gamma_v}{r_c U_t^*}$	$\frac{\Gamma_v}{R U_t^*}$	$\frac{\Gamma_v}{D_p U_t^*}$	$\frac{V_{\text{tip}}}{U_t^*}$
rpm, Re_{tip}, and sediment	Laboratory-scale tests in water (calculated)			
80 rpm, 1.06×10^4 Glass Particles	131	34.7	5.40×10^4	77.7
100 rpm, 1.33×10^4 Glass Particles	192	50.7	7.90×10^4	97.2
120 rpm, 1.60×10^4 Glass Particles	231	61.0	9.50×10^4	117
450 rpm, 5.98×10^4 Steel Particles	2440	645	6.49×10^5	367
Re_{tip} and sediment	Laboratory-scale tests in air (from [29])			
4.34×10^4 Glass Particles	1130	26.7	4.16×10^4	428
4.34×10^4 Kaolinite	7480	176	1.00×10^7	2820
4.34×10^4 Ottawa Test Dust	434	10.2	2410	164
Re_{tip} and sediment	Full-scale utility helicopter (estimated)			
7.47×10^6 AZTD (0-10 μm)	6400	167	3.85×10^8	8030

flow conditions that exist at the sediment bed. The vortex strength on the other hand, takes into account the transient flow velocities on the ground beneath a rotor. Unfortunately, it is sometimes difficult to measure vortex strength as it requires detailed measurements of the velocity field (see Section 4.3.1).

Mobile inertia ratio, Γ_v/D_pU_F

The mobile inertia ratio differs from the stationary inertia ratio in that it uses the terminal velocity, U_t, of the sediment rather than the threshold velocity, U_t^*. This parameter characterizes the likelihood of previously uplifted particles remaining suspended in the fluid, and is a measure of the sediment's ability to be transported through the flow (and perhaps reingested into the rotor system). The stationary inertia ratio provides a measure of how difficult it is to initially mobilize sediment from the sediment bed, while the mobile inertia ratio gives a measure of how easily mobilized sediment will form a suspended dust cloud.

Terminal-swirl velocity ratio, $V_{\theta\ \mathrm{max}}/U_F$

The terminal-swirl velocity ratio relates the sediment's terminal velocity to the maximum swirl velocity ($V_{\theta\ \mathrm{max}}$) of the passing vortices. This parameter is an indicator of whether the vortices induce a high enough velocity to keep sediment suspended in the flow. It is much like the classical ratio of characteristic flow velocity to particle terminal velocity ratio, except with the key replacement of the (time-averaged) characteristic flow velocity, U_{char}, with the swirl velocity induced by the vortices.

Threshold-swirl velocity ratio, $V_{\theta\ \mathrm{max}}/U_t^*$

This similarity parameter relates the threshold velocity of the sediment to the maximum swirl velocity of the vortices. It provides insight into whether sediment will initially mobilize. This parameter is similar to the threshold friction velocity ratio (a classical similarity parameter), except with the characteristic flow velocity replaced with the swirl velocity.

Terminal/threshold-swirl velocity ratio, $V_{\theta\ \mathrm{max}}^2/U_F U_t^*$

The final similarity parameter, $V_{\theta\ \mathrm{max}}^2/U_F U_t^*$, includes both the sediment terminal velocity and threshold velocity in a single parameter. Therefore, this parameter addresses both the stationary and mobile characteristics of the sediment, and compares them to the swirl velocity of the vortex induced flow. This parameter is useful because brownout can be thought of as a two-part problem where particles must both be *mobilized* from the sediment bed and *suspended* to create a degraded visual environment.

4.3.4 Analysis of the Similarity Parameters

To evaluate the validity and impact of the newly derived similarity parameters, values of these parameters were compared against a quantitative measure of the suspended sediment. Section 2.5.3 described the process of measuring the quantity of sediment in a dual-phase flow visualization image. Table 4.11 gives the percentage of the image areas that are obscured by suspended sediment. The near ground region is the area from $y/R = 1.0$ to 3.5, and from the ground plane to a nondimensional height of $z/R = 0.5$. The upper region covers the same horizontal distance, but from $z/R = 0.5$ to 1.0. The percentage of an area obscured by sediment is plotted in Figs. 4.4 – 4.6 against the derived similarity parameters.

The first selected parameter, the mobile inertia ratio, is shown in Fig. 4.4(a). Small increases in the values of this similarity parameter at the lower end of the testing range resulted in small increases in sediment obstruction. At the highest values of the measured mobile inertia ratio (i.e., for the glass particles with the rotor operating at 450 rpm), almost complete obstruction of the flow field by sediment was recorded. Unfortunately, there is a large gap in the data between the low and high ends of the values, and while there seems to be some structure to the data, there are no clear trends discernible at this point.

A plot of the stationary inertia ratio, as shown in Fig. 4.4(b), appears qualitatively similar to the effects of the mobile inertia ratio, but with one noticeable difference. There is a point in the data with significantly higher stationary inertia ratio values, but with no increase in the quantity of uplifted sediment. This data point represents the rotor operating at 450 rpm above the stainless steel particles. While it was found to be relatively easy to mobilize the steel particles, they did not remain suspended because of their high specific gravity and higher terminal velocity. This outcome suggests that a single similarity parameter may not fully represent the brownout problem unless it can characterize both particle mobilization and suspension.

Figures 4.5(a) and 4.5(b) shows the relationships between the third and fourth parameters and suspended sediment. These parameters are related to the inertia

Table 4.11: Measured image obstruction.

Operating Condition and Sediment	Near Ground Region	Upper Region	Combined Regions
80 rpm Glass microspheres	3.21%	0.56%	1.88%
100 rpm Glass microspheres	8.05%	0.54%	4.30%
120 rpm Glass microspheres	14.78%	2.60%	8.69%
450 rpm Glass microspheres	97.57%	98.54%	98.06%
120 rpm Steel microspheres	0.038%	0.035%	0.037%
450 rpm Steel microspheres	7.86%	0.76%	4.31%

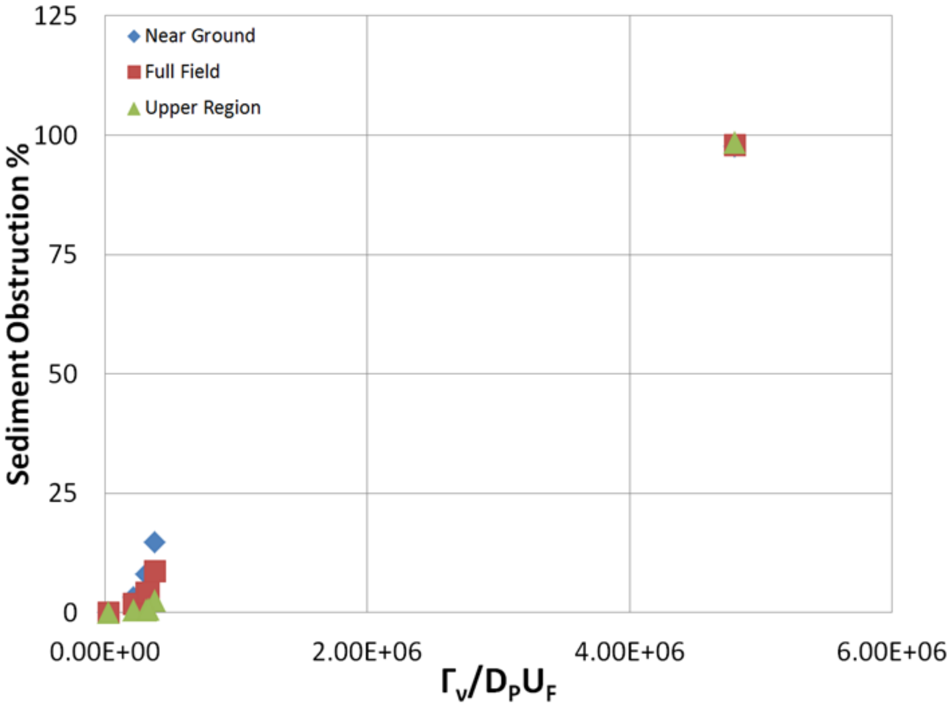

(a) Γ_v/D_pU_F Mobile inertia ratio

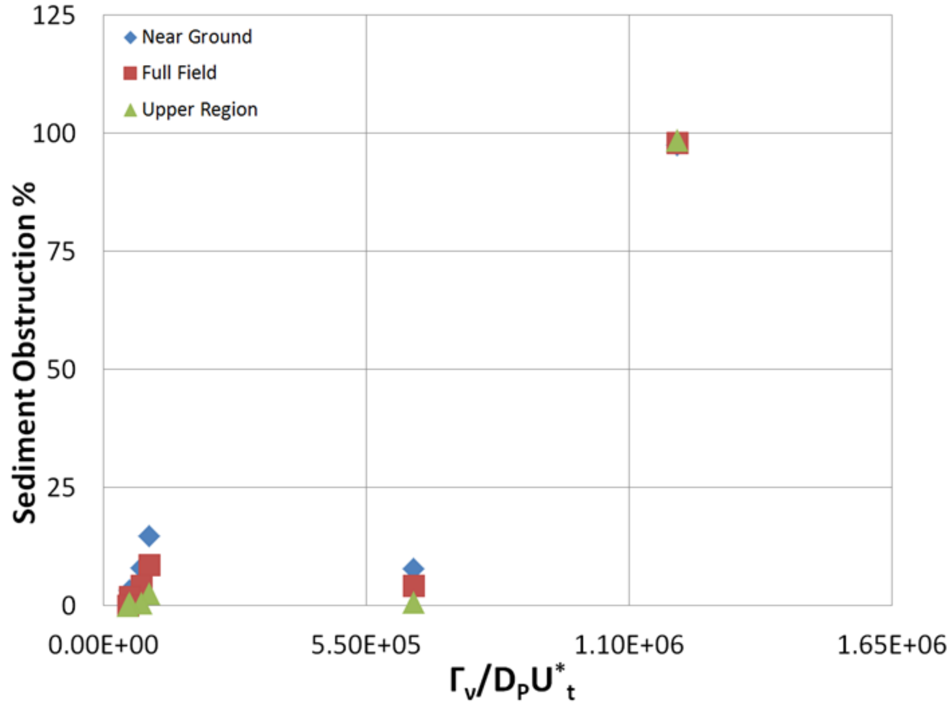

(b) $\Gamma_v/D_pU_t^*$ Stationary inertia ratio

Figure 4.4: Image obstruction as a function of inertia ratio similarity parameters.

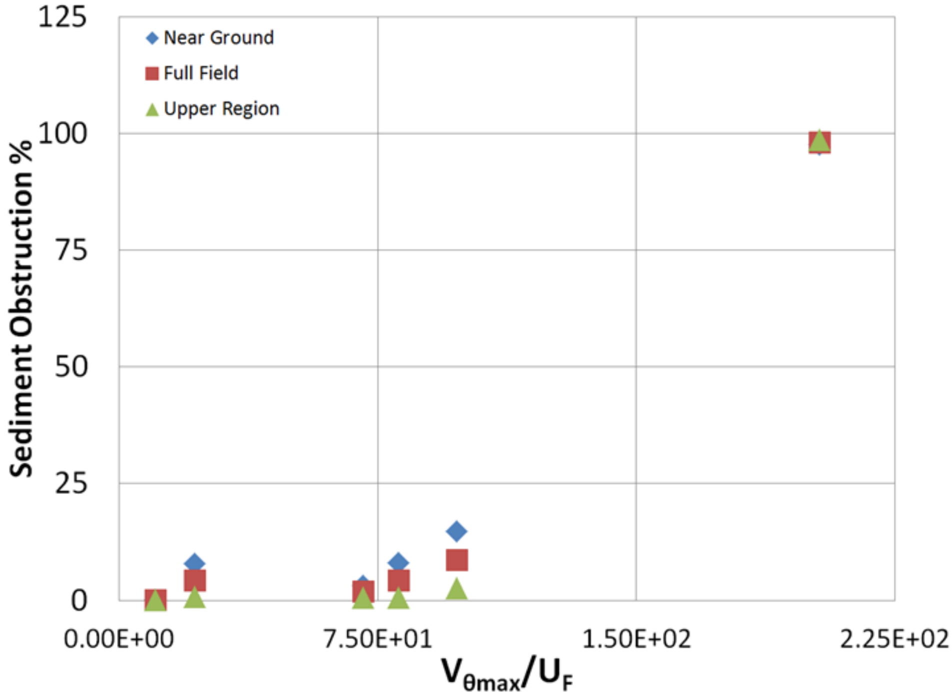

(a) $V_{\theta\ \max}/U_F$ Terminal-swirl velocity ratio

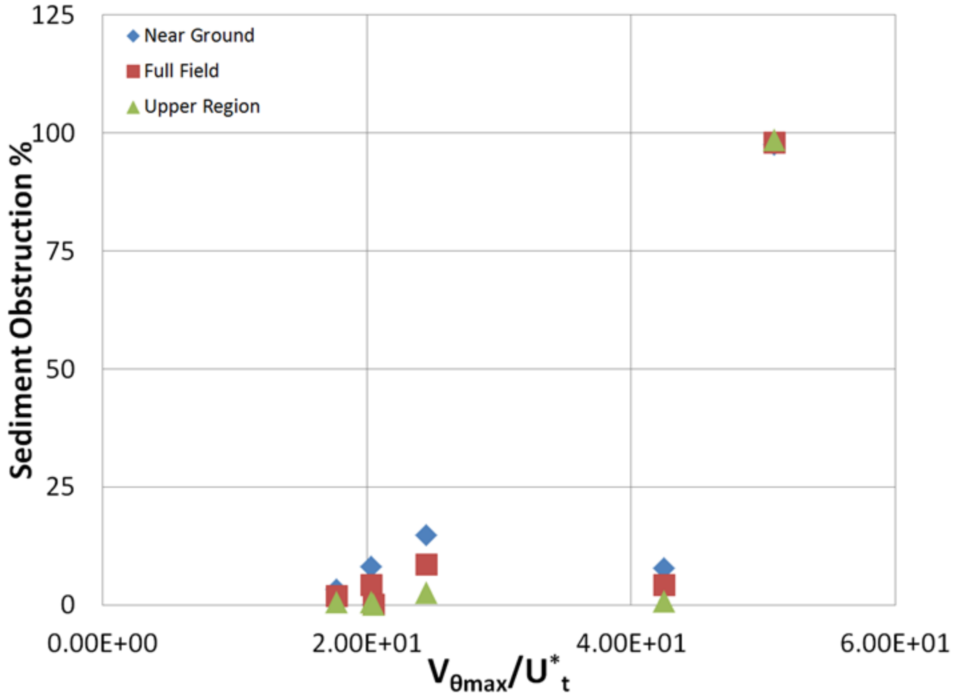

(b) $V_{\theta\ \max}/U_t^*$ Threshold-swirl velocity ratio

Figure 4.5: Image obstruction as a function of velocity ratio similarity parameters.

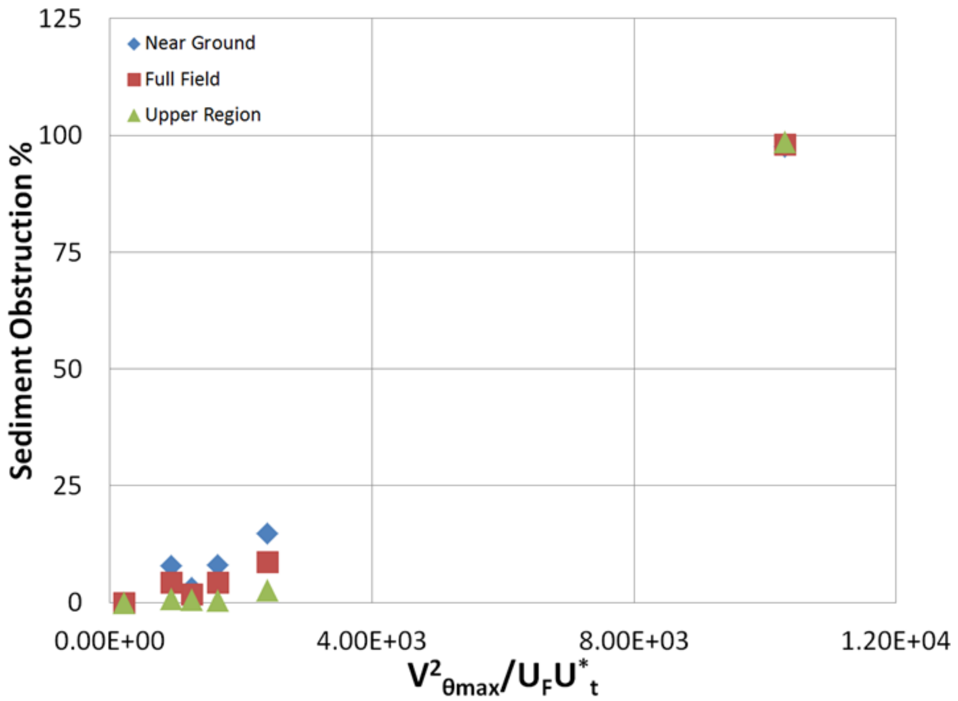

Figure 4.6: Image obstruction as a function of $V_{\theta}^{2}{}_{\max}/U_F U_t^*$, the terminal/threshold-swirl velocity similarity parameter.

ratios, but use the maximum swirl velocity induced by the vortex instead of vortex strength. This substitution spreads the data out along the abscissa.

The relationship between the final parameter and suspended sediment, shown in Fig. 4.6, is perhaps the most promising because it incorporates both sediment mobilization effects (i.e., the sediment friction threshold velocity, U_t^*) and suspension (i.e., the sediment terminal velocity, U_F). Including both characteristics in a single parameter allows for a more thorough characterization of both parts of the sediment transport problem, i.e., particle mobilization and suspension. While it can be seen that sediment obstruction increases with increases in all of the new parameter values, the data measured in the present work is only sufficient to provide some initial trends.

Further experiments are required to produce the extent of data needed to determine the sensitivities to the derived similarity parameters.

4.4 Summary

The present chapter has discussed how the similarity parameters relevant to the problem of brownout have been evaluated. The values of the similarity parameters used in aeolian two-phase sediment transport problems were measured below the rotor using time-averaged PIV. Phase-averaged PIV showed how the local velocities fluctuate as a vortex passes over a point on the ground. The vortex characteristics, such as core radius, vortex strength, and peak swirl velocities were calculated for the rotor as it operated over the ground plane. A Buckingham-Π dimensional analysis was used to develop new similarity parameters that may better account for the flow characteristics produced by these vortices. Based on these results, five new similarity parameters were selected and were plotted against quantitative measurements of sediment suspension (from the dual-phase flow visualization). Some parameters, especially the terminal/threshold-swirl velocity similarity parameter, $V_{\theta\,\max}^2/U_F U_t^*$, reflected the trends seen in the dual-phase flow visualization, with increasing values corresponding to increased quantities of sediment suspension.

Chapter 5

Conclusions

5.1 Overview

A laboratory-scale rotor, hovering in water over a mobile sediment bed, was tested to study the two-phase flow physics that could potentially influence the physics of the rotorcraft brownout problem. The rotor used in the present experiments was designed to match the physical geometry of a rotor previously tested in air [29]. Testing the rotor in water allowed for significant changes in the values of several of the scaling parameters that govern the fluid mechanics and particle transport physics of the problem.

The flow visualization experiments that were conducted showed the relatively complex nature of rotor flow in ground effect operation, and provided some results that helped to explain the mobilization of sediment by features of the rotor wake. Particle image velocimetry (PIV) techniques were used to provide measurements of the flow velocities in the rotor wake and also near the ground plane as the wake impinged upon the ground and spread outward. These measurements allowed for the values of the relevant similarity parameters to be calculated over a range of rotor operating conditions and for two different types of sediment.

A limitation in the use of classical similarity parameters for two-phase flow was found to be their inability to account for unsteady effects that are present in the rotor wake flow and the local flow at the ground plane. For example, a tip vortex that trails from a blade and subsequently interacts with the sediment bed produces unsteady flow fluctuations each time an element of the vortex passes over a point on the ground. A Buckingham-Π analysis was performed by introducing certain properties of the tip vortices in an effort to develop new similarity parameters that more completely describe the two-phase fluid flow problem.

5.2 Specific Conclusions

The outcomes from this research has lead to several conclusions:

1. The set of "classical" similarity parameters (e.g., those developed by Bagnold [37], Greeley and Iverson [38], etc.) are not fully adequate to describe sediment mobilization and entrainment by the action of a rotor wake. These classical parameters are based on steady flow assumptions, and so do not adequately represent the effects produced by the more unsteady flow conditions found beneath a rotor in ground effect operation. The classical similarity parameters use time-averaged quantities in their calculation; in particular they use a characteristic velocity, U_{char}. The dual-phase flow visualization experiments revealed that sediment mobilization is initiated and sustained primarily by the unsteady velocity fluctuations and excursions from the mean flow that are caused by the passage of the tip vortices near to the sediment bed.

2. The relevant similarity parameters governing the problem were classified as either "geometric" or "operational." Some similarity parameters, namely the

particle size-to-rotor radius ratio, D_P/R, and particle-to-fluid density ratio, ρ_s/ρ, remain constant for a given rotor system and for a given fluid. These parameters, along with any others that are independent of operational conditions, were classified as geometric parameters. Parameters that include terms that depend on the flow field (e.g., the characteristic flow velocity) were classified as operational similarity parameters.

3. To characterize and scale the rotorcraft brownout problem, it was shown why the similarity parameters should include certain characteristics of the tip vortices. To this end, a Buckingham-Π analysis was performed to identify nondimensional parameters that account for the strength, Γ_v, and/or the maximum internal (swirl) velocities, $V_{\theta\ \mathrm{max}}$, of the trailed tip vortices. Five new similarity parameters were selected, namely

   (a) The mobile inertia ratio, $\Gamma_v/D_p U_F$

   (b) The stationary inertia ratio, $\Gamma_v/D_p U_t^*$

   (c) The terminal-swirl velocity ratio, $V_{\theta\ \mathrm{max}}/U_F$

   (d) The threshold-swirl velocity ratio, $V_{\theta\ \mathrm{max}}/U_t^*$

   (e) The terminal/threshold-swirl velocity ratio, $V_{\theta\ \mathrm{max}}^2/U_F U_t^*$

   where D_P is the diameter of the particle, U_F is the terminal velocity of the sediment particles, and U_t^* is the threshold friction velocity of the particles.

4. The approximate quantity of sediment particles that were mobilized and entrained at different operating conditions was measured using dual-phase flow

visualization. The results were analyzed to examine the sensitivities (if any) to the values of the proposed new similarity parameters. Generally, increasing the values of the parameters was found to correspond to increased quantities of sediment mobilization and suspension. Of the five parameters, the terminal/threshold-swirl velocity ratio, $V_{\theta\,\max}^2/U_F U_t^*$, showed promise in helping to scale the brownout problem. This latter parameter characterizes both sediment mobilization and suspension by including both the threshold and terminal velocities of the sediment particles, as well as a characteristic flow velocity produced by the vortices.

5.3 Suggestions for Future Work

5.3.1 Further PIV Measurements

The dual-phase flow visualization showed that tip vortices play a key role in sediment mobilization and transport below a rotor. Significant differences were found when comparing the similarity parameters that were evaluated by using the time-averaged PIV measurements to those evaluated from the phase-averaged PIV results. Phase-averaging algorithms exist that can track and overlay the vortex centers (cores) to correct the slight aperiodicity and spatial locations of the vortices between successive PIV images, which may further improve the accuracy of the measurements.

Another technique that could increase understanding of the brownout phenomenon is dual-phase PIV. Dual-phase PIV allows for simultaneous, quantitative measurements of the carrier-phase velocity field (in this case water), as well as the locations and trajectories of suspended sediment particles [65]. This approach provides for a quantification of sediment mobilization and suspension. Furthermore, the flow field measurements during the dual-phase testing could also provide information about whether the suspended sediment influences the velocity field of the carrier-phase. By comparing the carrier-phase flow field velocities in a dual-phase test with single-phase PIV at the same operating conditions, it might be possible to determine how much sediment must be uplifted for the sediment to significantly influence the carrier flow.

5.3.2 Expanding the Range of the Similarity Parameters

By varying the operating conditions of the rotor or by selecting different sediment types (e.g., size and density), the sensitivity of sediment transport to changes in the values of the similarity parameters can be further explored.

Glass Sediment Particles

In the current work, the soda-glass microspheres produced a dense cloud when the rotor was operated at 450 rpm, but relatively few particles were mobilized and entrained when the rotor was at 80 rpm. More experiments at different operating conditions (that were not tested in the present research) would help to further define the relationships between sediment mobilization/suspension and the values of the similarity parameters. Table 5.1 shows examples of four test conditions that would help to better identify possible sensitivities to the values of the mobile inertia ratio.

The recommended rotor operating conditions given here are approximations based on the phase-averaged PIV results.

Table 5.1: Recommended operating conditions for further laboratory-scale testing in water.

Recommended Similarity Parameter Value (Mobile Inertia Ratio, $\frac{\Gamma_v}{D_p U_F}$)	Rotor rpm (Glass Sediment)	Rotor rpm (Steel Sediment)
7.50×10^5	165	580
1.50×10^6	240	840
2.50×10^6	320	1110
3.50×10^6	380	1340

Steel Sediment Particles

Another option for further work is to use the denser steel particles instead of (or in addition to) glass particles. While steel particles were used in the current research, only a limited set of operating conditions was tested when using those particles. Table 5.1 provides suggested operating conditions to reach four mobile inertia ratios by using the steel particles. Because the mobile inertia ratio is inversely proportional to the terminal velocity (and because the stainless steel particles have a much higher terminal velocity than the glass particles), the vortex strength, and thus the rotor rpm must also be increased.

Other Sediment Particles

Another method for testing at different similarity parameter values is to change the sediment particles while maintaining a fixed rotor operating condition (and thus a fixed vortex strength, Γ_v). Table 5.2 provides examples of several sediment materials that would produce the recommended range of the similarity parameters, assuming the particles are of the same size as the glass microspheres (average $D_p = 5.46 \times 10^{-5}$) and the rotor is operating at 120 rpm. Many other materials exist that would also satisfy the needed values and ranges of the similarity parameters. A parametric study of the effects of varying the sediment type, size, and rotor operating conditions independently could also be performed.

Table 5.2: Recommended sediment choices for further laboratory-scale testing in water at 120 rpm.

Recommended Similarity Parameter Value (Mobile Inertia Ratio, $\frac{\Gamma_v}{D_p U_F}$)	Recommended Sediment	Density (ρ_s, kg m^{-3})
7.50×10^5	Magnesium	1,940
1.50×10^6	Aluminum Oxide	1,463
2.50×10^6	Quartz, Bakelite	1,276
3.50×10^6	Sand, Glass	1,196

Appendix A

Selected Similarity Parameters

Particle Diameter-to-Rotor Radius Ratio, D_p/R

The particle diameter-to-rotor radius ratio, D_p/R, describes the size of the particles found in the flow relative to the size of the rotor generating the flow. For a full-size helicopter, with approximate values of the similarity parameters as given in Table 1.2, the particle diameter-to-rotor radius ratio is 6.22×10^{-7}, compared to 6.42×10^{-4} as in the current and previous experiments [16, 29]. If a one-to-one scaling of this parameter was preserved, the experiment would require tiny particles with a diameter of 50 nm. However, particles of this size suffer from inter-particle forces that cause particle clumping, and so they will exhibit different characteristics compared to larger particles. Furthermore, resolving such tiny particles in flow visualization images or particle image tracking velocimetry would be very difficult if not impossible.

Particle-to-Fluid Density Ratio, ρ_s/ρ

The particle-to-fluid density ratio is a parameter that directly relates the density of the sediment, ρ_s, to the fluid density, ρ [66]. This parameter is essentially a measure of the specific gravity between the two media. When switching from one fluid to another, maintaining the density ratio parameter is difficult. Water is approximately one thousand times denser than air, so finding a sediment particle that preserves the full-scale value of density ratio in water at laboratory-scale is all but impossible.

Characteristic Velocity-to-Particle Terminal Velocity Ratio, U_{char}/U_F

The characteristic velocity-to-particle terminal velocity ratio is a similarity parameter that takes into account not only the size of the sediment particles, but also the density ratio of the sediment to fluid. The terminal velocity of a particle is the maximum speed that it attains while falling freely through a fluid under the influence of gravity. This settling velocity occurs when equilibrium is reached between the forces of weight, drag and buoyancy acting on the particle, i.e., when $W = F_b + D$, where W is the weight of the particle, F_b is the buoyancy force on the particle, and D is the drag force [67]. Assuming a spherical particle, the weight and buoyancy forces on the particle are

$$W = \frac{\pi}{6} D_p^3 \rho_s g \tag{A.1}$$

and

$$F_b = \frac{\pi}{6} D_p^3 \rho g \tag{A.2}$$

respectively, and the drag force on the particle at its terminal velocity is

$$D = \frac{1}{2} \rho U_f^2 C_d A \tag{A.3}$$

where C_d is the particle drag coefficient, A is the cross-sectional area of the particle, and U_f is the terminal velocity. Substituting and solving for U_f yields

$$U_f = \sqrt{\frac{((\rho_s/\rho) - 1)4gD_p}{3C_d}} \tag{A.4}$$

The terminal velocity is affected by particle size, particle shape, and the difference between the density of the particle and the fluid medium it is suspended in. The particle terminal velocity ratio is then calculated by dividing the characteristic velocity by the terminal velocity. Previous research [29] suggests that an increase in terminal velocity ratio, which can be caused by an increase in characteristic velocity (or decrease in particle terminal velocity), results in an increase in the quantity of particles being uplifted.

Densimetric Froude Number, $U_{\text{char}}/\sqrt{((\rho/\rho_s) - 1)gD_p}$

The Froude number is a dimensionless parameter representing the ratio between the inertial forces and gravitational forces [68]. It is a predictor of sediment mobility because a body with lower inertia will be easier to mobilize than one with higher inertia [29, 69]. When dealing with an object submerged in a moving fluid, the use of densimetric Froude number is preferred because it is particle specific.

Velocity Threshold Ratio, U_{char}/U_t^*

Threshold friction velocity, $U_t^* = \sqrt{\tau_w/\rho}$, is the equivalent fluid velocity at which stationary sediment particles will begin moving along the sediment bed under the action of the fluid flow. Motion of the fluid causes shear stresses along the sediment bed which, if sufficiently high, begins moving particles along with the fluid. However, determining the threshold velocity is very difficult because it is first necessary to define when the onset of particle motion has actually occurred [70]. For example, some studies [71] have argued for the threshold to be the absolute minimum velocity required for even just one sediment particle to begin to move. This strict definition requires extremely careful observation in experiments, and determining the exact velocity is difficult and not completely unambiguous. Other research [72] has suggested that perhaps a more reasonable definition of threshold velocity is when some fraction (perhaps around 25%) of the particles become mobilized and move along the ground plane. Other definitions [70] specify the threshold velocity at the point where particles regularly creep along a sediment bed and where saltation is just beginning to occur.

Further complicating the issue of determining the threshold velocity are other characteristics of the sediment and the sediment bed, including how particles are arranged next to each other [73] or the compactness of the bed, which can prevent particle motion until higher fluid velocities are reached. In Fig. A.1, point (A) represents sediment particles that are stacked on top of each other such that the

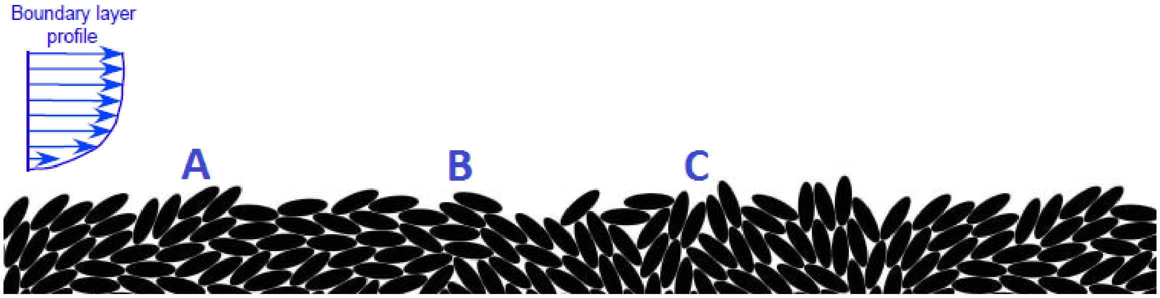

Figure A.1: Particle packing effects on motion threshold.

flow will be less likely to uplift them. Like scales on a fish, the particle arrangement in (A) allows fluid to flow over smoothly, creating a higher than expected friction threshold velocity, and so reducing the velocity threshold ratio. The arrangement of the sediment particles under point (B) are such that the flow would be more likely to mobilize the particles. Particles arranged as under (B) would present a lower friction threshold velocity than the particles under (A). As with the sediment under point (A), the sediment under (C) is arranged such that the flow would be less likely to mobilize the particles. The particles stacked against each other at (C) effectively lock them together, and will resist mobilization to a higher flow velocity.

Appendix B

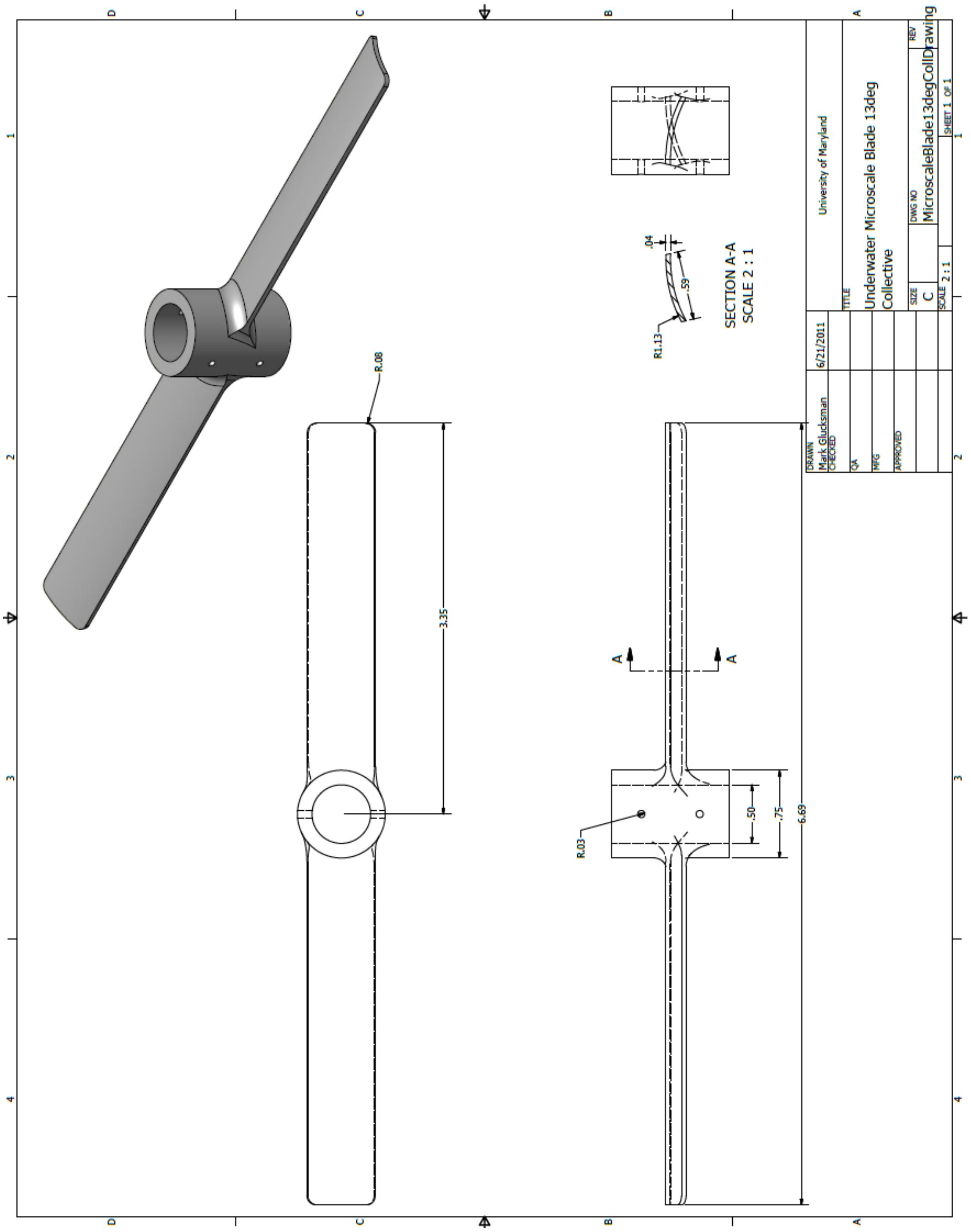
D
C
B
A
1
2
3
4
R.08
3.35
R.03
.50
.75
6.69
A
A
.04
.59
R1.13
SECTION A-A
SCALE 2 : 1
University of Maryland
TITLE
Underwater Microscale Blade 13deg Collective
DRAWN
Mark Glucksman
6/21/2011
CHECKED
QA
MFG
APPROVED
SIZE
C
DWG NO
MicroscaleBlade13degCollDrawing
REV
SCALE
2 : 1
SHEET 1 OF 1

Bibliography

[1] Mapes, P., Kent, R., and Wood, R., "DoD Helicopter Mishaps FY85-05: Findings and Recommendations," Tech. rep., U.S. Air Force, 2008.

[2] "NTSB Accident Briefs: LAX01LA283, LAX01LA304, LAX04LA285, and SEA05CA173," Tech. rep., National Transportation Safety Board, Washington, D.C.

[3] Thomas, W., Hong, S. C., Yu, C. J., and Rosenzweig, E. L., "Enhanced Erosion Protection for Rotor Blades," *Proceedings of the 65th Annual Forum of the American Helicopter Society*, Grapevine, TX, May 27–29, 2009.

[4] Tritschler, J., Celi, R., and Leishman, J. G., "A Methodology for Rotorcraft Brownout Mitigation Through Flight Path Optimization," *Proceedings of the 68th Annual Forum of the American Helicopter Society*, Phoenix, AZ, May 1–3, 2012.

[5] "Sandblaster 2 Support of See-Through Technologies for Particulate Brownout," Tech. Rep., Task 1 Technical Report, Sponsored by Defense Advanced Research Projects Agency (DOD) Strategic Technology Office, Issued by U.S. Army Aviation and Missile Command under Contract No. W31P4Q-07-C-0215, MRI Project No. 110565, October 31, 2007.

[6] "Sandblaster 2 Support of See-Through Technologies for Particulate Brownout," Tech. Rep., Task 5 Final Technical Report, Sponsored by Defense Advanced Research Projects Agency (DOD) Strategic Technology Office, Issued by U.S. Army Aviation and Missile Command under Contract No. W31P4Q-07-C-0215, MRI Project No. 110565, October 31, 2007.

[7] Harrington, W. W., Braddom, S. R., Savage, J. C., Szoboszlay, Z. P., McKinley, R. A., and Burns, H. N., "3D-LZ Brownout Landing Solution," *Proceedings of the 66th Annual Forum of the American Helicopter Society International*, Phoenix, AZ, May 11–13, 2010.

[8] Jansen, C., Wennemers, A., and Groen, E., "FlyTact: A Tactile Display Improves a Helicopter Pilots Landing Performance in Degraded Visual Environments," *Haptics: Perception, Devices and Scenarios*, Vol. 502, No. 4, 2008, pp. 867–875.

[9] Scherbarth, S., "Method of Pilot Support in Landing Helicopters in Visual Flight Under Brownout or Whiteout Conditions," 2005.

[10] Sykora, B., "BAE Systems Brownout Landing Aid System Technology (BLAST): System Overview and Flight Test Results," *Society of Photo-Optical Instrumentation Engineers (SPIE) Conference Series*, Vol. 8360, 2012, p. 19.

[11] Thomas, S., Lakshminarayan, V. K., Kalra, T. S., and Baeder, J. D., "Eulerian-Lagrangian Analysis of Cloud Evolution using CFD Coupled with a Sediment Tracking Algorithm," *Proceedings of the 67th Annual Forum of the American Helicopter Society*, Virginia Beach, VA, May 3–5, 2011.

[12] Morales, F. Naqvi, I., Squires, K. D., and Piomelli, U., "Euler-Lagrange Simulations of Particle Interactions with Coherent Vortices in Turbulent Boundary Layers," *62nd Annual Meeting of the Division of Fluid Dynamics*, Minneapolis, MN, November 2009.

[13] Bagnold, R. A., *The Physics of Blown Sand and Desert Dunes*, Dover Publications, Inc., Mineola, NY, 1941.

[14] Leishman, J.G., *Principles of Helicopter Aerodynamics*, Cambridge University Press, New York, NY, 2006.

[15] Leishman, J.G., "Challenges in Understanding the Fluid Dynamics of Brownout: Review and Update," *Proceedings of the American Helicopter Society International Meeting on Advanced Rotorcraft Technology and Safety Operations*, Omiya, Japan, November 1–3, 2010.

[16] Sydney, A., Baharani, A., and Leishman, J. G., "Understanding Brownout using Near-Wall Dual-Phase Flow Measurements," *Proceedings of the 67th Annual Forum of the American Helicopter Society*, Virginia Beach, VA, May 3–5, 2011.

[17] Beddoes, T.S., "Representation of Airfoil Behavior," *Vertica*, Vol. 7, No. 2, 1983, pp. 183–197.

[18] Cheeseman, I. C., and Bennett, W. E., "The Effect of the Ground on a Helicopter Rotor in Forward Flight," British ARC R&M 3021, 1955.

[19] Curtiss, H. C., Sun, M., Putman, W. F., and Hanker, E. J., "Rotor Aerodynamics in Ground Effect at Low Advance Ratios," *Journal of the American Helicopter Society*, Vol. 29, No. 1, 1984, pp. 48–55.

[20] Fradenburgh, E. A., "The Helicopter and the Ground Effect Machine," *Journal of the American Helicopter Society*, Vol. 5, No. 4, 1960, pp. 26–28.

[21] Hayden, J.S., "The Effect of the Ground on Helicopter Hovering Power Required," *Proceedings of the 32nd Annual National V/STOL Forum of the American Helicopter Society*, Washington D.C., May 10–12, 1976.

[22] Knight, M., and Hefner, R. A., "Analysis of Ground Effect on the Lifting Airscrew," National Advisory Committee for Aeronautics (NACA) Technical Note 835, 1941.

[23] Lakshminarayan, V. K., "Computational Investigation of Micro-Scale Coaxial Rotor Aerodynamics in Hover," Ph.D. Dissertation, Department of Aerospace Engineering, University of Maryland, College Park, 2009.

[24] Lee, T. E., Leishman, J. G., and Ramasamy, M., "Fluid Dynamics of Interacting Blade Tip Vortices With a Ground Plane," *Journal of the American Helicopter Society*, Vol. 55, No. 2, April 2010, pp. 1–16.

[25] Leishman, J. G., Bhagwat, M. J., and Bagai, A., "Free-Vortex Filament Methods for the Analysis of Helicopter Rotor Wakes," *Journal of Aircraft*, Vol. 39, No. 5, September–October, 2002, pp. 759–775.

[26] Light, J. S., and Norman, T., "Tip Vortex Geometry of a Hovering Helicopter Rotor in Ground Effect," *Proceedings of the 45th Annual Forum of the American Helicopter Society*, Boston, MA, May 22–24, 1989.

[27] Prouty, R. W., "Ground Effect and the Helicopter," *AIAA/AHS/ASEE Aircraft Design Systems and Operations Meeting*, No. AIAA Paper 85-4034, Colorado Springs, CO, October 14–16, 1985.

[28] Ramasamy, M., Johnson, B., and Leishman, J. G., "Understanding the Aerodynamic Efficiency of a Hovering Micro-Rotor," *Journal of American Helicopter Society*, Vol. 53, No. 4, October, 2008, pp. 412–428.

[29] Baharani, A., "Investigation into the Effects of Aeolian Scaling Parameters on Sediment Mobilization Below a Hovering Rotor," M.Sc. Thesis, Department of Aerospace Engineering, University of Maryland, College Park, 2011.

[30] Johnson, B., Leishman, J.G., and Sydney, A., "Investigation of Sediment Entrainment in Brownout Using High-Speed Particle Image Velocimetry," *65th Annual National Forum of the American Helicopter Society*, Grapevine, TX, May 27–29 2009.

[31] Kalra, T., Lakshminarayan, V., and Baeder, J., "CFD Validation of Micro Hovering Rotor in Ground Effect," *Proceedings of the American Helicopter Society International Specialists Conference on Aeromechanics*, San Francisco, CA, January, 2010.

[32] Milluzzo, J., Sydney, A., Rauleder, J., and Leishman, J. G., "In-Ground-Effect Aerodynamics of Rotors with Different Blade Tips," *Proceedings of the 66th Annual Forum of the American Helicopter Society*, Phoenix, AZ, May 10–13, 2010.

[33] Nathan, N. and Green, R., "Measurements of a Rotor Flow in Ground Effect and Visualization of the Brown-Out Phenomenon," *Proceedings of the 64th Annual Forum of the American Helicopter Society International*, April 29–May 1, 2008.

[34] Phillips, C., and Brown, R.E., "Eulerian Simulation of the Fluid Dynamics of Helicopter Brownout," *American Institute for Aeronautics and Astronautics Journal of Aircraft*, Vol. 46, No. 4, July 2009, pp. 1416–1429.

[35] Wachspress, D.A., Whitehouse, G.R., Keller, J.D., and Yu, H., "A High Fidelity Brownout Model for Real-Time Flight Simulations and Trainers," *Proceedings of the 65th Annual Forum of the American Helicopter Society*, Grapevine, TX, May 27–29, 2009.

[36] Wong, O. D., and Tanner, P. E., "Photogrammetric Measurements of an EH-60L Brownout Cloud," *66th Annual Forum of the American Helicopter Society*, Phoenix, AZ, May 10–13, 2010.

[37] Bagnold, R., *The Physics of Sediment Transport by Wind and Water: A Collection of Hallmark Papers*, American Society of Civil Engineers, 1988.

[38] Greeley, R., and Iversen, J. D., *Wind as a Geological Process on Earth, Mars, Venus and Titan*, Cambridge University Press, New York, NY, 1985.

[39] Shao, Y. and Lu, H., "A Simple Expression for Wind Erosion Threshold Friction Velocity," *Journal of Geophysical Research*, Vol. 105, No. D17, 2000, pp. 22.

[40] Cao, Z., Pender, G., and Meng, J., "Explicit Formulation of the Shields Diagram for Incipient Motion of Sediment," *Journal of Hydraulic Engineering*, Vol. 132, No. 10, 2006, pp. 1097–1099.

[41] Buffington, J., "The Legend of A.F. Shields," *Journal of Hydraulic Engineering*, Vol. 125, No. 4, 1999, pp. 376–387.

[42] Shields, A.F., "Application of Similarity Principles and Turbulence Research to Bed-Load Movement. Mitt Preuss, Verchsanst, Berlin. Wasserbau Schittbau," *Ott. WP, and Uchelen, JC,(translators): Pasadena, California Institute of Technology, WM Kech Laboratory of Hydraulics and Water Resources*, Vol. 167, 1936.

[43] Thomas, S., Kalra, T.S., and Baeder, J., "A Hybrid CFD Methodology to Model the Two-phase Flowfield beneath a Hovering Laboratory Scale Rotor," *30th American Institute for Aeronautics and Astronautics Applied Aerodynamics Conference*, New Orleans, LA, June 25–28, 2012.

[44] Syal, M., Govindarajan, B., and Leishman, J. G., "Mesoscale Sediment Tracking Methodology to Analyze Brownout Cloud Developments," *66th Annual Forum of the American Helicopter Society*, Phoenix, AZ, May 10–13, 2010.

[45] Syal, M., and Leishman, J. G., "Comparisons of Predicted Brownout Dust Clouds with Photogrammetry Measurements," *Proceedings of the 67th Annual Forum of the American Helicopter Society*, Virginia Beach, VA, May 3–5, 2011.

[46] Phillips, C., Kim, H. W., and Brown, R.E., "The Flow Physics of Helicopter Brownout," *66th Annual Forum of the American Helicopter Society*, Phoenix, AZ, May 10–13, 2010.

[47] Milluzzo, J., and Leishman, J. G., "Assessment of Rotorcraft Brownout Severity in Terms of Rotor Design Parameters," *Journal of the American Helicopter Society*, Vol. 55, No. 3, DOI: 10.4050/JAHS.55.032000, October 2010.

[48] Tritschler, J., Syal, M., Celi, R., and Leishman, J. G., "A Methodology for Rotor Design Optimization for Rotorcraft Brownout Mitigation," *Proceedings of the 66th Annual Forum of the American Helicopter Society*, Phoenix, AZ, May 10–13, 2010.

[49] Montes, J. and Ippen, A., *Interaction of Two-Dimensional Turbulent Flow with Suspended Particles*, Department of Civil Engineering, School of Engineering, Massachusetts Institute of Technology, 1973.

[50] Lavelle, J. and Mofjeld, H., "Bibliography on Sediment Threshold Velocity," *Journal of Hydraulic Engineering*, Vol. 113, No. 3, 1987, pp. 389–393.

[51] Adrian, R. and Westerweel, J., *Particle Image Velocimetry*, Vol. 30, Cambridge University Press, New York, NY, 2010.

[52] Raffel, M., Willert, C., and Kompenhans, J., *Particle Image Velocimetry: A Practical Guide*, Springer-Verlag, Berlin, Germany, 1998.

[53] Willert, C.E., and Gharib, M., "Digital Particle Image Velocimetry," *Experiments in Fluids*, Vol. 10, No. 4, 1991, pp. 181–193.

[54] Scarano, F., "Iterative Image Deformation Methods in PIV," *Measurement Science and Technology*, Vol. 13, No. 1, 2001, pp. R1–R19.

[55] Keane, R. and Adrian, R., "Theory of Cross-Correlation Analysis of PIV Images," *Applied Scientific Research*, Vol. 49, No. 3, 1992, pp. 191–215.

[56] Westerweel, J., "Fundamentals of Digital Particle Image Velocimetry," *Measurement Science and Technology*, Vol. 8, No. 12, 1999, pp. 1379–1392.

[57] Adrian, R., "Particle-Imaging Techniques for Experimental Fluid Mechanics," *Annual Review of Fluid Mechanics*, Vol. 23, No. 1, 1991, pp. 261–304.

[58] Keane, R. and Adrian, R., "Optimization of Particle Image Velocimeters," *Measurement Science and Technology*, Vol. 1, November 1991, pp. 1202–1215.

[59] Huang, H., Dabiri, D., and Gharib, M., "On Errors of Digital Particle Image Velocimetry," *Measurement Science and Technology*, Vol. 8, No. 12, 1999, pp. 1427–1440.

[60] Tropea, C., Yarin, A., and Foss, J., *Springer Handbook of Experimental Fluid Mechanics*, Vol. 1, Springer-Verlag, Berlin, Germany, 2007.

[61] Hunt, J.C.R., Wray, A.A., and Moin, P., "Eddies, Stream, and Convergence Zones in Turbulent Flows," *Center for Turbulence Research Report CTR-S88*, 1988, pp. 193–208.

[62] Graftieaux, L., Michard, M., and Grosjean, N., "Combining PIV, POD and Vortex Identification Algorithms for the Study of Unsteady Turbulent Swirling Flows," *Measurement Science and Technology*, Vol. 12, No. 9, 2001, pp. 1422.

[63] Leese, G.W., and Knight, J.T., Jr., "Helicopter Downwash Data," U.S. Army Engineer Waterways Experiment Station, Soils and Pavement Laboratory, Vicksburg, MS, June 1974.

[64] Lamb, H., *Hydrodynamics*, Cambridge University Press, Cambridge, UK, 1932.

[65] Kiger, K.T., and Pan, C., "PIV Technique for the Simultaneous Measurement of Dilute Two-Phase Flows," *Journal of Fluids Engineering*, Vol. 122, No. 4, 2000, pp. 811–818.

[66] Iversen, J.D., Greeley, R., Marshall, J.R., and Pollack, J.B., "Aeolian Saltation Threshold: The Effect of Density Ratio," *Sedimentology*, Vol. 34, No. 4, 2006, pp. 699–706.

[67] Ferguson, R. and Church, M., "A Simple Universal Equation for Grain Settling Velocity," *Journal of Sedimentary Research*, Vol. 74, No. 6, 2004, pp. 933–937.

[68] Aguirre-Pe, J., Olivero. M.L., and Moncada, A.T., "Particle Densimetric Froude Number for Estimating Sediment Transport," *Journal of Hydraulic Engineering*, Vol. 129, No. 6, 2003, pp. 428–437.

[69] Batchelor, G., *An Introduction to Fluid Dynamics*, Cambridge University Press, New York, NY, 3rd ed., 2000.

[70] Kramer, H., "Sand Mixtures and Sand Movement in Fluvial Models," *Transactions, American Society of Civil Engineers*, Vol. 100, 1935, pp. 798–878.

[71] Guoren, D., "Incipient Motion of Coarse and Fine Sediment," *Journal of Sediment Research*, Vol. 6, 1999, pp. 1–9.

[72] Miller, M., McCave, I., and Komar, P., "Threshold of Sediment Motion Under Unidirectional Currents," *Sedimentology*, Vol. 24, No. 4, 2006, pp. 507–527.

[73] Chien, N. and Wan, Z., *Mechanics of Sediment Transport*, American Society of Civil Engineers, Reston, VA, 1999.